In situ Transmission Electron Microscopy Studies of Microstructure Evolution in $Ba(Zr_{0.2}Ti_{0.8})O_3$-$x(Ba_{0.7}Ca_{0.3})TiO_3$ Piezoceramic

Dissertation

Vom Fachbereich 11, Material- und Geowissenschaften
der Technischen Universität Darmstadt
zur Erlangung des akademischen Grades
Doktor der Naturwissenschaften (Dr. rer. nat.)
genehmigte Dissertation von
M.Sc. Marina Zakhozheva
geboren am. 2. November 1986 in Novosibirsk, Russia

TECHNISCHE
UNIVERSITÄT
DARMSTADT

Referent: Prof. Dr. Hans-Joachim Kleebe
Korreferent: Prof. Dr. Jürgen Rödel

Tag der Einreichung: 12.07.2016
Tag der mündlichen Prüfung: 21.10.2016

Darmstadt 2016
D17

Statement of Authorship

I hereby certify that this thesis has been composed by myself and describes my own work unless otherwise acknowledged in the text. All references and verbatim extracts have been quoted and all sources of information have been specifically acknowledged. This thesis has not been accepted in any previous application for a degree.

Hiermit versichere ich, dass ich die vorliegende Arbeit selbstständig und ohne Benutzung anderer als der angegebenen Hilfsmittel angefertigt habe. Stellen, die wörtlich oder sinngemäß aus anderen Schriften entnommen sind, sind als solche kenntlich gemacht. Die Arbeit ist in gleicher oder ähnlicher Form noch nicht als Prüfungsarbeit eingereicht worden.

Darmstadt,

(M. Sc. Marina Zakhozheva)

Памяти моего деда - Евгения Владимировича Бадатова (1940 – 2008)

Acknowledgment

First of all, I was always thinking that studying abroad is a chance for a better future. And I was right. Therefore, I want to thank my advisor, Prof. Hans-Joachim Kleebe, for inviting me to his group in the Technische Universität Darmstadt in order to work on this exciting topic and to complete my PhD thesis here, in Germany. I am very grateful for his support, patience and motivation.

I am thankful for having a supervisor as enthusiastic as Dr. Ljuba Schmitt. I appreciate all her contributions of ideas and time, which made my thesis work possible. Even when she was very busy, she could find time for me. For me she is a good example of a successful scientist and I am very proud of the results we achieved. I have enjoyed the possibility to learn from her knowledge and experience.

I would like to thank my committee members, Prof. Hans-Joachim Kleebe, Prof. Jürgen Rödel, Prof. Wolfgang Ensinger and Prof. Michael J. Hoffmann, for their time, interest and helpful comments.

The major part of my experimental work was conducted at the Ames Laboratory, USA, for which I am grateful to Drs. Matthew Kramer and Lin Zhou for their assistance. A special thanks to Prof. Xiaoli Tan for his support and supervision during my time in USA. I am very thankful to Dr. Hanzheng Guo as I really benefited from his experience on *in situ* electric field TEM technique. I also would like to thank my former colleagues from the Iowa State University, Tim Prost and Tugce Karakulak, for help and advices.

All members of our group who contributed to my work. Therefore, I thank Dr. Stefan Lauterbach, Dr. Leopoldo Molina-Luna, Dr. Ingo Sethmann, Stefania Hapis, Mathis M. Müller, Carolin Wittich, Alexander Zintler and Kerstin Stricker. I am thankful to Angelika Willführ and Astrid Zilz for her help with administrative questions. Special thanks go to Ulrike Kunz for her great help with SEM measurements.

I appreciate help from Dr. Matias Acosta, Dr. Wook Jo and Dr. Roland Schierholz. Thank you very much for fruitful discussions, new ideas and your help whenever I needed.

I gratefully acknowledge the funding sources: AdRIA Hesse State Center for Adaptronics and the Deutsche Forschungsgemeinschaft that made my Ph.D. work possible.

I would also like to thank all my current colleagues from DENSsolutions as well as all HREM group from TU Delft. For the time being here I always feel support from all of you. It is a great to be in this team and I really enjoy this job.

I am very grateful for all my friends, especially Maria, Peter, Marina, Olesya and Chiara for their help and support whenever I needed it. Thanks to Lars Riekehr for being a part of my life. You made me much better person then I have been before. Without your help, I never would have finished my thesis and most likely would not stay in Europe. I would like to thank two people who entered my life recently but became a major part of it. Pauline and Jeroen, you are always with me in the most difficult moments. You help me to get my feelings under control and to believe in myself. You showed me the world from a different side, you teach and guide me like no one did before. I am grateful for your honest opinion even if it hurts sometimes because I feel that you always "stand behind me whatever I do and whatever decision I make".

Finally, I thank my family for all their love and encouragement and I will do it in Russian.

Мне всегда казалось, что учеба за границей это билет в счастливое будущее. Поэтому, когда мне предоставился такой шанс, я особо не раздумывала. Вместе с тем, уехать так далеко от семьи было не простым решением. Ведь я начала совершенно новую жизнь, где я сама отвечаю за себя и свои поступки. Несмотря на то, что вы находитесь в тысячи километрах, я всегда чувствую вашу поддержку. Вы всегда здесь со мной и я очень благодарна всем вам. Спасибо маме, бабуле, Оле, дяде Коле, Андрею, Кириллу, Артему и бабуле Зое. Без вас я бы никогда не добилась таких результатов и у меня не хватит слов, чтобы выразить всю признательность и любовь. Я очень благодарна бабе Тане за ее мудрость и советы. Я сожалею, что ты не дожила до этого момента и не можешь порадоваться моим успехам. Спасибо Ире, Вике, тете Люсе и всем моим родственникам, чьи имена я не назвала, но о которых всегда помню. Я благодорю моих друзей из Росии - Марину, Олесю, Таню, Раису и Алину. Спасибо, что были со мной.

И последние, я хочу поблагодарить моего деда - Бадатова Евгения Владимирович. Ты был и останешься главным учителем в моей жизни и примером во всем. Благодаря тебе я не опускаю руки и иду вперед. К сожалению, ты не дожил до этого дня и не можешь разделить моей радости. Но самое главное - я знаю, что оправдала все твои ожидания и, что ты бы очень гордился мной если бы был с нами. Я очень люблю тебя и хочу посвятить эту работу тебе и твоей памяти.

Table of Contents

List of Figures

List of Tables

List of Symbols

D	electrical displacement
d_{33}	piezoelectric coefficient
E	electric field
E_c	coercive field
E_{single}	electric field of a single-domain state appearance
k_{33}	coupling factor
P	polarization
P_{rem}	remanent polarization
P_s	saturation polarization
Q	electrostriction coefficient
r_A, r_B, r_O	ionic radii of A and B cation and O anion
S	strain
S_{neg}	negative strain
S_{rem}	remanent strain
S_{max}	maximum strain
s	stress
t	Goldschmidt tolerance factor
t_{obs}	observed tolerance factor
T	temperature
T_c	Curie temperature
T_d	depolarization temperature
$\tan\delta$	dissipation factor
γ	pyroelectric coefficient
χ	electrical susceptibility
ε	permittivity
ε_0	permittivity of vacuum
ε_r	relative permittivity

List of Abbreviations

BF	Bright field
BNT	$Bi_{1/2}Na_{1/2}TiO_3$
BNT – xBT	$(Bi_{1/2}Na_{1/2})TiO_3 – xBaTiO_3$
BNT – xBKT	$(Bi_{1/2}Na_{1/2})TiO_3 – xBi_{1/2}K_{1/2}TiO_3$
BNT – xBZT	$(Bi_{1/2}Na_{1/2})TiO_3 – Ba(Zr_xTi_{1-x})O_3$
BZT-xBCT	$Ba(Zr_{0.2}Ti_{0.8})O_3$-$x(Ba_{0.7}Ca_{0.3})TiO_3$
C	Cubic phase
CBED	Convergent beam electron diffraction
DP	Diffraction pattern
DW	Domain wall
EBDS	Electron backscatter diffraction
EDX	Energy-dispersive X-ray spectroscopy
iRAP	Innovative Research and Products, Inc.
MPB	Morphotrophic phase boundary
O	Orthorhombic phase
PNRs	Polar nanoregions
PPT	Polymorphic phase transition
PLZT	$(Pb_{0.92}La_{0.08})(Zr_{0.65}Ti_{0.35})O_3$
PZN – PT	$Pb(Zn_{1/3}Nb_{2/3})O_3 – PbTiO_3$
PZT	$Pb(Zr_xTi_{1-x})O_3$
R	Rhombohedral phase
RT	Room temperature
SAED	Selected area electron diffraction
SEM	Scanning electron microscopy
T	Tetragonal phase
TEM	Transmission electron microscopy
XRD	X-ray diffraction

1. Introduction

1.1 Motivation

Ferroelectrics play an important role in today's modern life. A large variety of applications including piezoelectric actuators, sensors, ultrasonic motors, dielectric capacitors, memory devices, energy harvesting devices, etc. are based on these materials [1-4]. A huge market for such devices grows continuously. Based on the report of Innovative Research and Products, Inc. (iRAP) from 2013, the global market of piezoelectric actuators and motors was estimated as $11.1 billion in 2013 and is expected to reach $16 billion in 2018, showing a high compound annual growth rate (CAGR) of 7.7% per year [5].

Today lead-based $Pb(Zr_xTi_{1-x})O_3$ (PZT) materials with perovskite structure are dominated on the market due to its superior electromechanical properties, ease of preparation and low cost [6]. Since PZT contains more than 60% of lead, which is toxic, environmental regulations in many countries initiated a search for potential lead-free substitutes for PZT. For example, the European Union directive regarding the use of certain hazardous materials restricts lead in electrical and electronic equipment [7]. Therefore, a search for alternative lead-free materials with competitive properties is of commercial and scientific importance for the last few decades. Over the years, numerous investigations were performed on lead-free systems containing $BaTiO_3$, $Bi_{0.5}Na_{0.5}TiO_3$, $Bi_{0.5}K_{0.5}TiO_3$, $BaZr_xTi_{1-x}O_3$, $Ba_{1-x}Ca_xTiO_3$, $(K_{0.5}Na_{0.5})NbO_3$, etc. [8-14]. High piezoelectric performance of the alkaline-niobate and alkaline-bismuth-titanate based solid solutions made it one of the most extensively studied piezoceramics [15-19]. However, since their electromechanical properties are still lower than those of PZT, up to now, environmentally friendly alternatives, which can replace lead-based materials in all devices, have not been found [9, 15-17].

In the recent past, scientific interest was given to the $Ba(Zr_{0.2}Ti_{0.8})O_3$-x$(Ba_{0.7}Ca_{0.3})TiO_3$ (abbreviated as BZT-xBCT) perovskite ferroelectric, designed by Liu and Ren, which exhibits superior electrical and mechanical properties [20-27]. Extremely high piezoelectric coefficient (d_{33} = 620 pC/N) was observed for the polymorphic phase transition (PPT) composition BZT-0.5BCT, which is even higher than for soft PZT [20]. Since the initial report of Liu and Ren, most studies on the BZT-xBCT piezoceramic were focused on the PPT composition, because of its outstanding properties [25, 28-30]. However, investigation of the BZT-BCT in a wide compositional range is necessary in order to fully understand the potential of this material for practical application. In this dissertation the structural features of a broad variety of BZT-xBCT were studied using a conventional transmission electron microscopy (TEM) technique. Finally, obtained results were compared and discussed with the electromechanical properties of this material.

Although enhanced piezoelectric performance makes BZT-xBCT a promising lead-free system, its commercial use is restricted by low Curie temperature, which depends on the composition but does not exceed 100 °C [20, 23, 31, 32]. It is also known, that the temperature rise of piezoelectric devices during utilization limits its practical application [33, 34]. Because of these two reasons, accurate studies on a temperature-dependent behavior of BZT-xBCT are required, in order to improve and optimize its application. In this work the microstructural changes and the evolution of ferroelectric domains during temperature-induced phase transition in BZT-xBCT system were monitored using *in situ* hot- and cold-stage TEM techniques.

Domain morphology plays a significant role in electromechanical properties of ferroelectrics [15, 35-38]. Since the external electric field induces a domain wall motion or domain switching, it is important to perform direct observations of domain structure evolution during electrical processes. In the present study *in situ* electric field TEM technique was used to visualize real-time microstructural changes over a wide compositional range of BZT-xBCT system in order to clarify microstructural mechanisms responsible for enhanced piezoelectric activity. Additionally, for specific compositions *in situ* electric field studies with simultaneous cooling were carried out. Such studies can provide important fundamental information about a phase transition behavior of BZT-xBCT system at low temperatures.

1.2 Dissertation Organization

The purpose of this work is to investigate microstructure features of the $Ba(Zr_{0.2}Ti_{0.8})O_3$-x$(Ba_{0.7}Ca_{0.3})TiO_3$ piezoelectric ceramic and to understand its influence on the enhanced piezoelectric response of this material. Transmission electron microscopy as a main experimental technique was used in order to achieve a goal of our study.

Chapter 2 provides a brief introduction to the fundamental aspects of dielectric, piezoelectric and ferroelectric materials and their structure. An overview of the most widely studied lead-based as well as lead-free systems is given. A detailed literature review on the electromechanical properties of the $Ba(Zr_{0.2}Ti_{0.8})O_3$-x$(Ba_{0.7}Ca_{0.3})TiO_3$ system and its microstructure features are discussed at the last part of this chapter.

Chapter 3 describes experimental details of the studies performed. Ceramic fabrication, sample preparation procedures, electrical properties measurements and structural characterization techniques such as scanning electron microscopy and transmission electron microscopy are discussed. Setup and performance of several *in situ* TEM techniques including *in situ* heating and cooling, *in situ* electric field and *in situ* electric field with simultaneous cooling are briefly described. A special attention was given to the *in situ* electric field TEM technique, which is a key technique of our studies.

Chapter 4 focuses on the results of conducted experiments. The electrical properties of the $Ba(Zr_{0.2}Ti_{0.8})O_3$-x$(Ba_{0.7}Ca_{0.3})TiO_3$ system are presented in a wide composition range. Moreover, the domain morphology evolution as a function of composition, temperature and electric field is monitored by conventional and *in situ* TEM.

Chapter 5 summarizes the main results and gives a detailed discussion of our findings with literature. Electrical properties of the $Ba(Zr_{0.2}Ti_{0.8})O_3$-x$(Ba_{0.7}Ca_{0.3})TiO_3$ are contrasted with the *in situ* electric field TEM results. Finally, perspectives for further investigations are given.

2. Literature review

2.1 Fundamental Characteristics of Dielectric, Piezoelectric and Ferroelectric materials

The following description of basic properties of ferroelectric materials was done based on books of Jaffe et al. [6], Moulson et al. [39] and Waser et al. [40].

Dielectrics are insulator materials, which can be polarized by applying an external electric field. When the dielectric material is placed in the electric field, separation of the centers of positive and negative charges occurs, leading to the formation of dipoles. The polarization (P) can be defined as a dipole moment per unit volume and can be related to the electric field (E) through electrical susceptibility χ:

$$P = \varepsilon_0 \chi E \qquad 1$$

where ε_0 is the permittivity of free space and is equal to $8.85 \cdot 10^{-12}$ F/m. An electrical displacement D can be defined as:

$$D = \varepsilon_0 E + P = \varepsilon_0 (1 + \chi) \mathrm{E} = \varepsilon_0 \varepsilon_r E \qquad 2$$

where ε_r is the dielectric constant or relative permittivity. All dielectrics exhibit a property of electrostriction, which causes an elastic deformation of material under the application of an electric field. The resulting strain S is proportional to the polarization squared by the electrostriction coefficient, which is forth rank tensor Q_{ijkl}:

$$S_{ij} = Q_{ijkl} P_k P_l \qquad 3$$

Certain classes of dielectrics exhibit a property, which is called a piezoelectric effect. Piezoelectric materials, which are a subgroup of dielectrics (Figure 2.1), produce an electric charge when a mechanical stress is applied to it (direct piezoelectric effect) or exhibit a strain in response to an applied electric field (inverse piezoelectric effect). Such effect can be observed only in non-centrosymmetric crystalline materials. From 32 crystal classes 21 are non-centrosymmetric and 20 exhibit a piezoelectric behavior. Mathematically, direct (equation 4) and inverse (equation 5) piezoelectric effect can be described in terms of tensor form:

$$P_i = d_{ijk} s_{jk} \qquad 4$$

$$S_{ij} = d_{ijk} E_k \qquad 5$$

where P_i is the polarization vector, s_{jk} is the mechanical stress tensor, S_{ij} is the mechanical strain tensor, E_k is the electric field vector, and d_{ijk} is the piezoelectric coefficient tensor.

Pyroelectrics refer to materials with a unique polar axis, which can exhibit a spontaneous polarization in a limited temperature range. In other words, pyroelectrics can generate a voltage as a response to temperature changes. Spontaneous polarization P_s is proportional to the change of temperature ΔT:

$$P_{si} = \gamma_i T \qquad 6$$

where γ_i is the pyroelectric coefficient. Above the Curie temperature (T_c) specific properties of pyroelectric materials disappear as a result of the phase transition to the paraelectric state, where the crystal structure becomes symmetric. From 20 piezoelectric crystal classes 10 are pyroelectrics.

Ferroelectrics, which are a subgroup of pyroelectrics (Figure 2.1), are characterized by the existence of a spontaneous polarization, which can be reoriented by an applied electric field. Figure 2.1 schematically illustrates the classification of dielectrics. Ferroelectric materials consist of regions with different net polarization, which are called ferroelectric domains. The domain morphology has a significant influence on the ferroelectric behavior, leading to a different type of ferroelectric material. Large micrometer-sized ferroelectric domains are typical for the normal ferroelectrics, while relaxor ferroelectrics are characterized by polar nanoregions (PNRs). During heating both types of ferroelectrics undergo a phase transition to the cubic paraelectric state. However, in contrast to the normal ferroelectric, which display a sharp transition to the paraelectric phase at T_c, relaxor ferroelectrics exhibit a diffuse transition with a wide peak in dielectric constant [35].

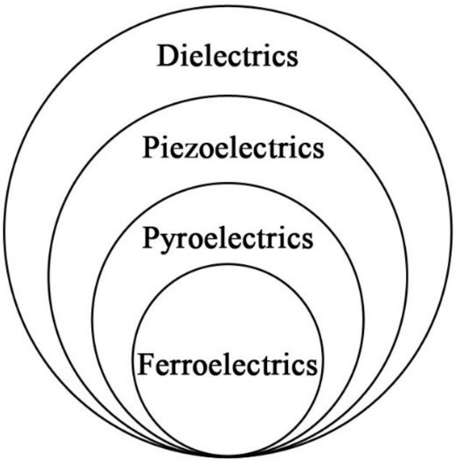

Figure 2.1: Classification of dielectrics.

One of the most important features of ferroelectric materials is the hysteresis character of the polarization - electric field (P - E) loop (Figure 2.2 (a)). In ferroelectric materials at the initial state all dipoles within domains are randomly orientated (I). When an external electric field is applied, dipoles tend to align themselves according to the field direction (II) until maximum alignment is achieved (saturation polarization P_s) (III). When the field is reduced to zero, a certain amount of dipoles do not switch back to their original configuration, leading to the remanent polarization P_{rem} (IV). In order to reduce the polarization, an electric field with reversed polarity must be applied. The polarization reaches zero value when the applied electric field is equal to the coercive field E_c (V). Further increase in the external field with revised polarity leads to the opposite alignment of dipoles (VI). After a full cycle P - E curve form a closed hysteresis loop (Figure 2.2 (a)).

The evolution of strain S under an external electric field is shown in Figure 2.2 (b). All characteristic parameters as maximum strain S_{max}, remanent strain S_{rem}, negative strain S_{neg}, and coercive field E_c are depicted on the S - E curve. A typical feature of the S – E hysteresis loop is its "butterfly" shape. Areas on the S - E loop, marked as (I) to (VI) are in agreement with Figure 2.2 (a).

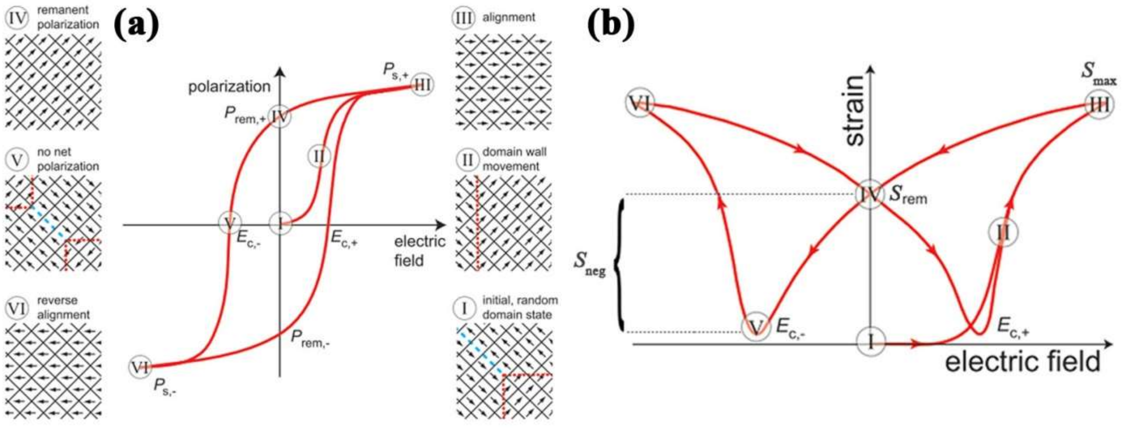

Figure 2.2: (a) Ferroelectric P – E hysteresis loop with characteristic parameters and scheme of domain evolution. (b) Bipolar S – E hysteresis loop with characteristic parameters [41].

2.2 Ferroelectric domains

Piezoelectric ceramics are characterized by a well-defined domain structure, which is critical to dielectric, piezoelectric and ferroelectric properties of these materials [42, 43]. As was mentioned above, ferroelectric domains are the regions of the crystal, which exhibit a uniform polarization. Orientation of spontaneous polarization within ferroelectric domains is governed by crystal structure of material and, therefore, is limited to certain crystallographic directions. For tetragonal crystal structure, such as $BaTiO_3$, polarization is orientated along one of six <100> directions and, therefore, the angle between two domains can be either 90° or 180° (Figure 2.3). As an example, Figure 2.3 illustrates an arrangement of ferroelectric domains inside the grain for tetragonal $BaTiO_3$. In comparison, polarization direction of domains in the rhombohedral ferroelectrics is aligned along one of eight <111> crystallographic directions, which leads to 71°, 109° or 180° angles between two domains. Two domains are separated by the interface, which is known as domain wall (DW). Thus, for tetragonal crystal structure only {110}c type of domain walls are permissible for 90° configuration, while 180°

configuration does not require any specific plane of domain wall. In case of rhombohedral structure, the nomenclature is different in different literature sources [44]. According to the angle between the polar axis, the {100} domain walls are defined as 71° and the {110} domain walls as 109° [45]. Regarding the angle between the polarization vectors in a head-to-tail arrangement, the nomenclature of the permissible domain walls is vice versa ({100} orientation for 109° and {110} for 71°) [46]. For 180° domains any plane parallel to the polarization direction is permissible [44-46]. In this dissertation we will adopt the first nomenclature.

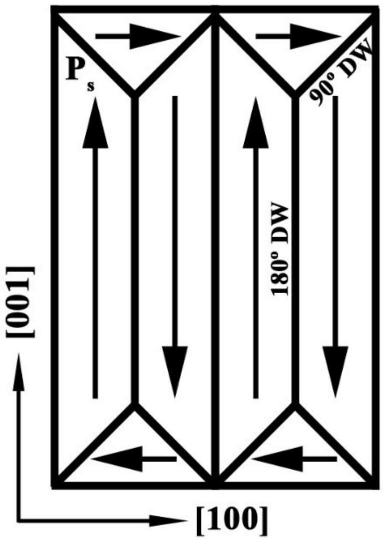

Figure 2.3: Schematic illustration of ferroelectric domains and domain walls within one grain in tetragonal BaTiO3. Dark arrows within individual domains represent a polarization direction (Ps). Crystallographic directions are given for cubic system.

2.3 Perovskite structure

The natural mineral perovskite ($CaTiO_3$) was discovered in 1839 in the Ural Mountains by Gustav Rose and named after Russian mineralogist Lev Aleksevich von Perovski [47]. The chemical formula of perovskites is ABX_3, where A-site cation is a divalent alkali earth or trivalent rare earth metal and B-site cation is a transition metal with partly filled d-orbitals [48]. The anion X is usually oxygen, however, perovskite structures containing fluorine, chlorine or sulfur are also known and of technological interest. In this chapter only oxide perovskites ABO_3 will be discussed. The ideal perovskite structure has a cubic symmetry with Pm-3m space group, where larger A-site cations are located at the corners of the cube and surrounded by 12 anions, whereas smaller B-site cations, which are octahedrally coordinated by 6 anions, occupy the body centered position (Figure 2.4 (a)). In this case BO_6 octahedra (oxygen octahedra) are in the center of the unit cell. Alternatively, an ideal perovskite structure can be viewed as a network of corner-sharing BO_6 octahedra surrounded by A-site cations (Figure 2.4 (b)).

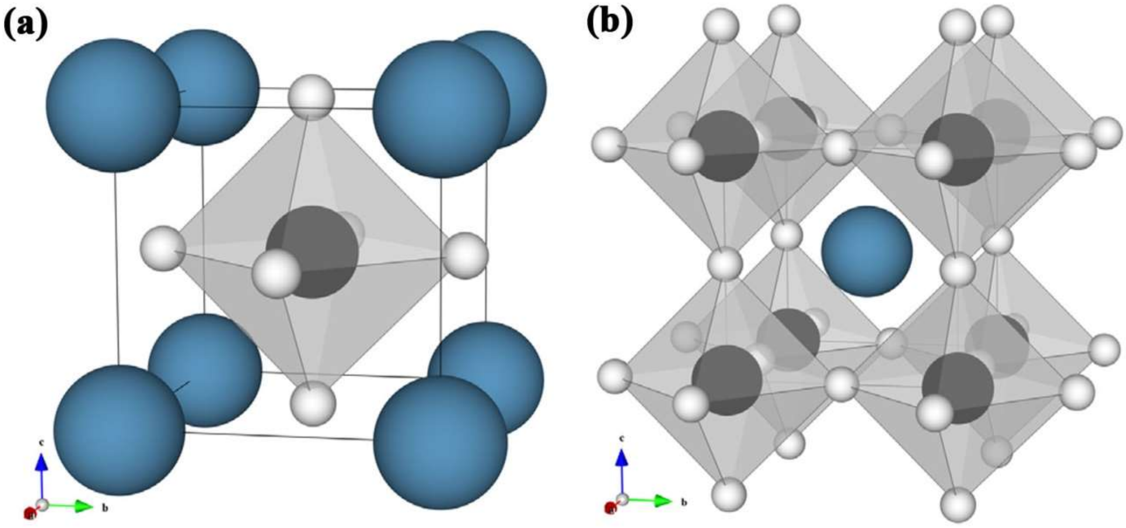

Figure 2.4: Ideal perovskite structure with a chemical formula ABO_3. A-site cations are blue, B-site cations are black, anions are white. (a) BO_6 octahedra are in the center of the unit cell. (b) BO_6 octahedra are in the corners [49].

However, most perovskites do not have the ideal cubic structure due to distortions, which reduce the crystal symmetry. Three types of distortions produced by tilting of the oxygen octahedra, displacements of the cations within the octahedra or distortions of the oxygen octahedra were identified by Glazer [50, 51]. The Goldschmidt tolerance factor (t) concept can be used to predict the stability of the perovskite crystal structure [52]:

$$t = \frac{r_A + r_O}{\sqrt{2}(r_B + r_O)} \qquad 7$$

where r_A, r_B and r_O are the ionic radii of A and B cation and O anion, respectively. The list of the effective ionic radii for oxide and fluoride structures were established by Shannon [53]. Sasaki et al. defined the observed tolerance factor in order to describe a structure deformation from the octahedra tilts and/or distortions in a systematic way [54]:

$$t_{obs} = \frac{<A-O>}{\sqrt{2}<B-O>} \qquad 8$$

where <A–O> and <B–O> are average cation – anion distances. The undistorted cubic structure is stable only for ideal A–O and B–O bond lengths and requires t = 1 (Figure 2.5 (a)) [15]. If the tolerance factor is less than one, the A-site ions are smaller than the ideal cubic structure allows. Therefore, a deviation of the crystal lattice, driven by rotation of the BO_6 octahedra, occurs (Figure 2.5 (b)) [55, 56]. In perovskites with the tolerance factor greater than one, the B-site ions are small. This leads to the displacements of the cations within the BO_6 octahedra and polar (or ferroelectric) distortions (Figure 2.5 (c)) [55, 56].

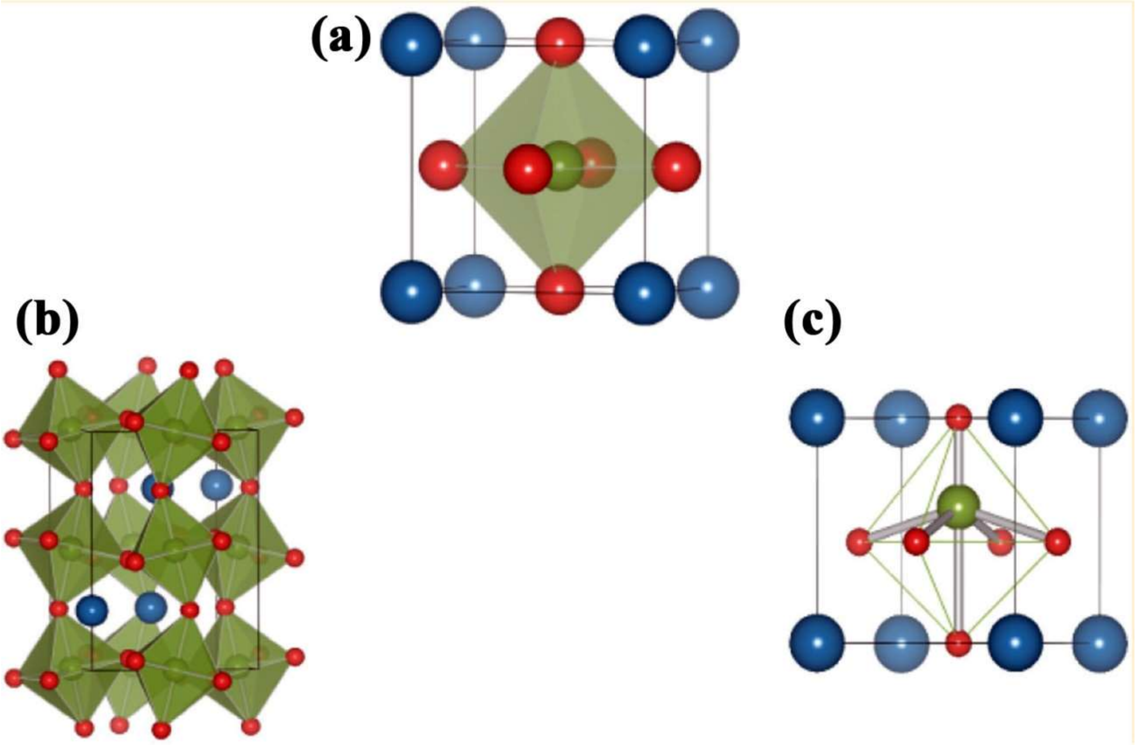

Figure 2.5: (a) Ideal cubic perovskite structure. (b) Distortions produced by tilting of the oxygen octahedra. (c) Distortions produced by displacements of the ions [57].

In 1972 Glazer developed a notation to classify octahedral rotations in perovskites, which is the most common used today [50]. He introduced 23 possible tilt systems, which describe the rotations of the oxygen octahedra around particular Cartesian axis by three letters with superscripts ($a^ib^jc^k$), indicating magnitudes and directions of the octahedra rotation around certain axis [50, 51]. For example, $a^+a^+c^-$ tilt system reveals the same rotation angle around x and y axes and different one for z axis. A positive superscript denotes in phase rotation, while a negative indicates out of phase rotation of adjacent octahedra (superscript 0 denotes no rotation). In order to clarify Glazer notation, Figure 2.6 displays a schematic illustration of two single tilt systems: $a^0a^0c^+$ and $a^0a^0c^-$, where in phase and out of phase octahedra rotation exist only around z-axis.

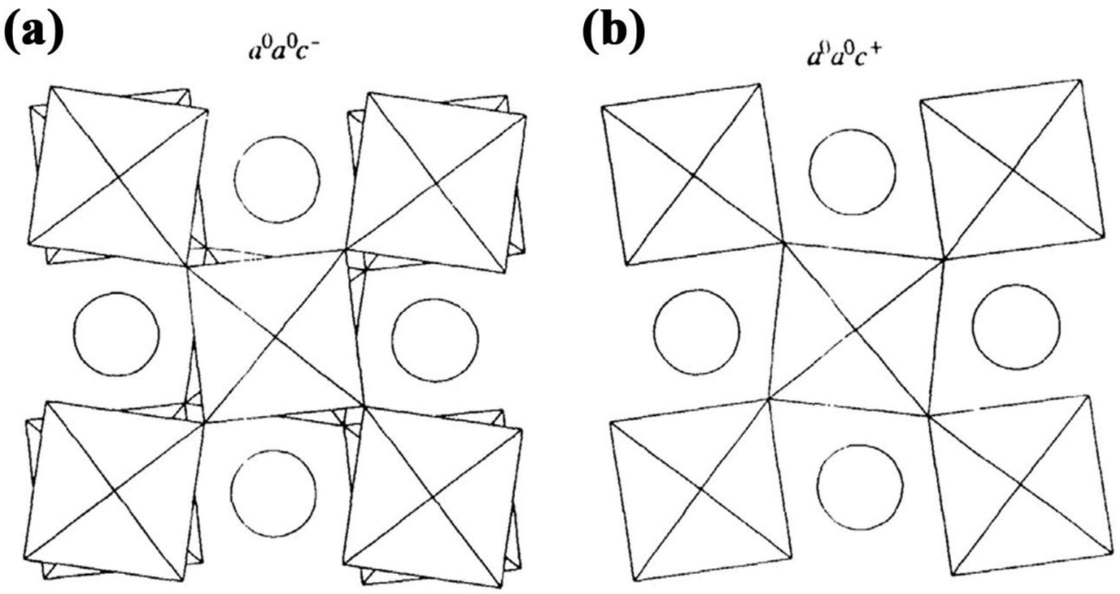

Figure 2.6: Comparison of two single tilt systems (a) $a^0a^0c^+$ and (b) $a^0a^0c^-$. Viewing direction is along z-axis [58].

2.4 Lead-containing piezoelectric ceramics

As mentioned above, lead-based piezoelectric ceramics, represented by $Pb(Zr_{1-x}Ti_x)O_3$ (PZT), exhibit very high electromechanical properties. After its discovery in 1952 [59], PZT has been widely studied and extensively used in industrial applications [6, 39, 60-63]. PZT is a solid solution of lead zirconate ($PbZrO_3$) and lead titanate ($PbTiO_3$) with a perovskite structure, where A-sites are occupied by Pb^{2+} ions, while Ti^{4+} or Zr^{4+} ions are randomly distributed on B-sites [6, 39]. Figure 2.7 (a) represents a composition-temperature phase diagram for the PZT solid solution initially proposed by Sawaguchi et al. [64] and then refined by Jaffe et al. [6]. For all PZT compositions at high temperature a paraelectric cubic (space group Pm3m) phase is stable (Figure 2.7 (a)). During cooling a phase transition from paraelectric to ferroelectric phase occurs at the Curie temperature, which varies from 230 °C for $PbZrO_3$ to 500 °C for $PbTiO_3$ depending on the composition. A significant feature of the PZT phase diagram is the existence of a nearly temperature independent phase transition between high temperature ferroelectric rhombohedral (space group *R*3*m*) phase and ferroelectric tetragonal (space group *P4mm*) phase at the composition $x = 0.48$ (Figure 2.7 (a)) [6, 39], where piezoelectric properties peak. For the composition with $x < 0.48$, except already mentioned ferroelectric rhombohedral phase, either antiferroelectric orthorhombic (space group *Pbam*) or low temperature ferroelectric rhombohedral (space group *R3c*) phases are stable (depending on temperature and composition), while ferroelectric tetragonal phase is stable everywhere for $x > 0.48$ (Figure 2.7 (a)) [6, 39]. However, later the appearance of a low-temperature monoclinic phase (space group *Cm*) at the morphotropic phase boundary (MPB) was demonstrated by means of high-resolution synchrotron X-ray powder diffraction [65]. More detailed investigations confirmed an existence of a monoclinic phase as a bridging phase in between rhombohedral and tetragonal phases [66, 67]. A revised phase diagram for PZT system is depicted on Figure 2.7 (b) [68].

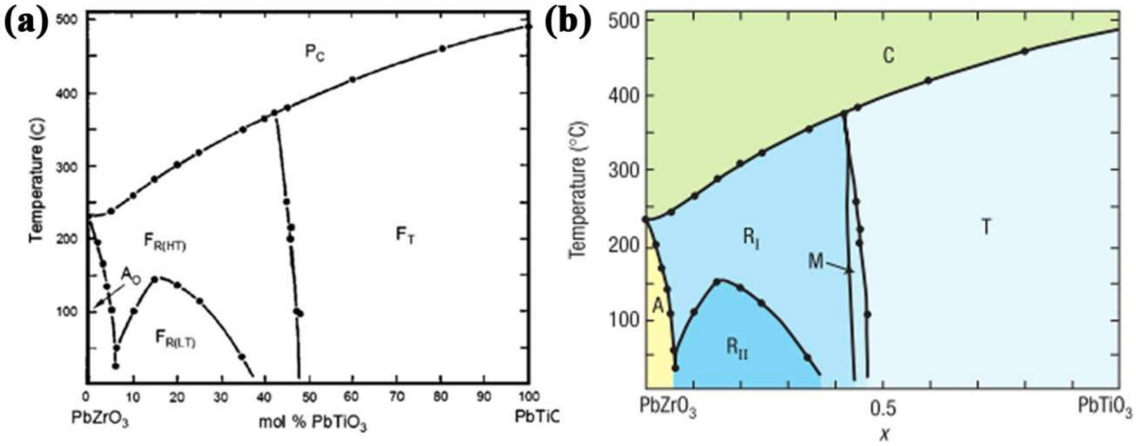

Figure 2.7: (a) Composition-temperature phase diagram for the PZT solid solution [6]. Pc: paraelectric cubic; FR(HT) and FR(LT): high- and low-temperature ferroelectric rhombohedral; FT: ferroelectric tetragonal; Ao: antiferroelectric orthorhombic. (b) Revised phase diagram for the PZT solid solution [68]. C: Paraelectric cubic; RI and RII: High- and low-temperature ferroelectric rhombohedral; T: Ferroelectric tetragonal; A: Antiferroelectric orthorhombic; M: Ferroelectric monoclinic.

The MPB composition attracts the most attention due to its very high piezoelectric coefficients, dielectric permittivity, remanent polarization and electromechanical coupling coefficients [6, 39]. The origin of the strong piezoelectric and dielectric properties for that composition have been studied extensively over the past few decades but it is still under discussion in the literature [69, 70]. It is commonly accepted that the enhancement of piezoelectric properties at the MPB region is related to the facilitated polarization rotation along rhombohedral and tetragonal phases during poling, due to flattening of the free energy profile [71-73]. At the MPB 6 equivalent <100> polarization directions from tetragonal phase coexist with 8 equivalent <111> polarization directions from rhombohedral phase. Therefore, 14 alternative polarization directions are available for the MPB composition, which increase the polarizability and result in enhanced piezoelectric properties of the material [74].

PZT ceramics are rarely used in the pure form. For certain application, the properties of PZT can be adjusted by donor or acceptor doping [6, 60]. The concentration of dopants is usually 0.05 – 5 at. % [39]. The addition of the donor-type dopants (higher valence) creates a cation-vacancy [39, 60] and causes the increases in dielectric constant, electromechanical coupling factor, and decrease in coercive field [39, 75, 76]. Materials, which exhibit such properties, are known as “soft” PZT [6]. The typical donor dopants are La^{+3} on the A-site and Nb^{+5}, Sb^{5+} on the B-site [74, 75]. Acceptor-type dopants (lower valence) generate oxygen vacancies [39, 60], which lead to reduction in dielectric constant, dielectric loss, and an increase in mechanical quality factor and coercive field. Such properties are typical for “hard” PZT [6]. Common acceptor dopants are Na^+, K^+ on the A-site and Fe^{3+}, Al^{3+}, Mn^{3+}, Mg^{2+}, on the B-site [74, 75].

2.5 $Bi_{1/2}Na_{1/2}TiO_3$-based ferroelectrics

$Bi_{1/2}Na_{1/2}TiO_3$ (BNT) is a relaxor ferroelectric with ABO_3 perovskite structure, where Bi^{3+} and Na^+ cations share the A-sites and Ti^{4+} cations occupy the B-sites. Discovered in 1961 by Smolenskii et al. [8], at room temperature BNT has a rhombohedral R3c structure with anti-phase $a^-a^-a^-$-type oxygen octahedral tilting [51], which is stable from -268 to 255 ºC [77]. On heating a phase transition to a tetragonal P4bm structure with in-phase $a^0a^0c^+$-type octahedral tilting occurs. Pure tetragonal phase is observed at the temperature range from 400 ºC to 500 ºC. Above 540 ºC a cubic structure with Pm-3m symmetry becomes stable [77]. Between 255 ºC and 400 ºC a rhombohedral – tetragonal phase coexistence is observed, while tetragonal and cubic phases coexist in the temperature range from 500 ºC to 540 ºC. Reported Curie temperature for that system is about 320 °C [6, 78, 79]. The tetragonal phase above the Curie temperature is considered to be ferroelastic [80, 81] or superparaelectric [82], which transforms to the paraelectric cubic phase at 540 ºC [79, 80].

High Curie temperature and relatively good electromechanical properties (piezoelectric constant of 73 pC/N and remanent polarization of 38 µC/cm^2 at room temperature) make BNT an appropriate substitute for PZT [8, 18, 77, 83-85]. However, low polarizability of BNT ferroelectric results in its high coercive field (E_c = 7.3 kV/mm) and therefore BNT is not suitable for many applications [86-89].

Various BNT-based systems were proposed in order to improve its properties [18, 90, 91]. Reported by Takenaka et al. [18] $(Bi_{1/2}Na_{1/2})TiO_3 – xBaTiO_3$ (BNT – xBT) is one of the most promising BNT-based solid solution due to its superior piezoelectric properties and ease of processing [92]. The phase diagram of BNT – xBT displays a MPB at 6~7 mol %BT, where rhombohedral and tetragonal phases coexist [18]. Similar to PZT, for the composition around the MPB region optimum piezoelectric and dielectric properties are observed (piezoelectric constant up to 180 pC/N, coupling factor (k_{33}) of 0.55, remanent polarization up to 38.8 µC/cm^2) [18, 83, 93-97]. However, low depolarization temperature (T_d) limits an application of the BNT – BT system as a lead-free substitute for PZT [98, 99]. An overview of properties of BNT – xBT solid solution are summarized in Table 2.1 [41].

Table 2.1: Properties of BNT – xBT, summarized by R. Dittmer [41].

Parameter	Takenaka et al. [18]	Chu et al. [93]	Xu et al. [94]	Chen et al. [95]	Xu et al. [83]	Zhang et al. [12]	unit
composition x	0.06	0.06	0.06	0.07	0.06	0.06	
coupling factor	k_{33}=0.55	k_p=0.29	k_p=0.28	k_p=0.26	k_p=0.367	k_p=0.29	
piezoelectric constant, d_{33}	125	122	180	176	155	110	pC·N^{-1}
depolarization temperature, T_d	150	100	n/a	87	129	124	°C
remanent polarization, P_{rem}	0.2	0.4	0.37	0.378	0.388	0.34	C·m^{-2}
coercive field, E_c	n/a	2.88	4.27	2.72	3.41	2.6	kV·mm^{-1}
structure	R/T	R/T	R/T	R/T	R/T	n/a	

Another binary system based on BNT with promising properties is $(Bi_{1/2}Na_{1/2})TiO_3$–$xBi_{1/2}K_{1/2}TiO_3$ (BNT – xBKT). This solid solution exhibits a MPB between rhombohedral and tetragonal structures in the range of x = 0.16 – 0.2, where the highest dielectric constant, piezoelectric constant and the coupling factor were obtained [76, 100, 101]. BNT – xBKT system exhibit a depolarization temperature of 174 °C, which is higher than that for BNT – BT. Table 2.2 lists the properties of BNT – 0.2BKT [41].

Table 2.2: Properties of BNT – 0.2BKT, after R. Dittmer [41].

Parameter	Sasaki et al. [100]	Yoshii et al. [102]	Hiruma et al. [103]	unit
relative permittivity $\varepsilon_{r,33}$	1030	884	930	
coupling factor	k_p=0.27	k_{33}=0.54	k_{33}=0.54	
piezoelectric constant	d_{31}=46.9	d_{33}=157	d_{33}=167	pC·N^{-1}
depolarization temperature, T_d	n/a	174	175	°C
remanent polarization, P_{rem}	0.199	0.384	n/a	C·m^{-2}
coercive field, E_c	3.0	3.6	n/a	kV·mm^{-1}

Piezoelectric properties of BNT can be also improved by adding $Ba(Zr_xTi_{1-x})O_3$ (BZT), which has a tetragonal symmetry [104]. In BNT – xBZT, Zr^{4+} ions replace Ti^{4+} on the B-sites of the ABO_3 perovskite structure. As well as in case of other high piezoelectric systems, enhanced properties of the BNT – BZT were obtained for the composition at the MPB, which separates ferroelectric rhombohedral (BNT side) and tetragonal (BZT side) crystal structures (Table 2.3). [13, 104-107].

Table 2.3 Properties of BNT – xBZT system around MPB.

parameter	Peng et al. [104]	Chen et al. [105]	Sawangwan et al. [107]	unit
composition x	0.09	0.06	0.07	
relative permittivity $\varepsilon_{r,33}$	881.4	950	1839	
coupling factor	n/a	k_p=0.27	n/a	
dissipation factor, tanδ	2.636	n/a	5.85	%
piezoelectric constant, d_{33}	147	168	161	$pC \cdot N^{-1}$
remanent polarization, P_{rem}	0.16	n/a		$C \cdot m^{-2}$

2.6 $Ba(Zr_{0.2}Ti_{0.8})O_3$ – $x(Ba_{0.7}Ca_{0.3})TiO_3$ piezoelectric ceramic

Lead-free $Ba(Zr_{0.2}Ti_{0.8})O_3$ – $x(Ba_{0.7}Ca_{0.3})TiO_3$, referred to as BZT – xBCT, solid solution received considerable attention in recent years due to its enhanced piezoelectric properties [21-26]. Since its discovery by Liu and Ren [20], the microstructural features [27, 108], phase transitions [109-111], elastic, dielectric, piezoelectric and ferroelectric properties [21, 112, 113] etc. have been widely studied. All BZT – xBCT compositions exhibit a perovskite structure, where Ba^{2+} ions on A-sites are substituted by Ca^{2+} ions, while Ti^{4+} ions on B-sites are substituted by Zr^{4+} ions.

Liu and Ren proposed the phase diagram of the BZT – xBCT system, which was obtained from the temperature dependent dielectric permittivity and X-Ray diffraction measurements (Figure 2.4) [20]. According to them, the phase diagram contains a paraelectric cubic (C) (space group Pm-3m), ferroelectric rhombohedral (R) (space group R3m) and ferroelectric tetragonal (T) (space group P4mm) phase. The paraelectric cubic phase becomes stable at the Curie temperature, which varies from 0 to 100 °C, depending on the composition. On cooling, for the BZT – xBCT with $x < 0.32$ a single phase transition from paraelectric cubic to ferroelectric rhombohedral phase occurs. An increase in the BCT content ($x > 0.32$) leads to the appearance of the ferroelectric tetragonal phase between rhombohedral and cubic ones. Therefore, on cooling two phase transitions, C ⟶ T and T ⟶ R, can be observed in this compositional range (Figure 2.8 (a)). Two ferroelectric phases are separated by the MPB, which is extremely temperature dependent and hence, more precisely named as a polymorphic phase transition (PPT). The PPT starts from the triple point, where the paraelectric C phase coexists with ferroelectric R and T phases, which locates at $x \sim 0.32$ and at $T \sim 57$ °C [20]. It should be noted that the C – R – T triple point, was also observed for high-piezoelectric lead-based systems such as PZT and $Pb(Zn_{1/3}Nb_{2/3})O_3 – PbTiO_3$ (PZN–PT) [114].

Numerous investigations support a phase diagram designed by Liu and Ren [21, 31]. However, a lot of studies showed an area around the PPT, where a coexistence of R and T phases was observed [27, 109, 112, 113]. Its presence has been shown by several experimental techniques such as Raman, thermally stimulated depolarization currents, and elastic and dielectric properties [113, 115, 116]. For example, using temperature dependent *in situ* X-Ray diffraction technique, Ehmke et al. reported an evidence of a phase coexistence region over a considerable temperature and composition range, which includes R, T and possibly C phases [112]. The phase diagram including the vicinity of the triple point, designed by Ehmke et al., is depicted in Figure 2.8 (b). More recent studies, performed by Keeble et al. by means of high-resolution synchrotron X-Ray powder diffraction, verified the existence of an intermediate orthorhombic (O) phase (space group *Amm2*) between the rhombohedral and tetragonal ones (Figure 2.8 (c)) [32]. Therefore, the previously reported sequence of phase transitions (from low to high temperature) R → T → C is identified as R → O → T → C, which is identical to that in the $BaTiO_3$ system [32]. Instead of a triple point [20], Keeble et al. observed a phase convergence region, where rhombohedral, tetragonal, orthorhombic, and cubic phases are hardly distinguishable experimentally [32]. Appearance of an O phase as a bridging phase at narrow region between R and T was also confirmed by Tian et al. [111] and Zhang et al. [117].

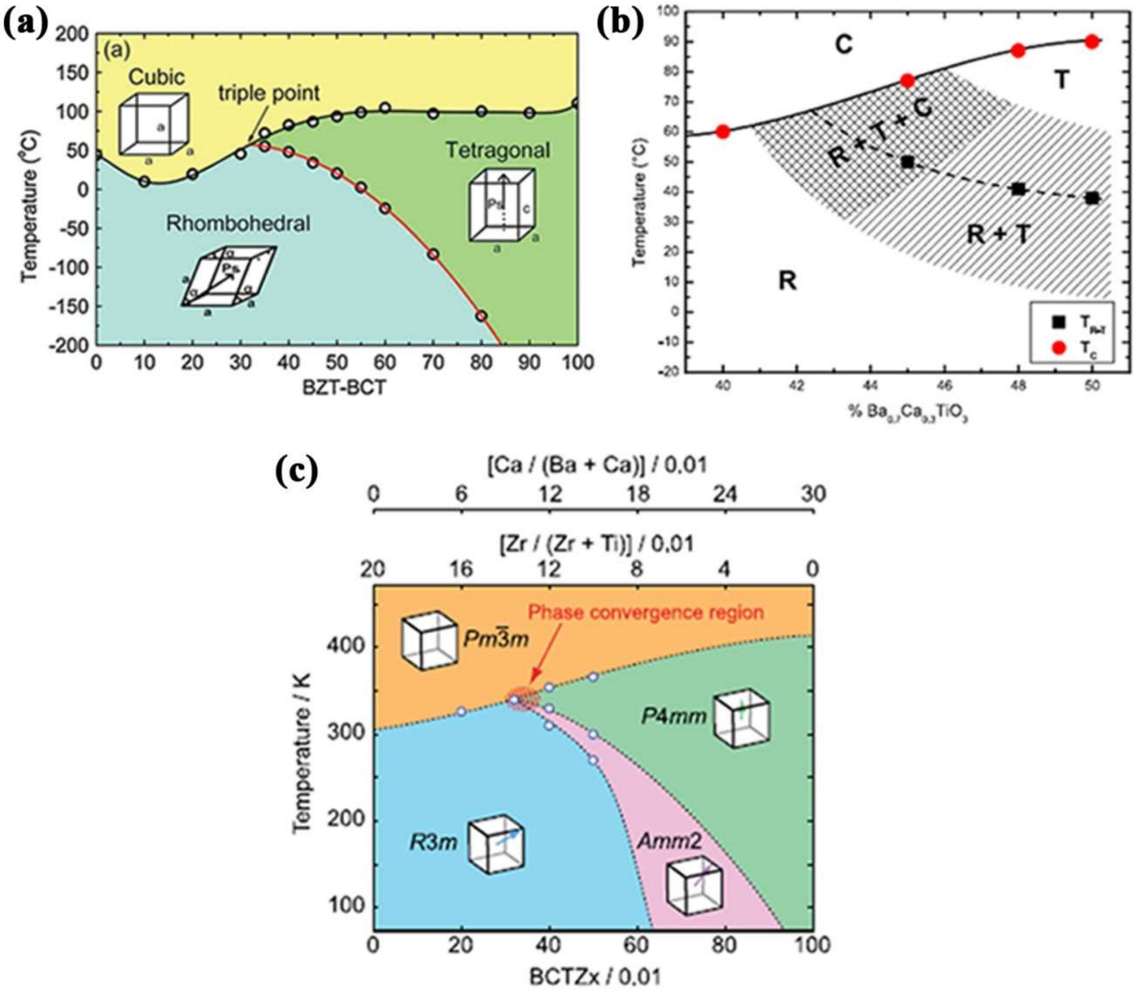

Figure 2.8: (a) Composition – temperature phase diagram of BZT-xBCT, designed by Liu and Ren [20]. (b) Phase diagram of BZT-xBCT close to the PPT, designed by Ehmke et al. [112]. (c) Revised phase diagram of BZT-xBCT, designed by Keeble et al. [32].

Properties of the BZT – xBCT piezoceramic are strongly dependent on the composition and temperature. For the PPT composition BZT – 0.5BCT, Liu and Ren observed enhanced electromechanical properties, such as very high saturation and remanent polarization (P_s = 19.8 µC/cm^2 and P_{rem} = 14.5 µC/cm^2), low coercive field (E_c = 0.168 kV/mm), high dielectric permittivity (ε ~ 3060) and high piezoelectric coefficient (d_{33} = 560-620 pm/V) (Figure 2.9 (a)) [20]. Enhanced piezoelectricity of the PPT composition was attributed to the tricritical nature of the triple point, which indicates a low energy barrier between C, R and T phases and therefore facilitates polarization rotation between T and R phases [20]. The reduced free energy anisotropy was recently calculated by a phenomenological approach and indeed a broad area of the phase diagram presents a low energy barrier for polarization rotation, specifically around phase boundaries [118]. By means of resonance method, Xue et al. investigated a full set of elastic, dielectric and piezoelectric properties of the BZT –

0.5BCT as a function of temperature [21]. The optimum properties were observed around room temperature, which coincides with a PPT area for that composition (Figure 2.9 (b)). Deviation from the PPT leads to the reduction of the dielectric, piezoelectric and electromechanical properties. Nevertheless, at low temperature BZT-0.5BCT exhibit appreciable piezoelectric constant (d_{33} = 93 pC/N at T = -50 °C). High piezoelectricity of the BZT-0.5BCT was attributed to the low polarization anisotropy and to the elastic softening of the lattice near the PPT [21].

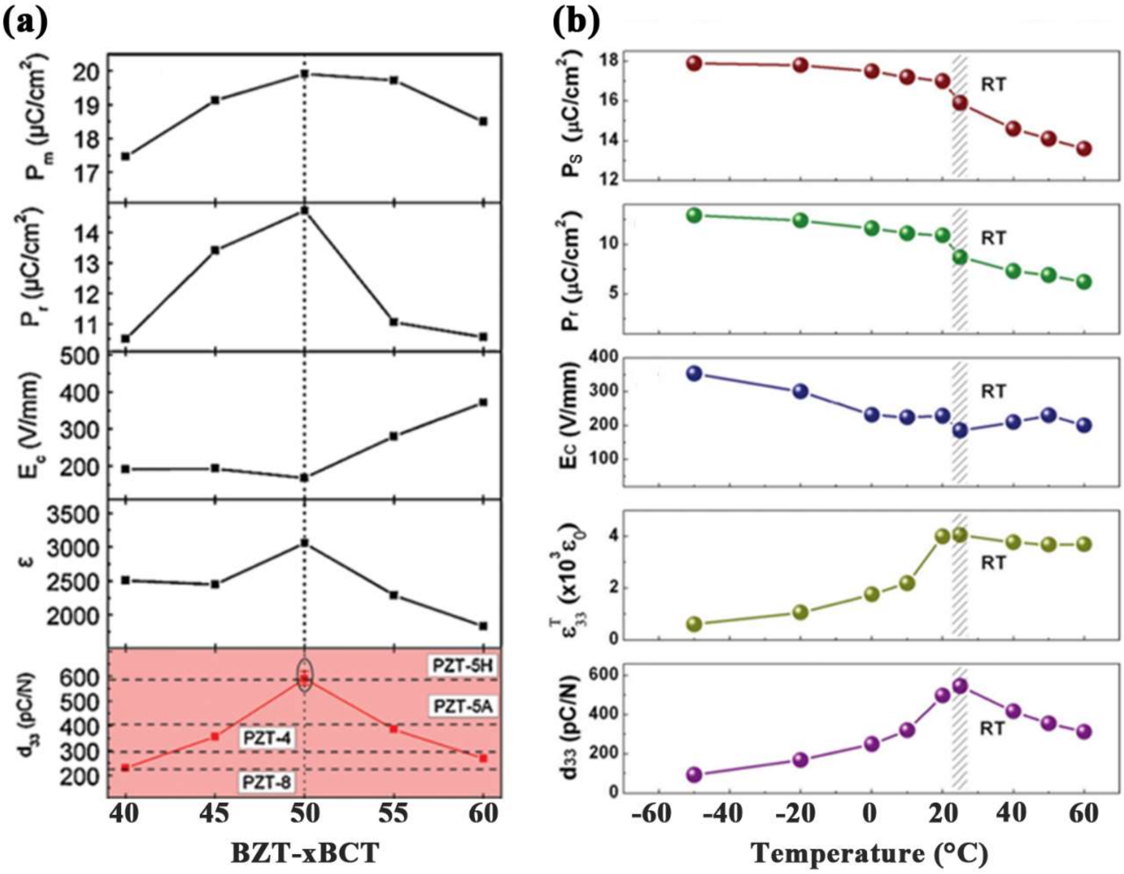

Figure 2.9: (a) Saturation polarization P_m, remanent polarization P_r, coercive field E_c, permittivity ε and piezoelectric coefficients d_{33} of BZT – xBCT as a function of composition [20]. (b) Saturation polarization P_s, remanent polarization P_r, coercive field E_c, permittivity $\varepsilon\varepsilon^T_{33}$ and piezoelectric coefficients d_{33} of BZT – 0.5BCT as a function of temperature [21].

Despite of high piezoelectric properties, BZT – xBCT ferroelectric has a main drawback of low Curie temperature, which restricts its application. For high piezoelectric BZT – 0.5BCT composition T_c = 93 °C [20]. The impact of Zr content on Curie temperature was reported by Bao et al. and Wu et al. [31, 119]. Thereby, a decrease in Zr content resulted in an increase in T_c. Furthermore, it was shown, that increase in Ca content leads to increase of T_c in the BZT – xBCT system [110, 120]. It should be noted that changes in composition lead to the stronger temperature dependence of the PPT and, hence, decreased piezoelectric and dielectric properties along the PPT as a result of stronger deviation from the triple point [31].

Intrinsic and extrinsic contribution to the electromechanical properties of a large variety of BZT – xBCT composition as a function of temperature was investigated by Acosta et al. [23]. The maximum value of piezoelectric coefficients was detected at the O – T PPT, while maximum polarization was peaking at the phase convergence region. It was suggested that the polarization rotation is enhanced around the triple point and PPT, however, the ability of the system to retain its spontaneous polarization determines the final intrinsic properties. Therefore, maximum values of piezoelectric constant were observed only at the orthorhombic – tetragonal phase transition area and not at the phase convergence region. On the other hand, extrinsic contributions peaking around the PPTs were rationalized with a broad minimum in energy barrier [121], leading to alleviated domain switching [122]. Similar results were obtained by Gao et al. [25]. They observed increased values of the intrinsic piezoelectric response around the ferroelectric – ferroelectric phase transition areas, while extrinsic piezoelectric activity is peaking at the phase instability region. An extrinsic contribution to the piezoelectric properties of BZT – xBCT, especially caused by reversible motion of the domain walls, was found to be dominant [25]. These results are in accordance with a report by Zhukov et al. [121], who showed an increased domain wall motion near the PPT as a result of minimum energy barrier for polarization rotation between two ferroelectric phases. However, a high extrinsic piezoelectric response was also observed for rhombohedral BZT – 0.3BCT composition [123]. Therefore, it was suggested that a high extrinsic contribution to the strong piezoelectricity of BZT – xBCT is not a unique feature of PPT compositions.

2.7 *In situ* TEM observations of ferroelectrics

Understanding a real-time dynamic of ferroelectric materials under variable electrical and thermal environments is of great interest. As an external electric field induces changes in domain morphology via polarization switching process, direct observations of structural transformations during electrical poling will greatly facilitate the understanding of structure-property relationship of these materials. It is known, that utilization of ferroelectric devices is limited at elevated temperatures due to phase transformation to paraelectric phase. Therefore, in situ TEM observations of temperature induced phase transitions and its correlation with changes in domain morphology is of significant importance in understanding the properties of these materials at elevated temperatures and can facilitate the development of new devices.

In situ temperature dependent structural studies were performed on a large variety of ferroelectric materials. Temperature influence on the domain structure and strain behavior was investigated for tetragonal and rhombohedral PZT [124]. It was shown that during heat treatment nanodomains formed within microsized domain lamellas and such a configuration remained after cooling to RT. Therefore, at RT the domain configuration of the PZT ceramic before and after annealing differs. Moreover, the influence of the annealing on the strain behavior in this material was studied. The effect of heating on strain for rhombohedral and tetragonal PZT is different. The heating of tetragonal PZT resulted in the increased strain under electric field, while for rhombohedral PZT an enhanced remanent poling strain was observed [124].

The temperature driven crystal structure evolution and its correlation with physical properties of BNT ceramic was investigated by V. Dorcet et.al [125] using in situ TEM technique. It was shown that phase transition from the rhombohedral to tetragonal structure in this material occurs in two steps. At the temperature between 200 °C and 300 °C formation of the modulated phase occurred. This phase consists of orthorhombic sheets of perovskite in the rhombohedral matrix and explains the antiferroelectric property of BNT in this temperature range and also the origin of the relaxor behavior of BNT [125].

In Situ TEM analysis performed on the BNT-xBT ($x = 0.06, 0.11$) solid solution showed a good correlation between structure and property during heating [126]. It was shown that at depolarization temperature (T_d) a dielectric transition is consistent with a structural transformation to *P*4*bm* phase. At that temperature large ferroelectric domains start to disappear and transform to the miniaturized nanodomains. Further increase in temperature does not reveal structural changes at T_{RE} (temperature, where the dielectric frequency dispersion vanishes) and at T_m (temperature, where the dielectric permittivity peaks) [126].

Microstructure evolution of the BZT – xBCT by varying composition and temperature were studied by Gao et al. [27]. For the BZT – 0.4BCT composition with rhombohedral structure they observed typical wedge-shaped microdomains, while lamellar domains on the microscale were a characteristic feature for tetragonal BZT – 0.6BCT [27]. The PPT composition BZT – 0.5BCT showed a unique domain morphology. Nanodomains with an average size of 20 – 100 nm developed within large domain lamellas, forming a domain hierarchy for BZT – 0.5BCT, which coincides with enhanced piezoelectric performance for that composition. Using a convergent beam electron diffraction (CBED) technique Gao et al. showed a coexistence of tetragonal (T) and rhombohedral (R) phases for BZT – 0.5BCT and suggested that an enhanced polarization rotation between T and R phases at nanoscale is responsible for the strong piezoelectric properties of BZT-0.5BCT [27, 28]. Hierarchical domain morphology was previously observed in lead-based materials with high piezoelectric activity such as $Pb(Mg_{1/3}Nb_{2/3})O_3 - xPbTiO_3$ [127-129].

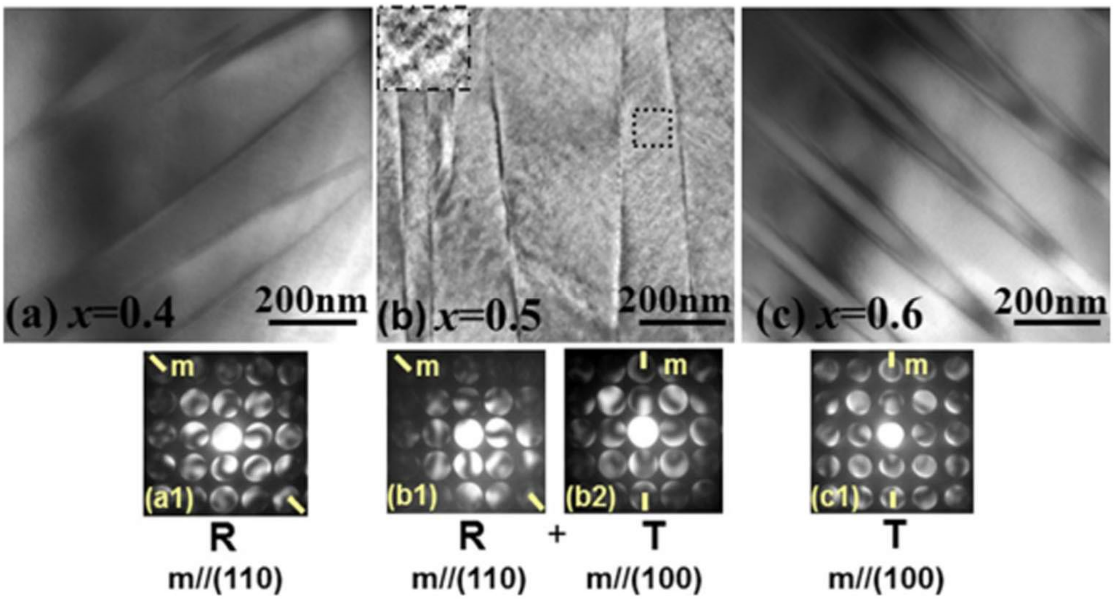

Figure 2.10: TEM observation of composition-induced R – MPB – T transition in BZT – xBCT (T = 25 °C and x = 0.4, 0.5, and 0.6), reported by Gao et al. [27]. The corresponding CBED patterns are displayed below. R and T indicate rhombohedral and tetragonal symmetry, respectively.

In situ electric field TEM technique is very powerful in understanding the microstructural origins for electric field induced phenomena in ferroelectrics. In was shown that the external electric field does not induce noticeable changes in microdomain structure of PZT ceramic, while evolution of nanodomains in response to applied field occurs [130]. The evolution on nanodomains during poling process of PZT was monitored by X. Tan etc. [131]. The polarization alignment and coalescence of nanometer-sized domains were observed under applied electric field for this material.

Recently, in situ TEM observation demonstrated a possibility to destroy or create MPB in BNT-BT through the poling-induced phase transition [132]. These observations correlate well with the piezoelectric properties measured for this material. Authors point out that the creation and destruction of MPBs during field induced ferroelectric-ferroelectric transition is very likely to occur in other perovskite ferroelectrics. Therefore, ferroelectric-ferroelectric transition must be extensively studied in order to understand piezoelectric behavior and its microstructural origins of different systems [132].

Reversible transformation from multi- to single-domain state was reported for BZT – 0.5BCT during electrical poling using *in situ* TEM [29, 30]. Unique single-domain state formation in this material was associated with increased piezoelectric performance. However, rhombohedral BZT – 0.3BCT exhibit an electric-field induced formation of the single-domain state as well [123].Therefore it is not an exclusive feature of the PPT composition.

In this dissertation the temperature and electric field induced microstructure evolution in the lead-free BZT – xBCT piezoceramic is analyzed by means of conventional and *in situ* TEM. Obtained microstructural results are contrasted with strain and polarization measurements in order to understand the potential of this material to replace PZT in certain application.

3. Experimental

Lead-free $Ba(Zr_{0.2}Ti_{0.8})O_3 - x(Ba_{0.7}Ca_{0.3})TiO_3$ piezoelectric ceramic attract a lot of attention due to its enhanced piezoelectric performance. Considering its potential to replace lead-based materials in certain applications, this system was selected for our studies. In this work strain and polarization measurements as a function of electric field are contrasted with TEM findings for a wide compositional range of BZT – xBCT. This chapter will briefly introduce a method for ceramic fabrication and sample preparation procedures as well as characterization techniques used in our study.

3.1 Synthesis and sample preparation procedure

All studied specimens were synthesized in the Nonmetallic – Inorganic group (Prof. Jürgen Rödel) via a conventional solid-state reaction technique. High purity powders of $BaCO_3$ (99.8%), ZrO_2 (99.5%), TiO_2 (99.6%), $CaCO_3$ (99.5%) were mixed according to the stoichiometric formula $Ba(Zr_{0.2}Ti_{0.8})O_3$–$x(Ba_{0.7}Ca_{0.3})TiO_3$ with $x = 0.3$, 0.32, 0.35, 0.4, 0.45, 0.48, 0.5, 0.52 and 0.6. The powders were ball-milled for 5 hours at 250 rpm using yttria stabilized zirconia balls and ethanol in home-made nylon containers in a planetary ball mill (Pulverisette 5, Fritsch GmbH, Germany). These suspensions were dried at 90 °C for 24 hours and then calcined at 1300 °C for 2 hours with a heating rate 5 °C/min. The calcined powders were ball-milled again for 15 hours under identical conditions and cold-isostatically pressed (KIP 100 E, Paul-Otto Weber GmbH, Germany) at 300 MPa into disc-shape samples with a diameter of ~ 10 mm and a thickness of ~ 0.5 – 0.7 mm. The green bodies were sintered at 1500°C for 2 hours with a heating rate of 5 °C/min under atmospheric pressure in covered zirconia crucibles.

For electrical measurements disc-shaped samples of each composition were ground using grinding discs with a successively decreasing grit size 220, 600 and 1200 (MD Piano, Struers GmbH, Germany) and polished using an abrasive paper that had a grit size of 2400 on a semiautomatic grinding and polishing machine (Phoenix 4000, Buehler GmbH, Germany). After that, electrodes were manually applied on both sides of the samples by silver paste (C80415D5, Gwent Electronic Materials Ltd, UK) and burnt in at 400 °C for 2 hours with a heating rate of 2 °C/min (L9/11/S27, Nabertherm GmbH, Germany).

The grain size analysis was performed by M. Acosta using optical microscope (DMRME, Leica Mikroskopie und Systeme GmbH) [23]. In order to obtain the grain boundaries the polished samples of BZT-xBCT system were chemically etched with 50 vol. % diluted HCl and a few drops of HF for 90 s [23]. The determination of the average grain size for each composition was calculated by a linear intercept method using a Lince software [133]. The data of approximately 200 grains for certain composition were considered.

For scanning electron microscopy (SEM) examination the sintered samples were polished using a diamond paper with a grit size of 6, 3, 1, 0.5 µm and 0.05 µm polycrystalline diamond suspension by semiautomatic polishing system (Multiprep^{TM} system, Allied High Tech Products Inc., USA). No chemical or thermal etching was performed prior to SEM analyses.

Specimens for TEM investigation were obtained by conventional sample preparation procedures. Firstly, discs of 3 mm in diameter were ultrasonically cut from as-sintered pellets by ultrasonic disc cutter (Model 601, Gatan, USA). The samples were mechanically thinned to approximately 120 – 150 µm by semiautomatic polishing machine (Multiprep^{TM} system, Allied High Tech Products Inc., USA) using a progressively finer grit of diamond paper (15, 6, 3, 1, 0.5 µm). The final polishing step was performed using 0.05 µm polycrystalline diamond suspension. Polished samples were dimpled to a final thickness of about 20 µm using a Dimple Grinder (Model 656, Gatan, USA). The samples were annealed for 2 hours at 450 °C in order to remove any residual strain induced during the sample preparation. The samples were perforated on both sides by argon ion milling firstly at 5 kV with 16° incidence angle and finally at 4 kV with 12° using a Dual Ion Mill unit (Model 600, Gatan, USA). Schematically the TEM sample preparation procedure is depicted on Figure 3.1. Prior to conventional and *in situ* hot- and cold-stage TEM examinations the specimens were coated with carbon in order to minimize charging under the incident electron beam.

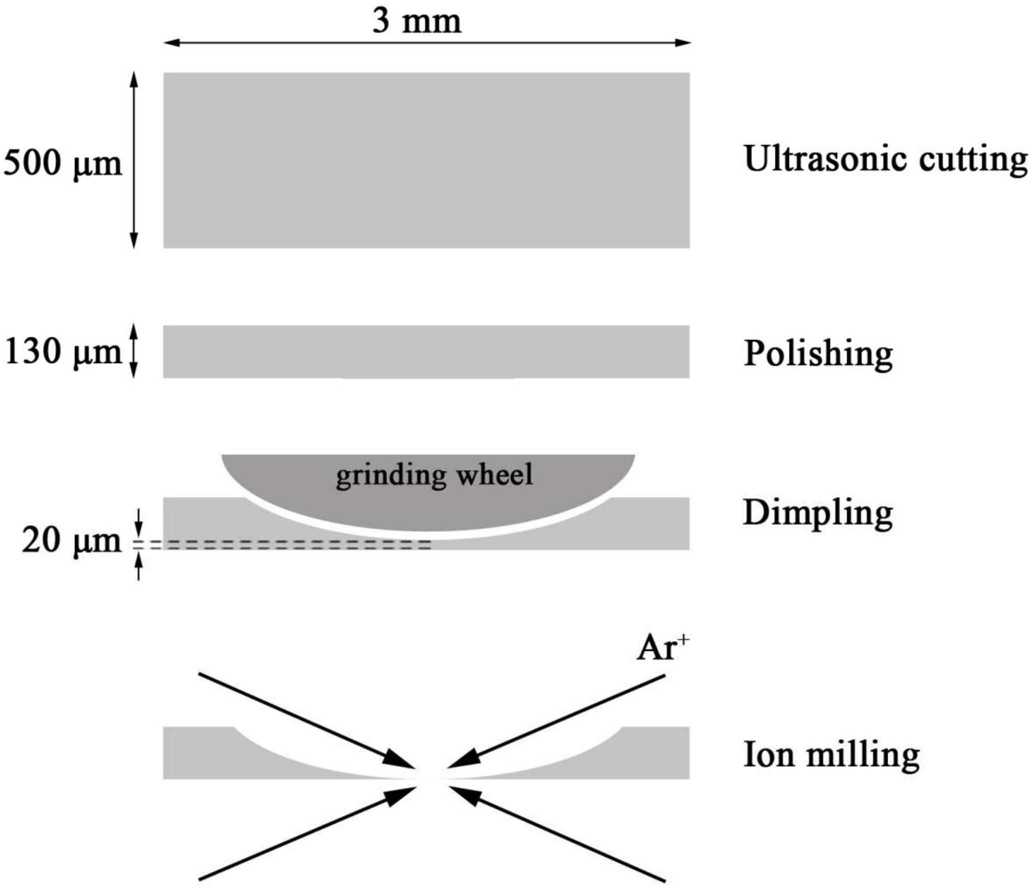

Figure 3.1: TEM sample preparation procedures: ultrasonic cutting, polishing, dimpling, ion milling.

3.2 Strain and polarization measurements

Room temperature ferroelectric strain and polarization hysteresis loops of BZT-xBCT system were obtained by using a modified Sawyer-Tower circuit equipped with an optical strain measurement setup (Figure 3.2). This circuit includes a standard capacitor (C_0) in a series with ferroelectric sample (C_s). The value of capacitance C_0 should be much higher than C_s in order to minimize the voltage drop U_0 at standard capacitor. In our studies the capacitance C_0 = 10 µF was chosen, which was more than three orders of magnitude larger than C_s. As both capacitors are in a series, the charge Q in the standard and sample capacitors must be the same (Kirchhoff's first law), so $Q = C_s \cdot U_s = C_0 \cdot U_0$. Therefore, the charge Q on the sample capacitor can be determined by measuring the voltage drop U_0 across C_0. Polarization P of the sample can be calculated as charge Q divided by area A ($P = Q/A = C_0 \cdot U_0/A$). To be more precise, Q/A gives a displacement D, however, for high values of P and D we can approximate $D \approx P$.

Polarization loops were measured by applying triangular waves of 3 kV/mm with frequencies of 0.01 – 50 Hz using a function generator and a voltage amplifier (High Voltage Amplifier 20/20C, Trek Inc.).

Four-channel-oscilloscope was used to register the voltage drop across the standard capacitance. Simultaneously, strain measurements were performed using an optical displacement sensor (Model D63, Philtec Inc.).

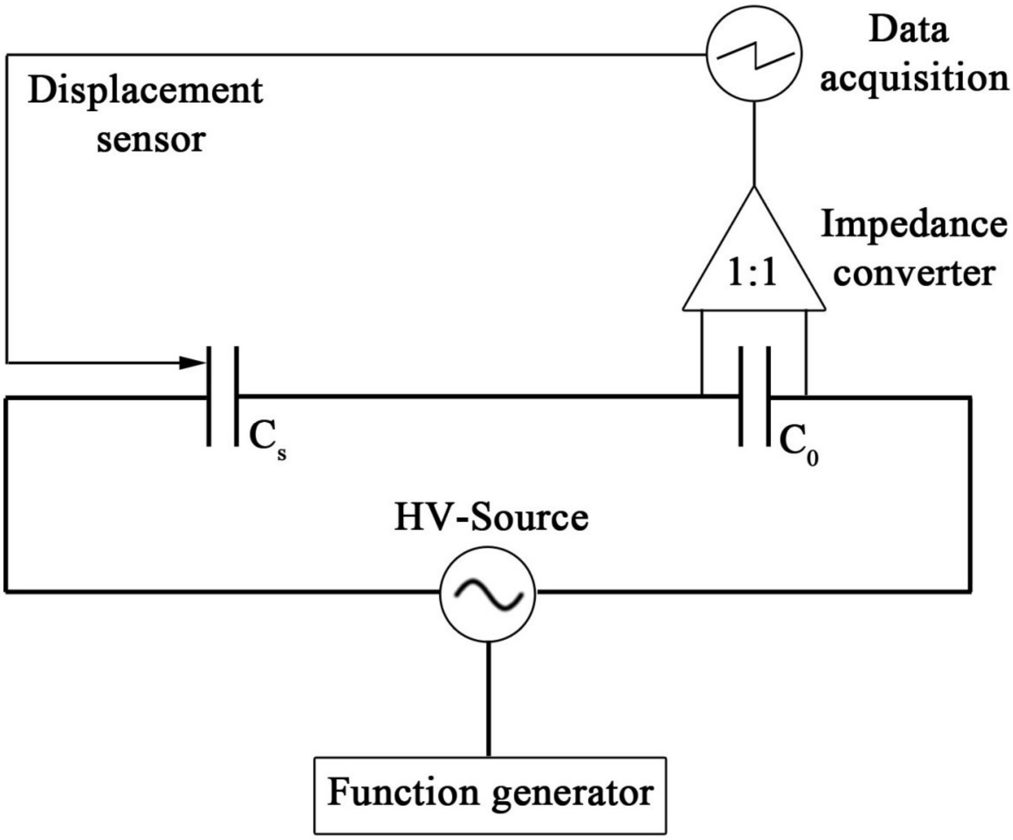

Figure 3.2: Schematic view of the Sawyer-Tower circuit used for room temperature strain and polarization measurements.

3.3 Scanning Electron Microscopy studies

In the SEM a surface of the specimen is scanned by focused beam of electrons. Large variety of signals is produced by electron-sample interaction, which can be detected and produce image or elemental composition of the sample. Therefore, SEM provides information about specimen surface and composition. Main signals, which are used in the SEM are secondary electrons (SE), backscattered electrons (BSE) and X-rays. Low energy SE are emitted by atoms near the surface of the specimen by inelastic scattering [134]. SE are registered by Everhart-Thornley detector [135] and produce an image of the surface on the video display. BSE are high energy electrons of a primary beam, which is reflected from the atom in the specimen by an elastic scattering. The atomic number of the elements determines the contrast on the image. Light elements will appear darker in the image in comparison with heavy elements because heavy elements backscatter stronger.

An energy dispersive X-ray spectroscopy (EDX) allows identifying particular elements and their relative proportions. A characteristic X-ray emission from the specimen is generated by the interaction of the high energy electron beam with atoms of the specimen. An incident beam creates an electron hole in the inner shell, which will be filled by the electron from the outer, higher energy shell. The difference in energy between these two shells is released in the form of X-rays, which is characteristic for a particular element. Therefore, energy dispersive X-ray spectroscopy (EDX) allows identifying particular elements and their relative proportions.

Chemical analyzes for a full range of BZT-xBCT compositions were performed using the scanning electron microscope Jeol JSM 7600F equipped with an SE, BSE and EDX detectors under 8 kV accelerating voltage.

3.4 Transmission Electron Microscopy studies

TEM is one of the most powerful methods in microstructural characterization of materials. Electron microscopes were developed because of the resolution limit in optical microscopy, which is determined by the wavelength of visible light. Nowadays different TEM techniques as High Resolution TEM (HRTEM), Scanning TEM (STEM), Energy-Filtered TEM (EFTEM), EDX etc. are available. *In situ* TEM enabled to visualize changes in material properties under performance in real time e.g. as a function of electric field or temperature. In this chapter applied TEM techniques, such as conventional, *in situ* hot-stage, *in situ* cold-stage, *in situ* electric-field and *in situ* electric-field with simultaneous cooling TEM techniques, will be briefly described.

3.4.1 Conventional, *in situ* hot- and cold-stage TEM techniques

In a TEM the electrons, emitted by an electron source, are accelerated to a high energy level and focused on a material by electromagnetic lenses. When an electron beam interacts with a specimen, a wide range of secondary signals, which can be used in analytical microscopy, are generated. Conventional TEM uses only forward scattered electrons. Due to forward scattering through the specimen we see a diffraction pattern (DP) or an image of an object on the viewing screen. Objective lens is the most important lens in the TEM. It forms DP on the back focal plane and an image of the specimen on the image plane, which are magnified and projected onto a viewing screen by the imaging system of the microscope [136].

Conventional TEM observations were carried out on Philips CM-20 and Jeol Jem 2100F microscopes with an accelerating voltage of 200 kV using double tilt specimen holders (PW6595/05, FEI, Netherlands and EM-31640, Jeol, Japan, respectively). *In situ* hot-stage experiments were performed on Jeol Jem 2100F at 200 kV with a double tilt heating holder (Model 652, Gatan, USA). The temperature was controlled through the SmartSet Hot Stage controller (Model 901, Gatan, USA). *In situ* hot-stage TEM studies were conducted in a temperature range from 22 to 130 °C using heating and cooling rates of 5 – 10 °C/min. *In situ* cooling experiments were carried out on Philips CM-20 instrument operating at 200 kV with the double tilt liquid nitrogen cooling holder (Model 636, Gatan, USA) in the temperature range of -30 – 97 °C. Prior to the experiment, the liquid nitrogen dewar of the holder was evacuated for approximately 5 – 7 hours. Bright field (BF) images and selected area electron diffraction (SAED) patterns during in-situ hot- and cold-stage TEM studies were recorded approximately 10 min after stabilization of the certain temperature.

3.4.2 *In situ* electric-field and *in situ* electric-field plus cold-stage TEM techniques

For *in situ* electric-field investigations semicircular Au electrodes, separated by 100 – 150 µm, were sputtered on the flat surface of each specimen. Electroded specimen was glued to the sample holder tip with an insulating varnish and connected to the electrical contacts on the holder with Pt wires. Figure 3.3 illustrates the experiment configuration of the electrodes geometry (Figure 3.3 (a)) and the tip of the holder with a glued and contacted specimen (Figure 3.3 (b)).

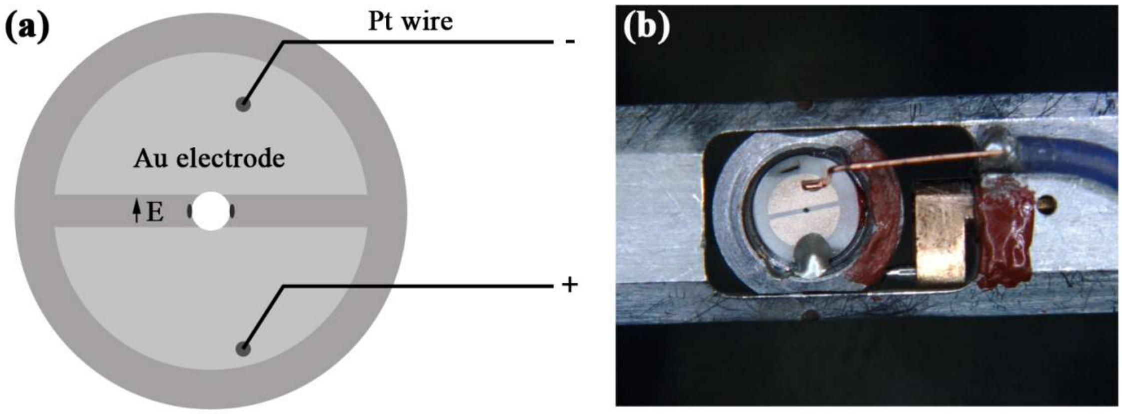

Figure 3.3: Experiment configuration of the in situ electric-field TEM studies. (a) Scheme of the electrode geometry, (b) TEM holder tip with a glued and contacted specimen.

In situ electric-field TEM studies were performed with a Philips CM-20 operated at 200 kV and a Philips CM-30 operated at 200 and 250 kV. The specimen was glued into the holder tip of the modified double tilt electric-field TEM specimen holder (Model 652, Gatan, USA) as described above. According to the geometry of the electrodes, the electric field was perpendicular to the incident electron beam (Figure 3.3 (a)). It should be noted that the electric field strength in the TEM specimen is not uniform due to presence of the central perforation [29, 30, 131]. Therefore, values of electric field reported in the present work are nominal, which was calculated as the applied voltage divided by the spacing between electrodes. Maximum applied nominal voltage in our studies was ±500 V. The actual value of electric field is intensified by the factor of two at the edges of the circular perforation (two areas highlighted in Figure 3.3 (a)) [131]. All *in situ* electric-field studies were performed within these two areas.

In situ electric-field plus cold-stage TEM observations were carried out on Tecnai G2 F20XT operated at 200 kV, using a modified single tilt (Model 626, Gatan, USA) cryo-transfer holder. The specimen geometry and the experiment configuration coincide with previously explained *in situ* electric-field studies. The *in situ* cold-stage experiments with simultaneously applied electric-field were performed using liquid nitrogen cooling in a temperature range of -30 – 50 °C. In order to provide a thermal insulation, the specimen holder dewar was evacuated for approximately 10 – 12 hours prior to TEM investigations. The highest applied voltage was ±500 V.

3.5 Calculation of the reflection splitting

The diffraction patterns of BZT-xBCT were calculated by R. Schierholz with MATLAB (MathWorks, Nattick, MA, USA) using the lattice parameters originally reported by Liu and Ren (tetragonal, a = 4.007Å and b = 4.025 Å; rhombohedral, a = 4.009Å and α = 89.88°) [20]. The MATLAB code, which was used for calculation was written by R. Schierholz and can be found in the Appendix A of [137]. In addition to the graphical representation of the diffraction patterns, the reflection splitting caused by rhombohedral and tetragonal domains in $<001>_c$, $<011>_c$ and $<111>_c$ zone axis was defined. It should be noted that indexing of diffraction parents and directions of the reflection splitting were performed based on cubic coordinate system. The amount of reflection splitting on the SAED was calculated by the following equation:

$$S = \frac{|(g_{hkl1} - g_{hkl2}) - (g_{hkl1} - g_{hkl2}) \cdot [uvw]|}{|g_{hkl}|} \qquad 9$$

where [uvw] is a vector, parallel to the zone axis; and g_{hkl1} and g_{hkl2} are a pair of reflections with the largest splitting for a certain zone axis [44].

4. Results

In recent years BZT – xBCT piezoelectric ceramics were widely studied [23, 27, 31, 32, 117]. Special attention was given to the PPT composition BZT – 0.5BCT [25, 28-30, 115, 138, 139], which exhibits impressive piezoelectric performance (d_{33} = 620 pC/N), which is comparable to PZT [20]. However, in order to understand the structural property relationship and the potential of this material to replace PZT in certain application it is necessary to investigate a full range of BZT – xBCT compositions. It should be noted that BZT – xBCT piezoceramic has a major drawback of low Curie temperature, ranging between 60°C and 95°C depending on composition [20, 23, 32], which restricts its practical utilization. Nevertheless, it is important to understand the behavior of this material under various temperatures in order to optimize and improve its application.

This chapter will present the electrical properties and microstructural features of a broad variety of BZT – xBCT. In order to visualize the real time microstructural evolution, the domain structure as a function of temperature and electric field was monitored *in situ* using TEM.

4.1 Electrical properties

Electrical properties of BZT – xBCT system are strongly composition dependent. Figure 4.1 represents room temperature polarization and strain loops as a function of electric field for BZT – xBCT (x = 0.30, 0.52, 0.60). For all compositions P – E loops exhibit a typical hysteresis character. Increase in the BCT content causes a broadening of the polarization loops (Figure 4.1 (a) – (c)). A coercive field (E_c), saturation polarization (P_s) and remanent polarization (P_{rem}) were derived from bipolar P – E hysteresis loops. Bipolar S – E loops with a typical "butterfly" shape were used to examine the maximum and negative strain (S_{max} and S_{neg}, respectively).

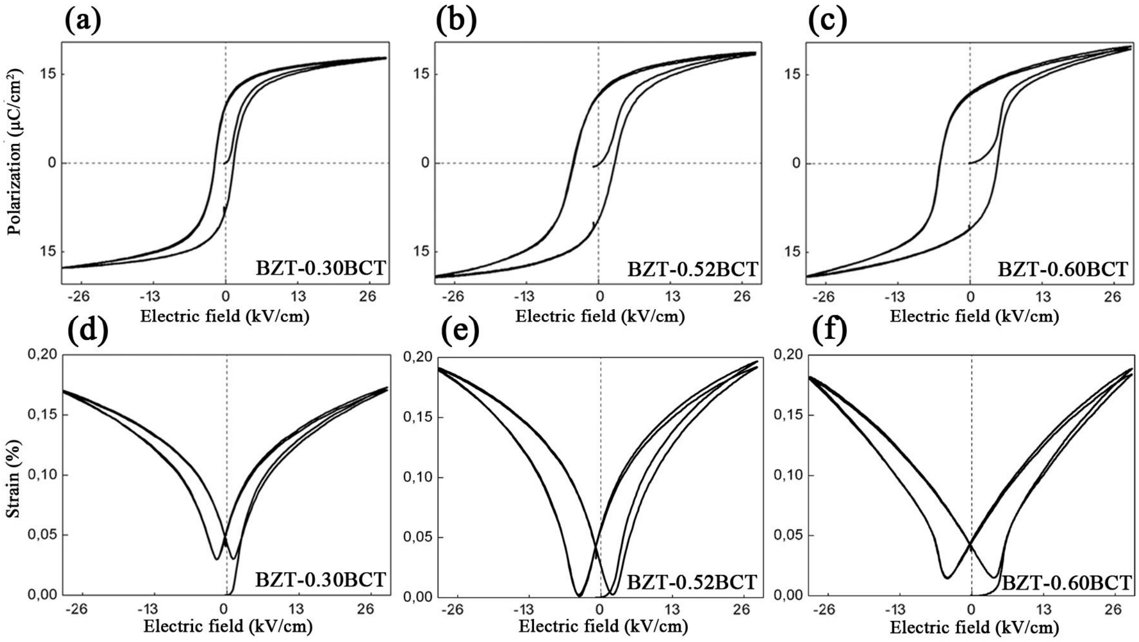

Figure 4.1: (a) - (c) Room temperature P – E hysteresis loops and (d) – (f) room temperature bipolar S – E loops of BZT-0.3BCT, BZT-0.52BCT and BZT-0.6BCT, respectively 140.

Large signal parameters obtained from bipolar P – E and S – E loops as a function of composition for a wide range of BZT – xBCT (x = 0.30, 0.32, 0.40, 0.45, 0.5, 0.52, 0.60) are depicted in Figure 4.2. The minimum value of the coercive field is 1.8 kV/cm, which was obtained for the rhombohedral BZT-0.3BCT. This value increases with BCT content and reaches its maximum of 5.6 kV/cm for the BZT-0.6BCT, which exhibits a tetragonal symmetry (Figure 4.2 (a)). The saturation and the remanent polarization are increased for the PPT compositions BZT-0.45BCT (P_s = 18.67 μC/cm^2, P_{rem} = 11.71 μC/cm^2) BZT-0.5BCT (P_s = 18.88 μC/cm^2, P_{rem} = 11.88 μC/cm^2) and BZT-0.52BCT (P_s =18.41 μC/cm^2, P_{rem} = 11.67 μC/cm^2). These parameters decrease for the compositions, which is located more far away from the PPT (Figure 4.2 (b), (c)). Maximum and negative strain (S_{max} and S_{neg}, respectively) as a function of composition were measured from bipolar strain loops. The largest values of S_{max} and S_{neg} were reached in rhombohedral BZT-0.4BCT (S_{max} = 0.183 %, S_{neg} = 0.047 %) and in tetragonal BZT-0.52BCT (S_{max} = 0.182 %, S_{neg} = 0.047 %) close to the PPT. For the BZT-0.5BCT the negative strain is enhanced as well (S_{neg} = 0.046 %), while the maximum strain is significantly lower (S_{max} = 0.152 %). BZT-0.45BCT shows a decrease on both of these parameters. A decrease in S_{max} and S_{neg} for these compositions can be attributed to the presence of an orthorhombic phase.

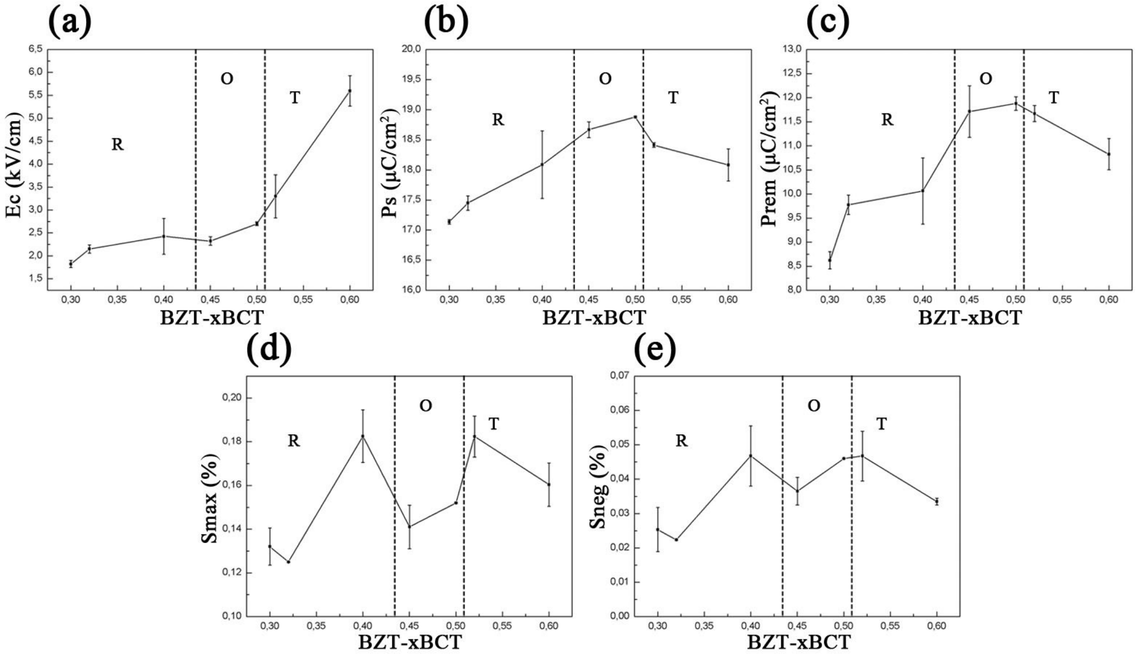

Figure 4.2: (a) coercive field E_c, (b) saturation polarization P_s, (c) remanent polarization P_{rem}, (d) maximum strain S_{max} and (e) negative strain S_{neg} as a function of composition. Dashed lines indicate phase boundaries between phases (R – rhombohedral, O – orthorhombic, T – tetragonal) [140].

4.2 SEM and EDX analysis

Grain size analysis of all BZT-xBCT compositions was calculated using the linear intercept method [133] by M. Acosta and listed in Table 2.2 [23]. Grain size was found to vary from 20 ± 3 µm for BZT-0.32BCT to 36 ± 9 µm for BZT-0.45BCT.

Table 4.1: Grain size analysis of BZT-xBCT [23].

Material	Average grain size, µm
BZT-0.3BCT	28 ± 7
BZT-0.32BCT	20 ± 3
BZT-0.35BCT	36 ± 8
BZT-0.37BCT	28 ± 8
BZT-0.4BCT	25 ± 5
BZT-0.45BCT	36 ± 9
BZT-0.5BCT	35 ± 8
BZT-0.6BCT	26 ± 6

In order to verify a compositional homogeneity of each sample an EDX analyses has been performed using SEM. EDX profiles are shown in Appendix I. It can be clearly seen that the weight percent of Zr decreases and the weight percent of Ca increases with increasing the BCT content (Figure 4.3). These results are in a good agreement with weight percentage of each element, calculated from the stoichiometric formula (Appendix I). Therefore, the phase composition of synthesized material is proved by the EDX profiles.

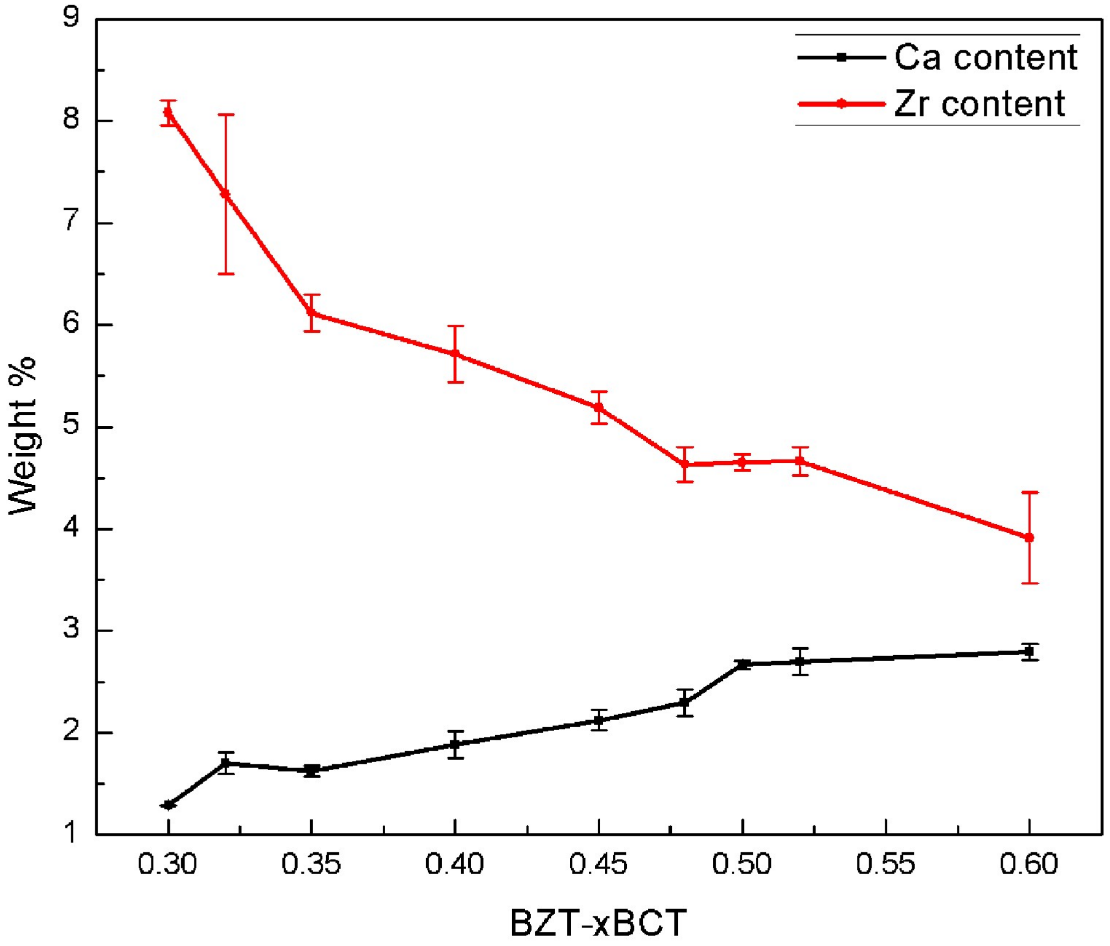

Figure 4.3: Experimental results of Zr and Ca content as a function of composition for BZT-xBCT based on EDX analysis.

4.3 Calculation of the reflection splitting on the SAED

The SAED patterns for tetragonal domains calculated by R. Schierholz are depicted in Figure 4.4. The reflection splitting for rhombohedral 71° and 109° domains with walls in {100}c and {110} planes (nomenclature is from Ricote et al. [45]), respectively, was found to be very small. The largest splitting produced by 71° domains was obtained in [0-11] and by 109° domains in [1-10] and in [1-11] zone axes and achieved s = 0.0024. For tetragonal 90° domains in the [001] crystallographic orientation the amount of reflection splitting was maximum, s = 0.0079 (Figure 4.4 (a)). This value decreased down to s = 0.0056 for the [0-11] zone axis (Figure 4.4 (b)) and down to s = 0.0046 for [111] (Figure 4.4 (c)) and [1-11] orientations. Even smaller splitting of the reflections was observed for other crystallographic orientations.

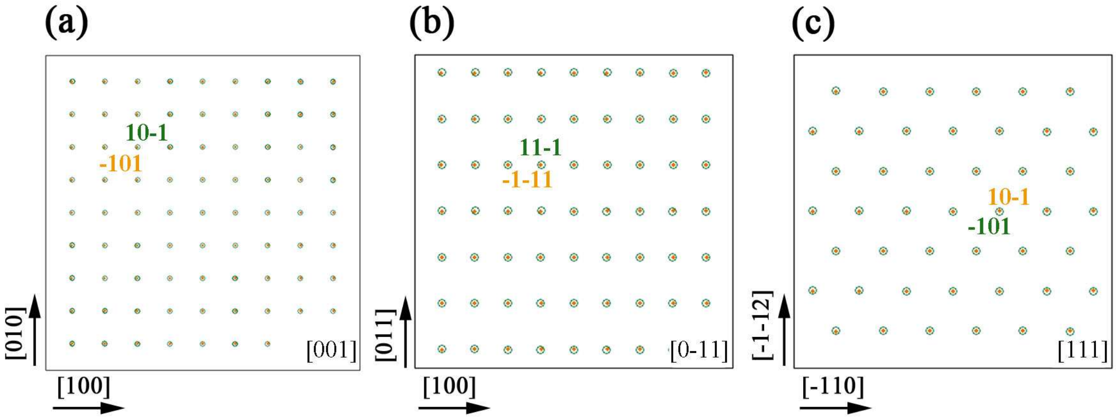

Figure 4.4: Calculated SAED patterns for tetragonal 90° domains along the (a) [001] zone axis. (b) [0-11] zone axis. (c) [111] zone axis. Reflections, which are used for calculation of the parameter s, are indicated (green and orange) [140].

4.4 Conventional TEM investigations

It is known that ferroelectric domains play an important role in the dielectric, piezoelectric and ferroelectric properties of materials [6, 27, 60]. However, composition dependent studies of the domain morphology in the BZT – xBCT system are very rare in the literature. In this chapter the domain structure evolution in the BZT – xBCT piezoceramic is discussed as a function of composition for x = 0.3, 0.32, 0.35, 0.4, 0.48, 0.6 at room temperature.

Lamellar needle-shaped (or wedge-shaped) domains with an average width of 230 nm ± 30 nm are representative for the rhombohedral BZT – 0.3BCT (Figure 4.5 (a)). Such domain configuration appears due to misorientation of domain walls with respect to the predicted twinning planes [45]. Domains with wedge-shaped tips are very typical for rhombohedral PZT [45]. In the lower left corner of the Figure 4.5 (a), very few domains, which are miniaturized down to the nanoscale level can be observed. It should be noted that no signs of ferroelectric domains were found within some grains. Grain imaged along its $[0\text{-}11]_c$ zone axis with an average size of 1.7 µm shows a homogeneous contrast (Figure 4.5 (b)). No evidence of the reflection splitting or presence of superstructure reflections were observed in the corresponding SAED pattern (Figure 4.5 (b), inset).

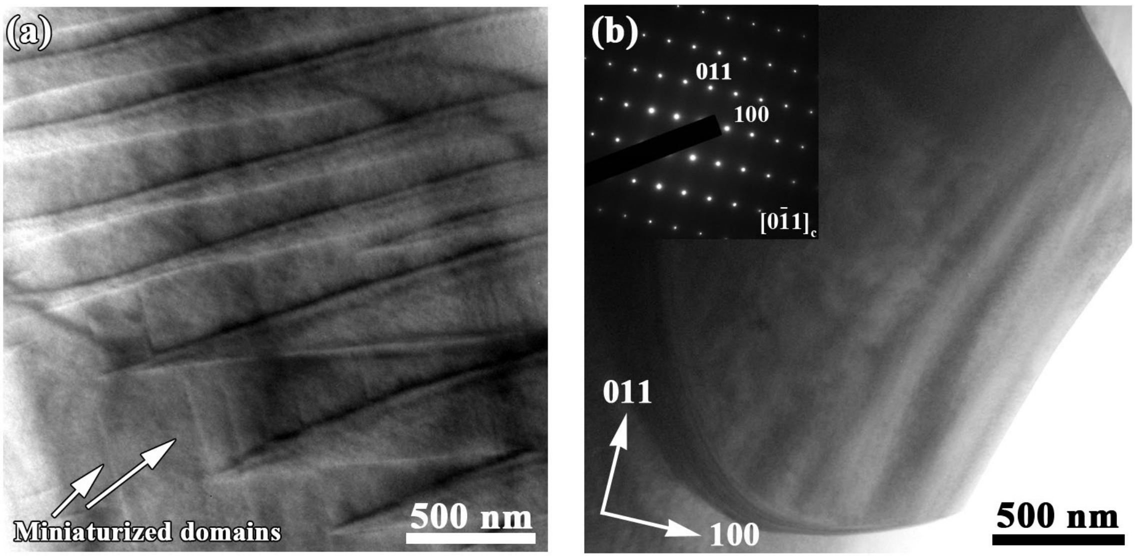

Figure 4.5: TEM bright field images of the BZT – 0.3BCT. (a) Grain with a needle-shaped domain structure. (b) Grain with a homogeneous contrast imaged along the $[110]_c$ zone axis. In the inset of (b), the corresponding SAED pattern is depicted.

Figure 4.6 represents a domain configuration observed for rhombohedral BZT – 0.32BCT. Needle-shaped domains with tips pointing in [01-3] and [-3-20] directions are visible inside the grain, imaged along the $[-231]_c$ zone axis (Figure 4.6 (a)). Rhombohedral edge-on domains with (011) and (100) walls, viewed along $[0-11]_c$, which correspond to the presence of 109° and 71° domains [45], respectively, are shown in Figure 4.6 (b). Within 109° domains further contrast can be observed (Figure 4.6 (b)). This contrast was identified as miniaturized domains with (110) walls, inclined by 30° with respect to the electron beam. An average domain width for that composition was found to be 205 nm ± 45 nm. Corresponding SAED patterns did not show any reflection splitting (Figure 4.6 (insets)). This is attributed to very small distortions from the cubic symmetry. As a consequence, a very tiny peak splitting cannot be detected in the SAED patterns due to its resolution limit.

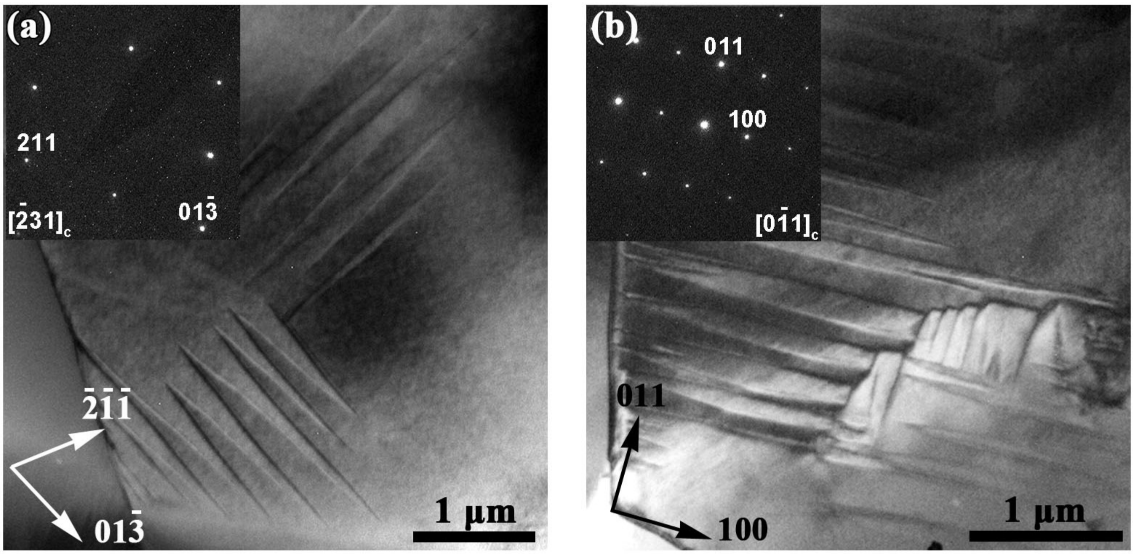

Figure 4.6: TEM bright field images of the BZT – 0.32BCT. (a) Grain with needle-shaped domains imaged along the [-231]$_c$ zone axis. (b) Grain with needle-shaped and nanometer-sized domains imaged along the [0-11]$_c$ zone axis. In the insets, the corresponding SAED patterns are depicted.

Edge-on rhombohedral 109° domains with walls along (011) planes (area A) and domain walls, which do not follow any particular crystallographic direction (area B), are visible within the grain imaged along its [0-11]$_c$ zone axis for the BZT – 0.35BCT (Figure 4.7 (a)). At the central part of the grain a crystallographic twin, interpenetrated by ferroelectric domains, can be observed. The inset of Figure 4.7 (a) is a corresponding SAED pattern, where twin and matrix reflections are abbreviated as T and M, respectively. Figure 4.7 (b) displays a grain occupied by lamellar domains with needle-shaped tips, pointing in [-100] direction. These sets of domains have walls in (011) planes, which corresponds to 109° domains. Miniaturized domains with (110) walls inclined by 30° to the beam can be visible in the lower part of the Figure 4.7 (b). The average width of the ferroelectric domains for that composition is 140 nm ± 28 nm. As in the previous case, the splitting of the electron diffraction spots was not detected on the corresponding SAED patterns as well. (Figure 4.7 (a), (b)).

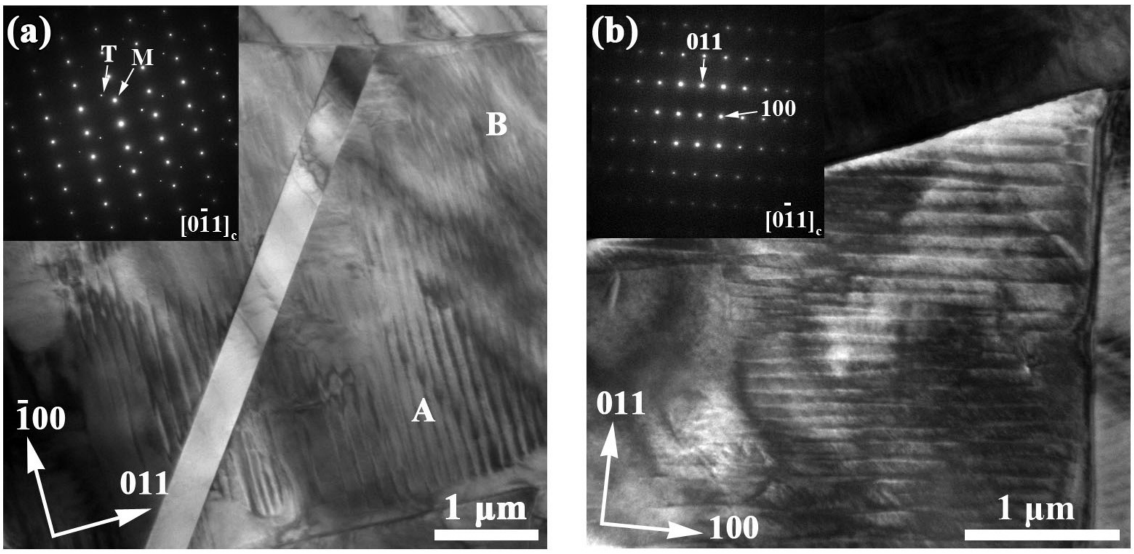

Figure 4.7: TEM bright field images of the BZT – 0.35BCT along the [0-11]$_c$ zone axis. (a) Grain occupied by 109° domains (area A) and domains, which do not follow any crystallographic direction (area B). In the inset, the corresponding SAED patterns are depicted. Twin and matrix reflections on the SAED pattern are denoted as T and M, respectively. (b) Grain occupied by 109° domains with needle-shaped tips. In the inset, the corresponding SAED pattern is depicted.

Figure 4.8 displays TEM bright field images of the BZT – 0.40BCT, which exhibit a rhombohedral structure at room temperature. Within the grain imaged along its [112]$_c$ zone axis domain walls with traces running in [201] and [02-1] directions are visible (Figure 4.8 (a)). The width of these domains is 130 nm ± 49 nm. Further contrast inside domain lamellas indicates the presence of miniaturized ferroelectric domains. Figure 4.8 (b) displays the grain viewed along its [111]$_c$ zone axis occupied by wedge-shaped domains with curved walls, which are 265 nm ± 41 nm in width. As the BZT – 0.40BCT composition locates close to the R – O PPT region, appearance of such curved domain walls can be related to the presence of an additional (orthorhombic) phase. As before, the SAED patterns, displayed in the insets of Figure 4.8 (a), (b), do not show any reflection splitting.

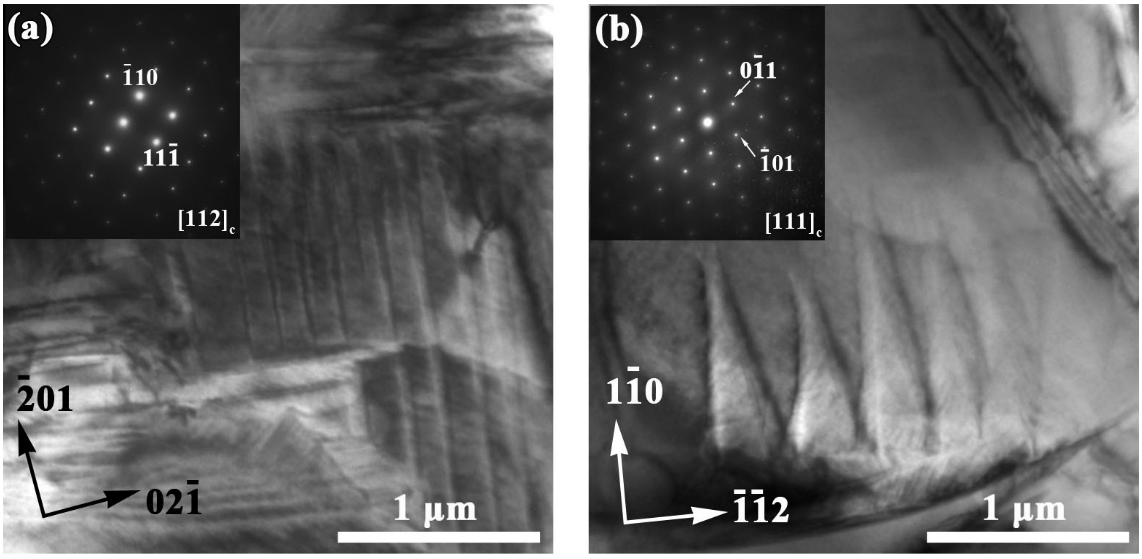

Figure 4.8: TEM bright field images of the BZT – 0.4BCT. (a) Grain with lamellar domains imaged along the $[112]_c$ zone axis. (b) Grain with wedge-shaped domains imaged along $[111]_c$ zone axis. In the insets, the corresponding SAED patterns are depicted.

The domain morphology of the PPT composition BZT – 0.48BCT is depicted in Figure 4.9. Parallel domain strips with the width of around 311 ± 42 nm and ferroelectric domains with the width of several to tens of nm form a herringbone domain configuration (Figure 4.9 (a)). Such a domain structure is a typical feature of the MPB compositions in the Pb-based systems [127-130, 141, 142]. Miniaturized domains assembled into lamellar domains have been also observed in the MPB- and the PPT-type lead-free piezoelectric ceramics [27, 29, 139, 143, 144]. Gao et al. showed that hierarchical domain morphology in the BZT – 0.5BCT system coincides with a strong piezoelectricity of the BZT – xBCT piezoceramic [27]. Other grains contain elongated domains with a small width of 117 ± 5 nm and wedge-shaped domains with 200 ± 20 nm in width (Figure 4.9 (b)).

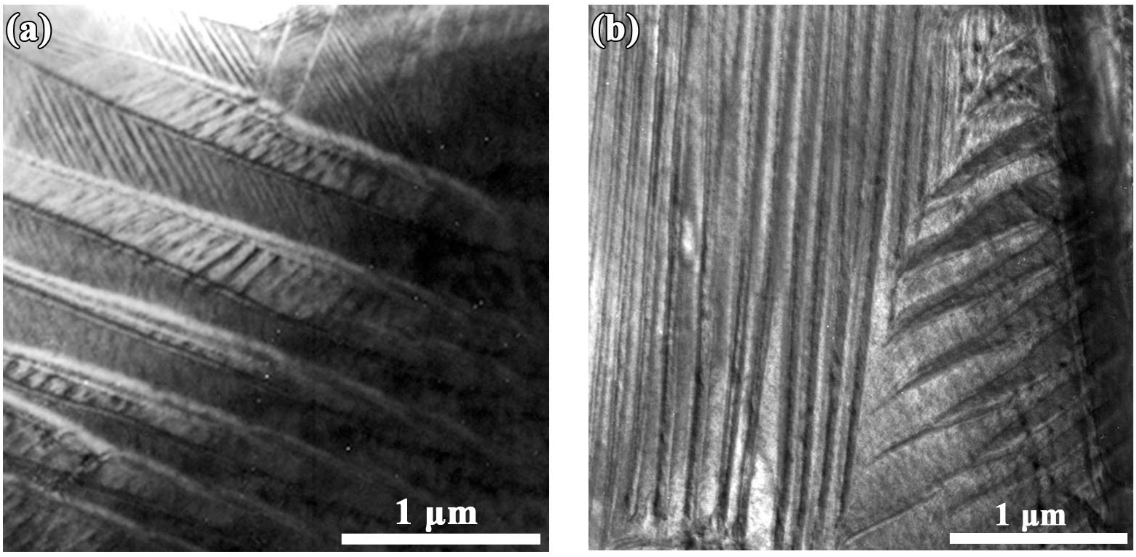

Figure 4.9: TEM bright field images of the BZT – 0.48BCT. (a) Grain with herringbone domain morphology. (b) Grain with thin domain lamellas and wedge-shaped domains.

Lamellar ferroelectric domains are dominated for the tetragonal BZT – 0.6BCT composition. Figure 4.10 (a) shows a lamellar domain configuration with the walls inclined by about 54° to the electron beam. The average width of such domains is 375 ± 67 nm. Formation of needle-shaped tips was observed at the contact area between two sets of ferroelectric domains (Figure 4.10 (b)). The inset of the Figure 4.10 (a) is a corresponding SAED pattern. Splitting of the reflections was not detected due to small tetragonal distortions.

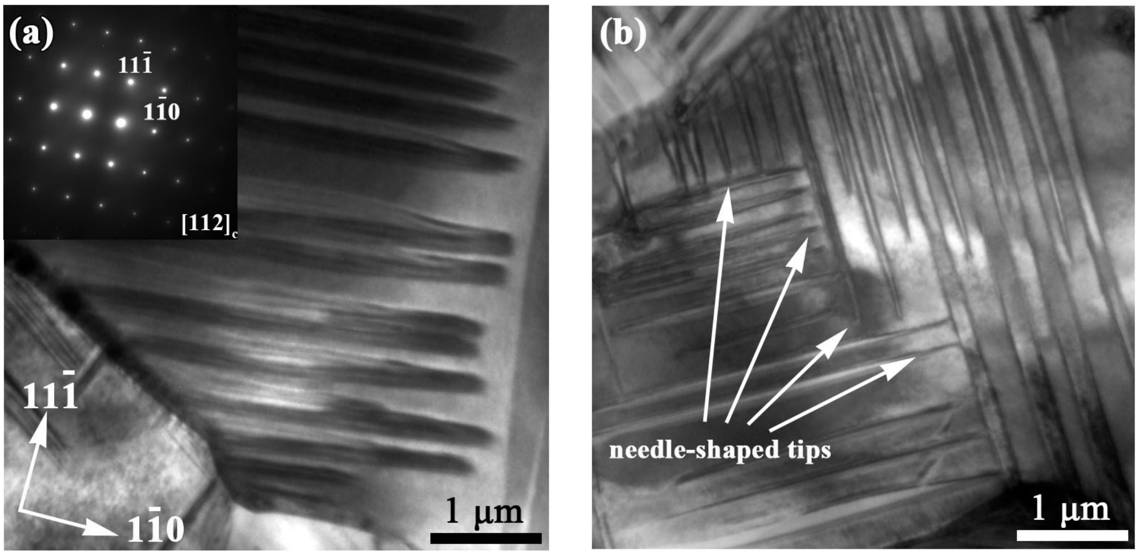

Figure 4.10: TEM bright field images of the BZT – 0.6BCT. (a) Lamellar domain configuration viewed along $[112]_c$ zone axis. Inset is a corresponding SAED pattern. (b) Domains with needle-shaped tips. In the inset of (a), the corresponding SAED pattern is depicted.

The domain morphology evolution during R → O → T transition, when varying the composition, was investigated using TEM. Wedge-shaped domains are a representative feature for rhombohedral BZT – xBCT systems. A miniaturized down to nanoscale level domain structure was found within some wedge-shaped domains. Additionally, grains free of visible ferroelectric domains, which exhibit a homogeneous contrast, were also observed. It should be noted that for the rhombohedral BZT – xBCT, domains with {110} – type walls were observed more frequently than {100} – type domains. The BZT – xBCT composition close to R – O phase boundary exhibits ferroelectric domains with curved walls, which do not follow any particular crystallographic direction. For compositions belonging to the orthorhombic phase hierarchical domain structure with miniaturized domains within lamellar microdomains is a characteristic feature. This observations coincided with the results obtained by Gao et al. [27, 28]. In contrast to that, for tetragonal compositions the characteristic domain morphology was composed of large lamellar domains. Due to the resolution limit, SAED patterns for all compositions are devoid of any reflection splitting.

4.5 In situ temperature dependent TEM investigations

As mentioned before, lead-free BZT – xBCT perovskite ferroelectrics are of great interest due to its non-toxicity and enhanced piezoelectric and dielectric properties [20-26]. Figure 4.11 displays a phase diagram of the BZT – xBCT determined from the measurements of dielectric permittivity by M. Acosta et al. [23], which is in a good agreement with the phase diagram obtained from synchrotron x-ray powder diffraction by Keeble et al. [32]. Green squares denote the compositions, which were studied in the present work. Hence, BZT – xBCT, for a given x, exhibits up to three temperature induced phase transitions from high temperature cubic (C) to tetragonal (T), orthorhombic (O) and rhombohedral (R) phases (Figure 4.11) [23, 32]. Recently, the existence of an O phase was also confirmed by the group of Prof. Ren [117]. This chapter presents the thermally driven structural transitions in the BZT – xBCT with x = 0.4, 0.45, 0.5 and 0.6 monitored by means of *in situ* hot- and cold-stage TEM techniques.

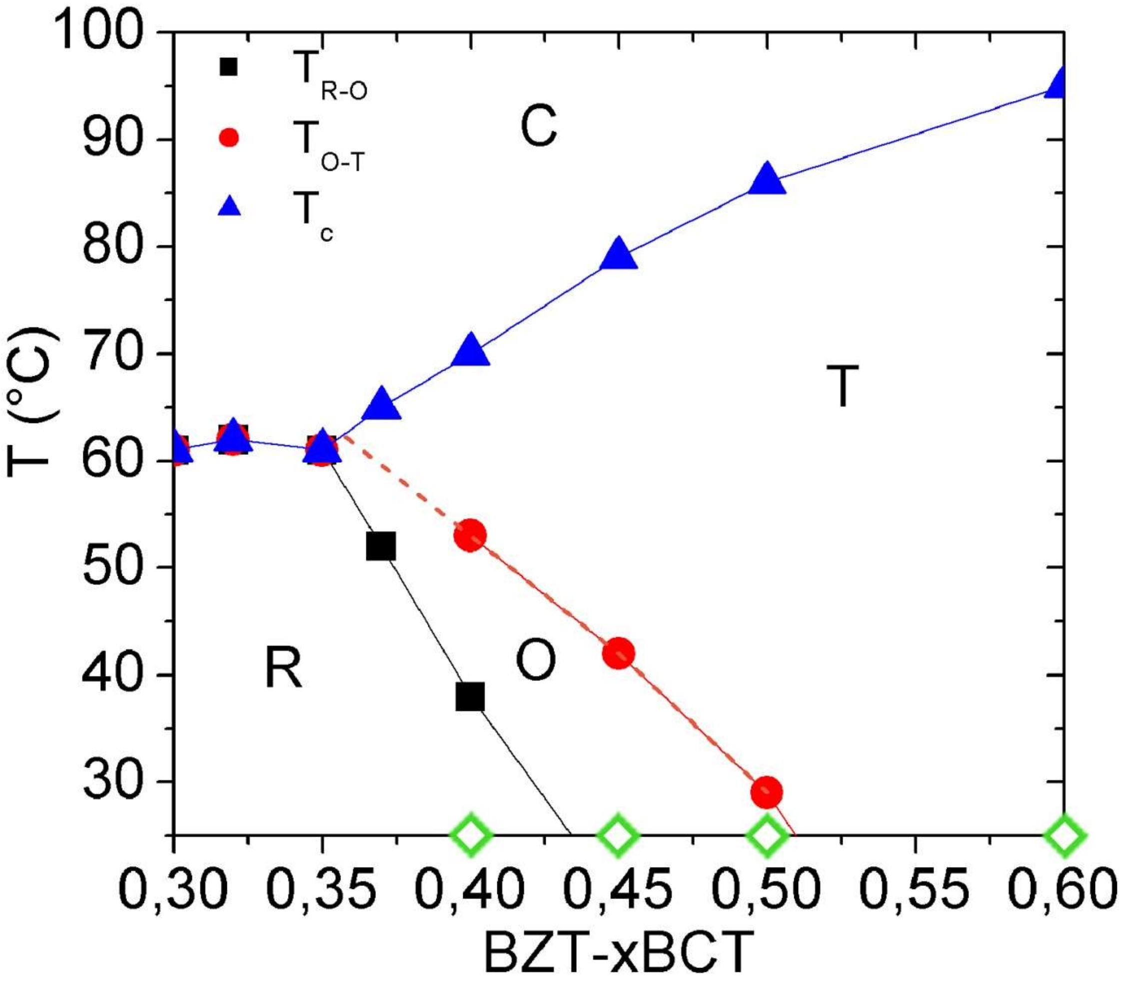

Figure 4.11: Phase diagram of the BZT – xBCT system, proposed by M. Acosta et al. [23]. As a function of temperature and composition either cubic (C), tetragonal (T), orthorhombic (O) or a rhombohedral (R) phase is present. Green squares denote compositions used for these studies.

In situ hot-stage experiments were conducted on BZT – xBCT with x = 0.4, 0.45 and 0.6 with heating and cooling rates of 5 – 10 °C/min. The temperature was stepwise increased from room temperature (RT) to 130 °C. *In situ* cold-stage investigations were performed on BZT – xBCT with x = 0.5 down to -30 °C.

For the BZT – 0.40BCT composition *in situ* hot-stage TEM investigations were performed using a grain imaged along the $[11\text{-}1]_c$ zone axis (Figure 4.12). At RT a multiple domain configuration consisting of rhombohedral domains with needle-shaped tips, lamellar domains and domains with curved walls were observed inside the grain (Figure 4.12 (a)). Moreover, a hierarchical domain structure is visible in all domains presented in Figure 4.12 (a). At 45 °C domain contrast was slightly reduced (Figure 4.12 (b)). According to the phase diagram this state corresponds to the orthorhombic symmetry (Figure 4.11). When the temperature was increased up to 65 °C most domain walls disappeared (Figure 4.12

(c)) and at 75 °C only a homogeneous contrast was observed (Figure 4.12 (d)). The ferroelectric phase transformed to the paraelectric phase at 75 °C, which is consistent with the Curie temperature of BZT – 0.40BCT [20, 23, 32]. On cooling the domain configuration reappeared at around 60 °C, reproducing the domain pattern from the initial state. The SAED patterns along the [11-1]$_c$ zone axis do not exhibit any significant changes during heat treatment (Figure 4.12 (a), (d), insets). This can be explained by very small rhombohedral distortions, calculated by R. Schierholz and presented in chapter 4.3.

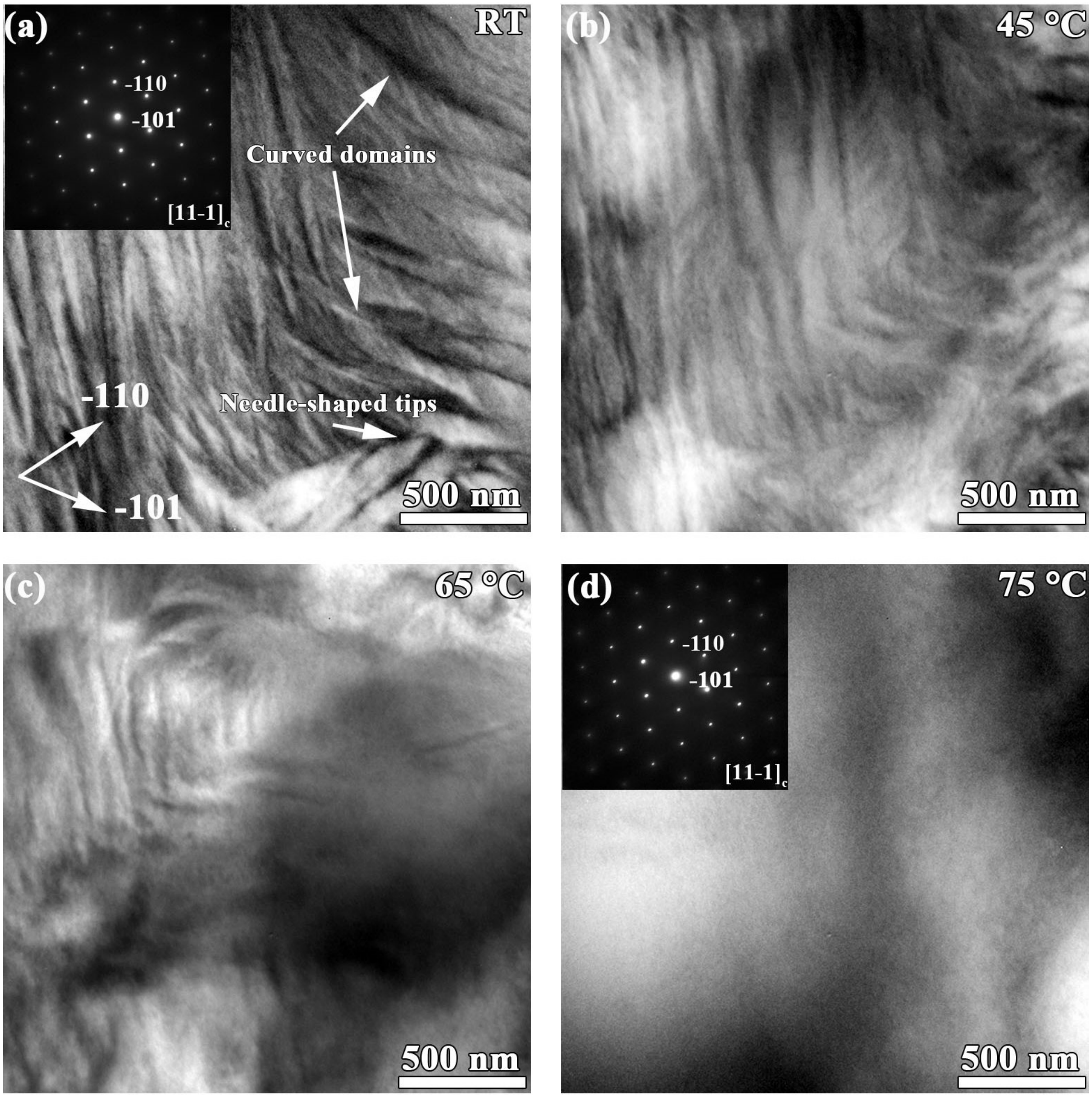

Figure 4.12 *In situ* TEM bright field images of the BZT – 0.4BCT along the [11-1]$_c$ zone axis at (a) RT, (b) 45 °C, (c) 65 °C, (d) 75 °C. In the insets of (a) and (d), the corresponding SAED patterns are depicted.

In situ hot-stage TEM experiments on the BZT – 0.45BCT ceramic were performed using a grain imaged along [112]$_c$ zone axis (Figure 4.13). Initially inclined wedge-shaped domains with tips pointing in a [1-10] direction are present inside the grain (Figure 4.13 (a)). With increasing temperature an orthorhombic to tetragonal phase transition occurs at 42 °C (Figure 4.11). However, the domain pattern does not exhibit significant changes even at 55 °C, as shown in Figure 4.13 (b). One of the reason, which can explain absence of any noticeable changes on the domain pattern can be related to the low temperature accuracy of the furnace holder. At 95 °C tips of the wedge-shaped domains become blunter (Figure 4.13 (c)). Such misoriented domain walls were previously reported for rhombohedral PZT [45].

When the temperature reached 130 °C domain contrast was dramatically reduced. However, few domains were still visible within the grain at that temperature (Figure 4.13 (d)). According to the literature, for BZT – 0.45BCT composition the phase transition to the paraelectric cubic state observes at around 80 °C [20, 23, 32] and, therefore, no domains should be visible. We assume that in this particular case TEM imaging was performed shortly after the temperature was achieved but not yet stabilized. This could significantly reduce the local temperature at the specimen and can explain the presence of ferroelectric domains. When the temperature was reduced down to 100 °C the domain contrast reappeared (Figure 4.13 (e)). Reappearance of the former domain configuration and nucleation of new curved domains as well as domain walls tracing in [11-1] direction on a previous wedge-shaped domain configuration were observed during cooling to RT (Figure 4.13 (e), (f)). The SAED patterns during heat treatment were also studied. No detectible changes or visible reflection splitting were observed. The inset of Figure 4.13 (d) displays a SAED pattern, recoded at 130 °C.

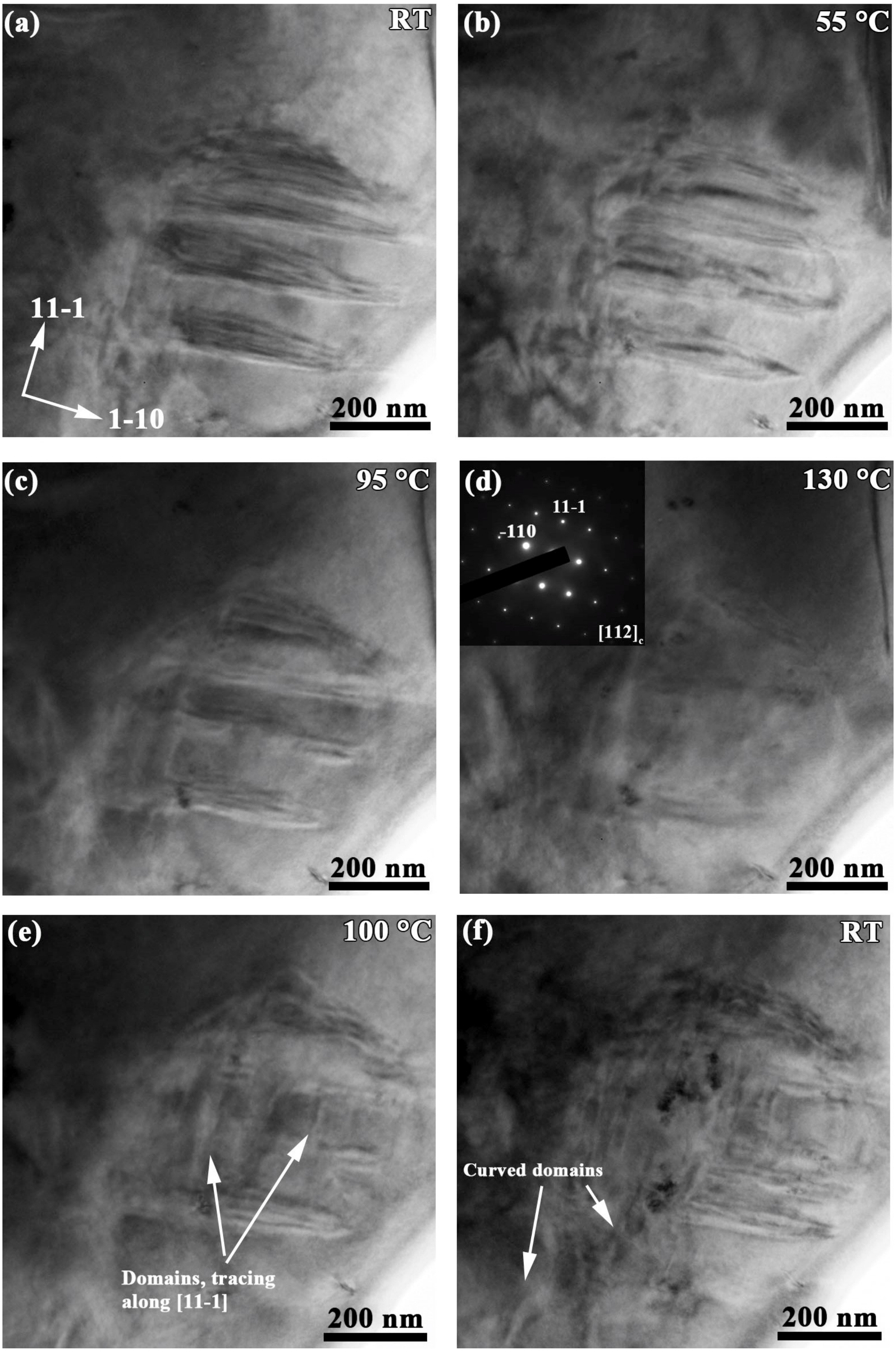

Figure 4.13: *In situ* TEM bright field images of the BZT – 0.45BCT along the [112]$_c$ zone axis during heating at (a) RT, (b) 55 °C, (c) 95 °C, (d) 130 °C and during cooling at (e) 100 °C, (b) RT. Depicted grain shows wedge-shaped domains with delta fringe contrast due to inclined domain walls. In the inset of (d), the corresponding SAED pattern is depicted.

Figure 4.14 displays BF images and corresponding SAED patterns of the BZT – 0.6BCT monitored along $[112]_c$ zone axis during *in situ* hot-stage TEM studies. At RT a BZT – 0.6BCT composition exhibit a ferroelectric tetragonal phase which undergoes a phase transition to the paraelectric phase at around 95 °C (Figure 4.11). Lamellar domains with walls tracing along [-110] direction were present prior to heating (Figure 4.14 (a)). At 45 °C only slight changes in the domain morphology, which were attributed to the bending of the specimen, were detected (Figure 4.14 (b)), but at 85 °C the domain contrast was reduced significantly (Figure 4.14 (c)) due to transition to the paraelectric state. At 92 °C only a "bubble" contrast is visible, which originated from the ion milling during sample preparation procedure. Clearly no domain walls were observed at that temperature (Figure 4.14 (d)), which coincides with the Curie temperature, reported for that composition [20, 23, 32]. The insets of Figure 4.14 show the corresponding SAED patterns taken along $[112]_c$ zone axis at RT, 45 °C, 85 °C and 92 °C, respectively. Neither reflection splitting nor any changes during heat treatment were observed. Upon further cooling lamellar domains started to reappear at around 75 °C (Figure 4.14 (e)). At RT a domain structure similar to the domain pattern, which was presented before heat treatment was observed (Figure 4.14 (e)), indicating that the domain configuration is completely reversible.

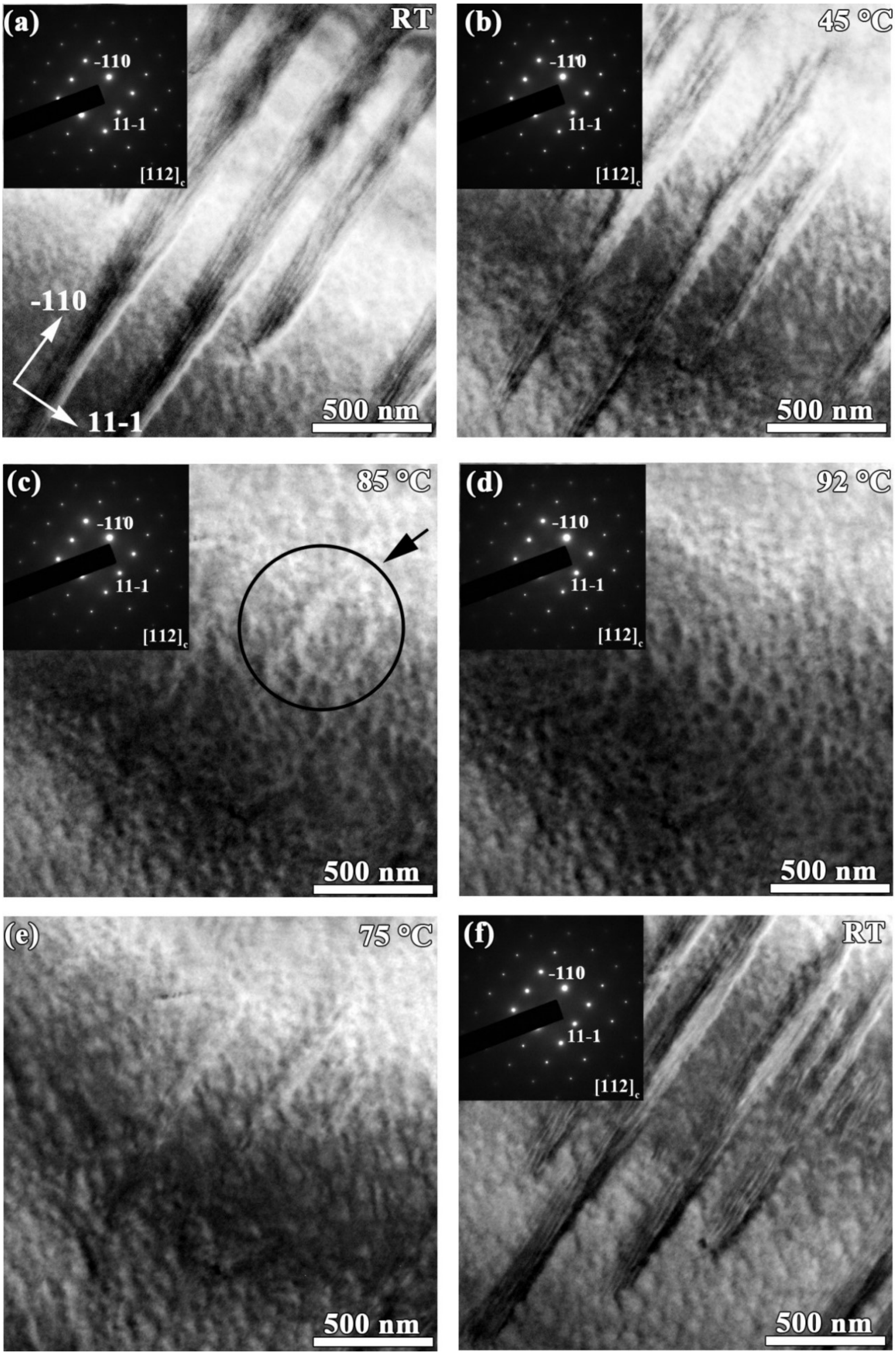

Figure 4.14: *In situ* TEM bright field images of the BZT – 0.6BCT along the $[112]_c$ zone axis at (a) RT, (b) 45 °C, (c) 85 °C, (d) 92 °C, (e) 75 °C, (f) RT (after heat treatment). A "bubble" contrast is visible due to ion milling. In the insets the corresponding SAED patterns are depicted.

According to Keeble et. al. [32] for BZT – 0.5BCT composition the phase transition from O to R is observed below RT. Therefore, in order to monitor the microstructural changes for BZT – 0.5BCT an *in situ* cold-stage experiment was performed.

The grain aligned along the $[11\text{-}1]_c$ zone axis was used to analyze a temperature induced phase transitions in BZT – 0.5BCT by *in situ* cold-stage TEM technique. At RT lamellar domains with the walls tracing along [11-2] direction, are observed within the grain (Figure 4.15 (a)). The inset of Figure 4.15 (a) shows the corresponding SAED pattern, which is devoid of any reflection splitting. On cooling, domain morphology significantly changed at -5 °C. Domains with curved walls and lamellar domains with their traces along [1-21] direction appeared within the grain, as marked on Figure 4.15 (b). Curved ferroelectric domains can indicate appearance of another phase or 180° domain walls [145, 146]. According to the BZT – xBCT phase diagram this temperature corresponds to the O → R phase transition area (Figure 4.15 (d)). Newly formed ferroelectric domains with walls tracing in [1-21] direction become more apparent with decrease of the temperature down to -30 °C (Figure 4.15 (c)), which corresponds to the rhombohedral symmetry (Figure 4.15 (d)).

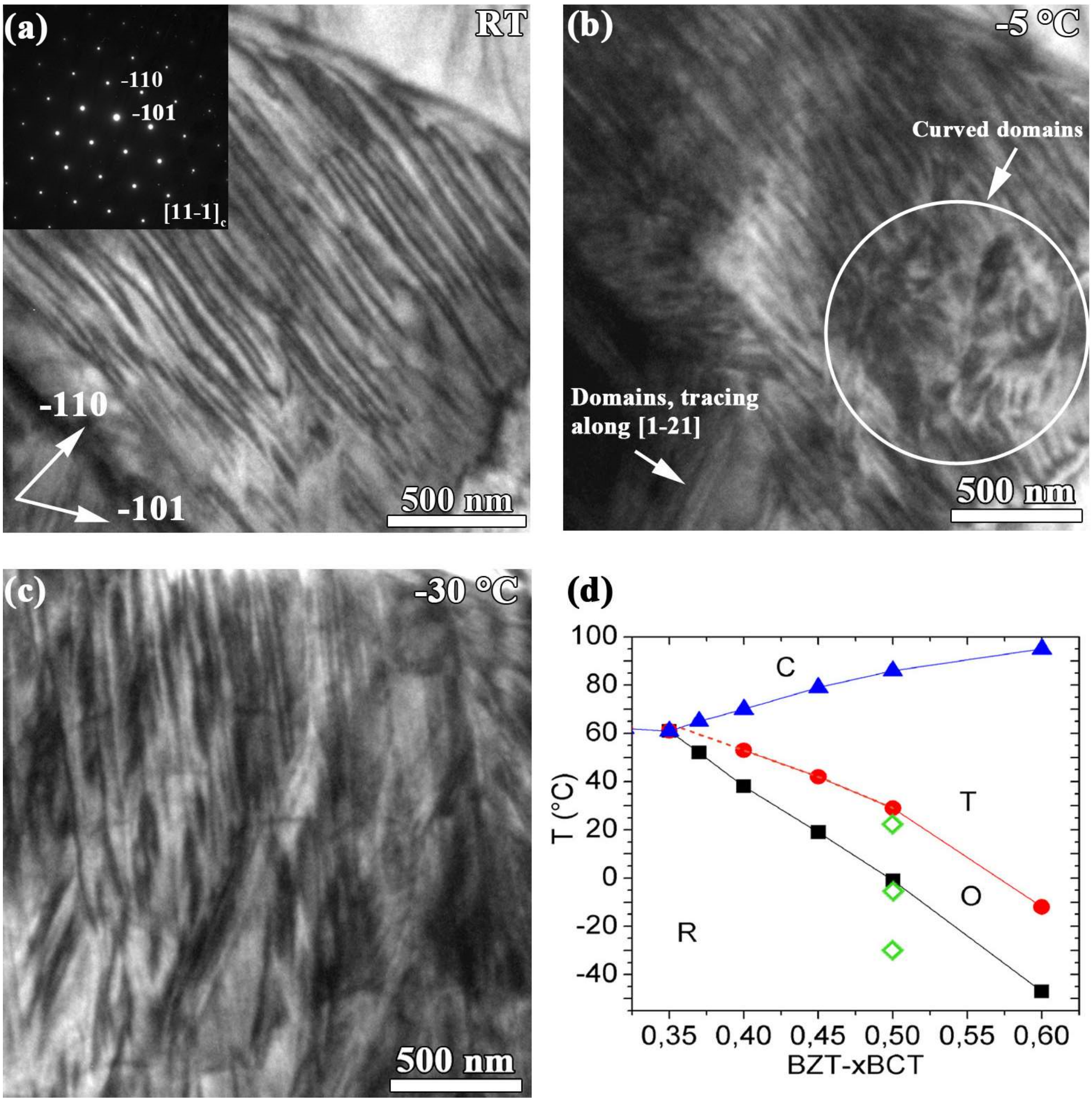

Figure 4.15: *In situ* TEM bright field images of the BZT – 0.5BCT along the [11-1]$_c$ zone axis at (a) RT, (b) -5 °C, (c) -30 °C, (d) phase diagram of the BZT – xBCT [23]. Green squares correspond to the temperatures during cooling. In the inset of (a), the corresponding SAED pattern is depicted.

During heat treatment (followed after cooling) significant changes in domain configuration were observed. At 5 °C the major part of the studied grain was occupied by domains, which do not follow any particular direction (Figure 4.16 (a)). On further heating the volume fraction of misoriented domains decreased, while lamellar domains tracing in [11-2] direction became more evident (Figure 4.16 (b), (c)). When the Curie temperature for this composition was exceeded the domain contrast completely disappeared and a paraelectric cubic phase became stable (Figure 4.16 (d)).

When the temperature was reduced down to 87 °C the domain walls reappeared due to paraelectric to ferroelectric phase transition (Figure 4.16 (e)). After cooling down to RT domain morphology is different from that in the initial state. The probed grain contained domain walls with traces along [11-2] direction. After heating the domain configuration was miniaturized (Figure 4.16 (f)). Domains with curved walls and lamellar domains along [1-21] direction were also observed at RT (Figure 4.16 (f)). Recently, by means of convergent beam electron diffraction (CBED), a thermally induced irreversible domain transformation from wedge-shaped rhombohedral to a lamellar tetragonal domain configuration was reported for BZT – 0.5BCT [139].

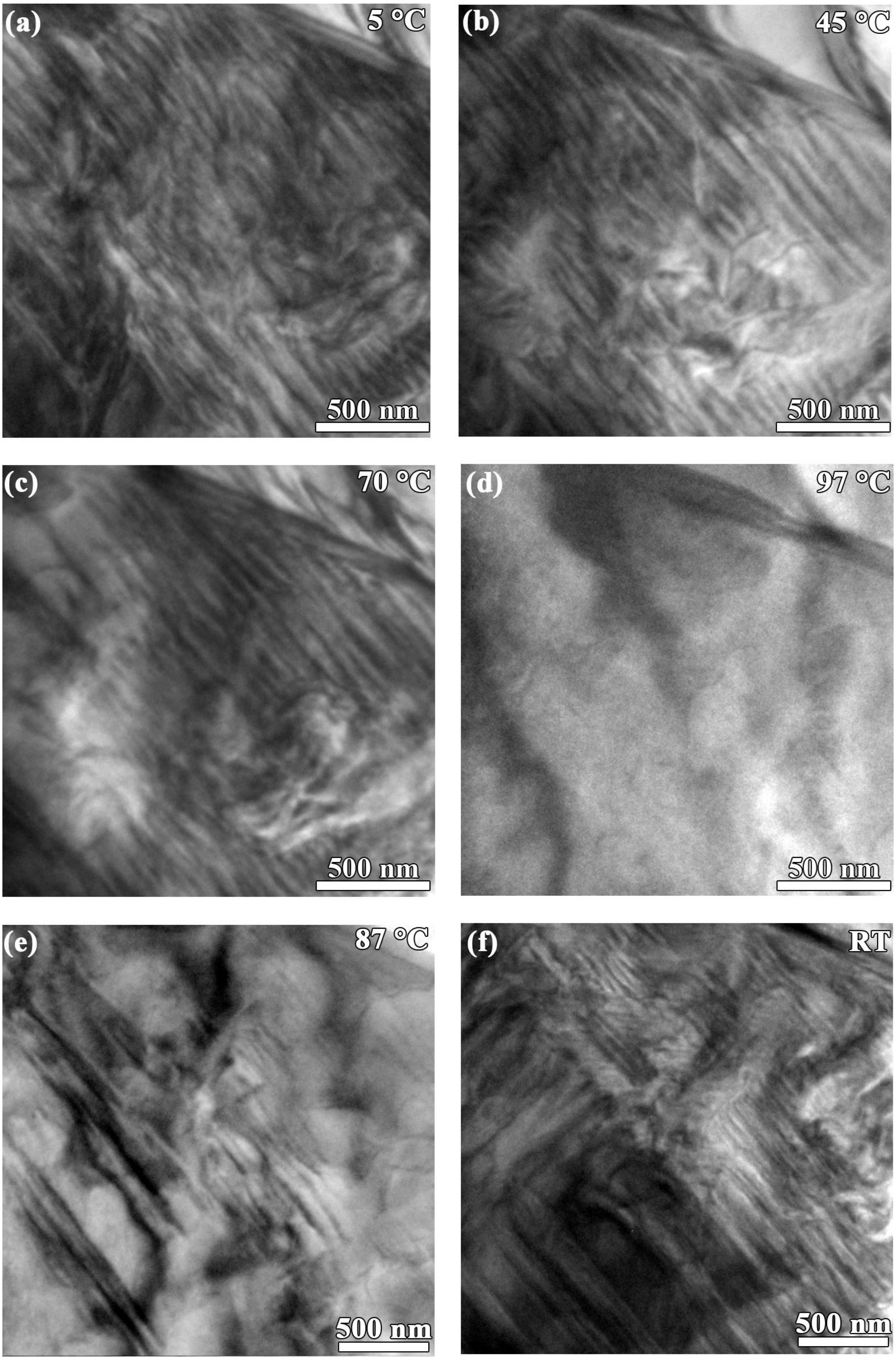

Figure 4.16: *In situ* TEM bright field images of the BZT – 0.5BCT along the [11-1]$_c$ zone axis during heating at (a) 5 °C, (b) 45 °C, (c) 70 °C, (d) 97 °C and during cooling at (e) 87 °C, (f) RT. Microstructural changes as a function of temperature are observed.

In general, during *in situ* hot- and cold-stage TEM experiments changes in the domain morphology were observed in BZT – xBCT piezoceramic. For all studied compositions multiple ferroelectric domains were observed within the grains at RT. Domains with curved walls, which do not follow any particular direction, were present in BZT – 0.4BCT at RT and appeared in BZT – 0.45BCT at 55 °C and in BZT – 0.5BCT at -5 °C, which corresponds to the PPT area (Figure 4.11). In addition, curved domains were not observed for the BZT – 0.6BCT composition, which locates deep in the T region of the phase diagram (Figure 4.11). Therefore, in BZT – xBCT curved domains evolve in compositions near the PPT area. Upon heating domain walls in BZT – xBCT reversibly vanished due to the ferroelectric to paraelectric phase transition at temperatures, which are in a good agreement with the Curie temperature, previously reported for this material [20, 23, 32]. The SAED patterns did not reveal any reflection splitting or any detectable changes during heat treatment for all studied materials. However, due to very small deviations for R, O, and T phases in BZT – xBCT system, described in the chapter 4.3, the information obtained by SAED technique is limited and cannot be used for accurate structure determination in this case.

4.6 In situ electric field TEM investigations

In the following chapter the composition dependent microstructural evolution of the BZT – xBCT system as a function of electric field will be reported. A wide compositional range of the BZT – xBCT system (with x = 0.3, 0.32, 0.4, 0.45, 0.48, 0.52, 0.6) was investigated *in situ* under an applied electric field using TEM.

In Figure 4.17 a grain orientated along $[1\text{-}53]_c$ zone axis of BZT – 0.30BCT during poling process is presented [123]. At the unpoled state (Figure 4.17 (a)) lamellar domains with an average size of 174 ± 35 nm are visible inside the grain. The domain walls with a normal vector, tracing along [30-1] direction, are expected to be (10-1) type walls tilted about 13.8° with respect to the viewing direction. This corresponds to the presence of 109° domains reported for rhombohedral PZT [45]. The inset of Figure 4.17 (a) illustrates the SAED pattern, recorded prior to applying a poling field. Due to small rhombohedral distortions a reflection splitting in the SAED pattern was not resolved. When the poling field achieved the value of 5 kV/cm the domain walls disappeared and single-domain state formation occurred (Figure 4.17 (b)).

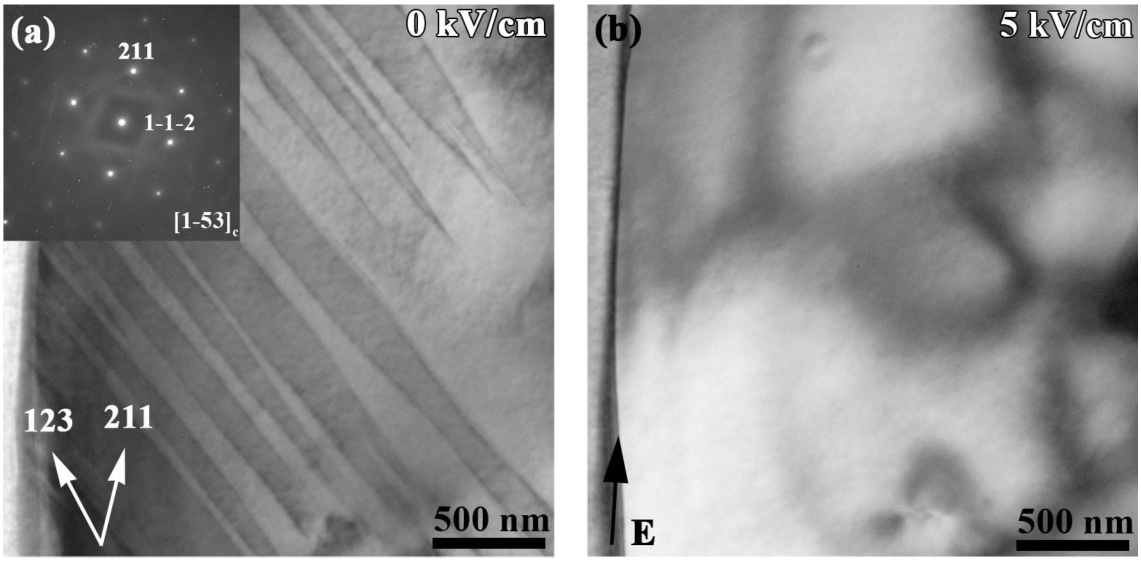

Figure 4.17: *In situ* TEM bright field images of the BZT – 0.3BCT along the [1-53]c zone axis at (a) virgin state, (b) 5 kV/cm. The direction of the poling field is indicated by the dark arrow in (b). In the inset of (a), the corresponding SAED pattern is depicted [123].

Another representative grain of BZT – 0.30BCT, imaged along [-1-14] zone axis, is depicted in Figure 4.18 [123]. Prior to applying an external electric field edge-on 109° domains with walls in (1-10) planes and domain walls with the normal vector tracing along <311> direction, which lie along {110} planes are visible inside the grain (Figure 4.18 (a)). Increasing the poling field to 4.2 kV/cm, domain contrast changed, indicating a field induced domain switching (Figure 4.18 (b)). Multiple domains disappeared and transition to a single-domain state occurred at the nominal field of 5 kV/cm. (Figure 4.18 (c)). The multi- to single-domain state transition is found to be reversible as multiple domain contrast reappeared within the grain upon field removal (Figure 4.18 (d)). The SAED pattern recorded at 5 kV/cm is shown in the inset of Figure 4.18 (c). Due to the resolution limit, no visible changes were observed during poling process on the SAED patterns. The same region was monitored by CCD during the second cycle. The corresponding multimedia file (Movie 1) and its description are presented in the Appendix.

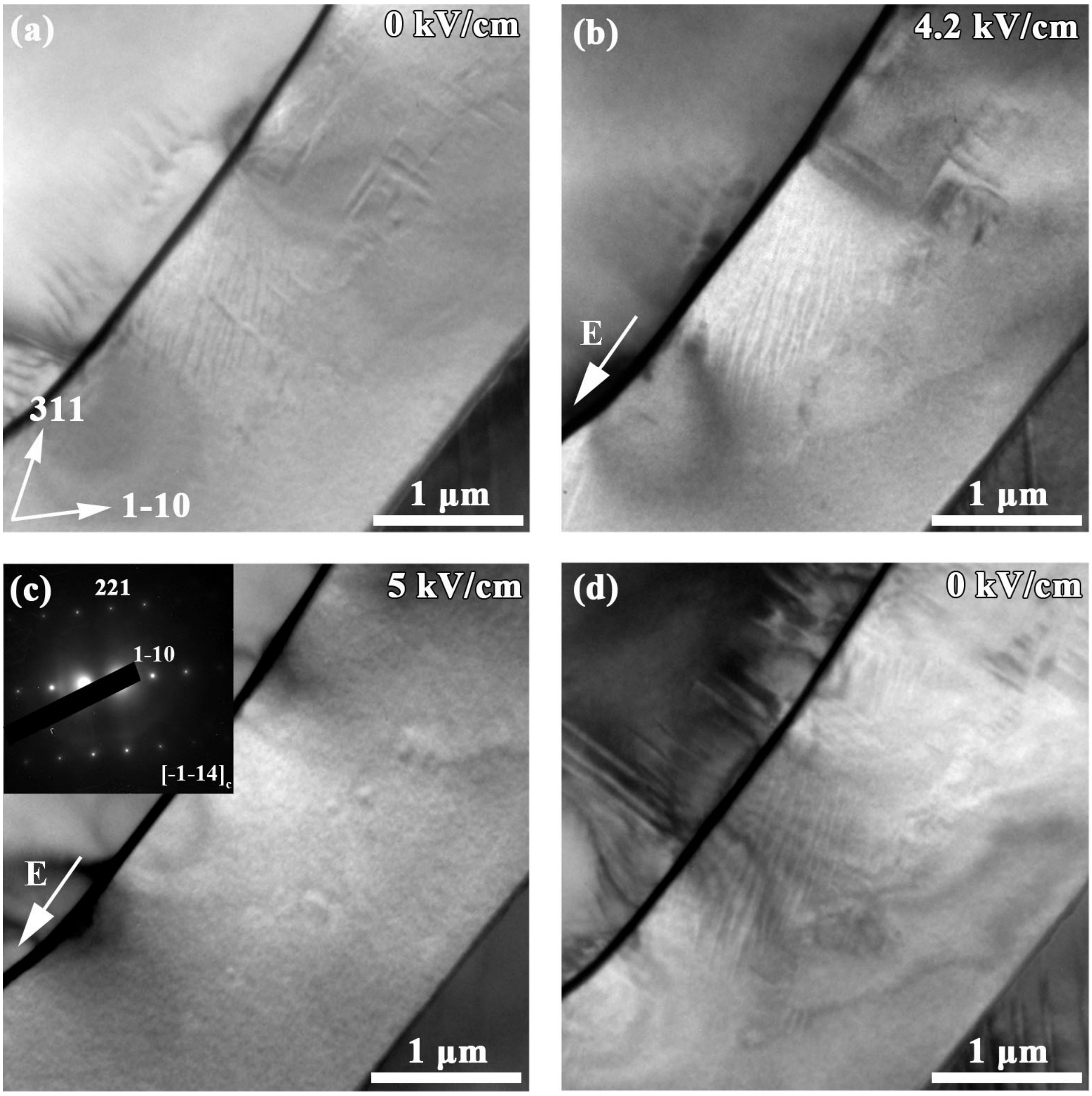

Figure 4.18: *In situ* TEM bright field images of BZT – 0.3BCT along the $[-1-14]_c$ zone axis at (a) virgin state, (b) 4.2 kV/cm, (c) 5 kV/cm, (d) zero field after two cycles. The direction of the poling field is indicated by the bright arrow in (b), (c). In the inset of (c), the corresponding SAED pattern is depicted [123].

A grain orientated along $[1-53]_c$ zone axis of BZT – 0.3BCT ceramic was also used to analyze the domain morphology evolution during electrical poling (Figure 4.19) [123]. In the virgin state two sets of ferroelectric domains with an average size of 298 ± 42 nm were observed within the grain (Figure 4.19 (a)). At the nominal poling field of 2.66 kV/cm the domain contrast disappeared completely and a single-domain state was formed throughout the grain (Figure 4.19 (b)). The SAED patterns recorded at multiple and at single-domain states during the initial poling do not show any perceptible changes or splitting of the Bragg spots (Figure 4.19 (a), (b) insets).

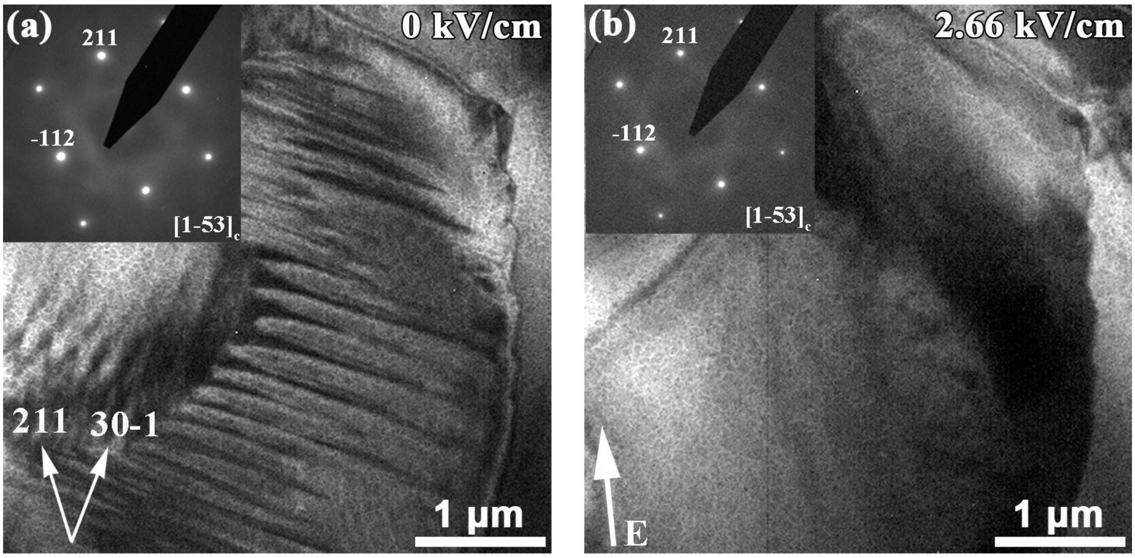

Figure 4.19: *In situ* TEM bright field images of the BZT – 0.3BCT along the [1-53]c zone axis at (a) virgin state, (b) 2.66 kV/cm. The direction of the poling field is indicated by the bright arrow in (b). In the insets, the corresponding SAED patterns are depicted [140].

As shown in Figure 4.20 (a) a multiple domain configuration reappeared upon field removal. At the second cycle a nanodomain state was formed when the applied field reached a nominal value of 0.66 kV/cm (Figure 4.20 (b)). At the field strength of 1.33 kV/cm the domain configuration completely disappeared. A single-domain state was formed within the grain (Figure 4.20 (c)). Thus, a reversible transformation from multi- to single-domain state occurred with appearance of an intermediate nanodomain state. At zero field the domain pattern significantly changed in comparison to the virgin state, miniaturized domains were observed within microsized domain lamellas (Figure 4.20 (d)). After the second cycle a multiple domain state with a remanent polarization was present. When the nominal poling field of -2.66 kV/cm with reversed polarity was applied, the single-domain state appeared again (Figure 4.20 (e)). However, higher fields induced a further transformation to the multiple domain state. At the field strength of -14 kV/cm new sets of domains started to appear from the grain boundary. These new formed domains grew with further increase in the poling fields up to -20 kV/cm (Figure 4.20 (f)). Therefore, with increasing electric field we observed multi-domain state (A) → nanodomain state → single-domain state → multi-domain state (B) transformation. The SAED patterns of BZT – 0.3BCT were also monitored during electrical poling. Neither detectable changes nor reflections splitting in the SAED patterns were observed, which is expected considering very small distortions from a cubic symmetry for BZT – 0.3BCT.

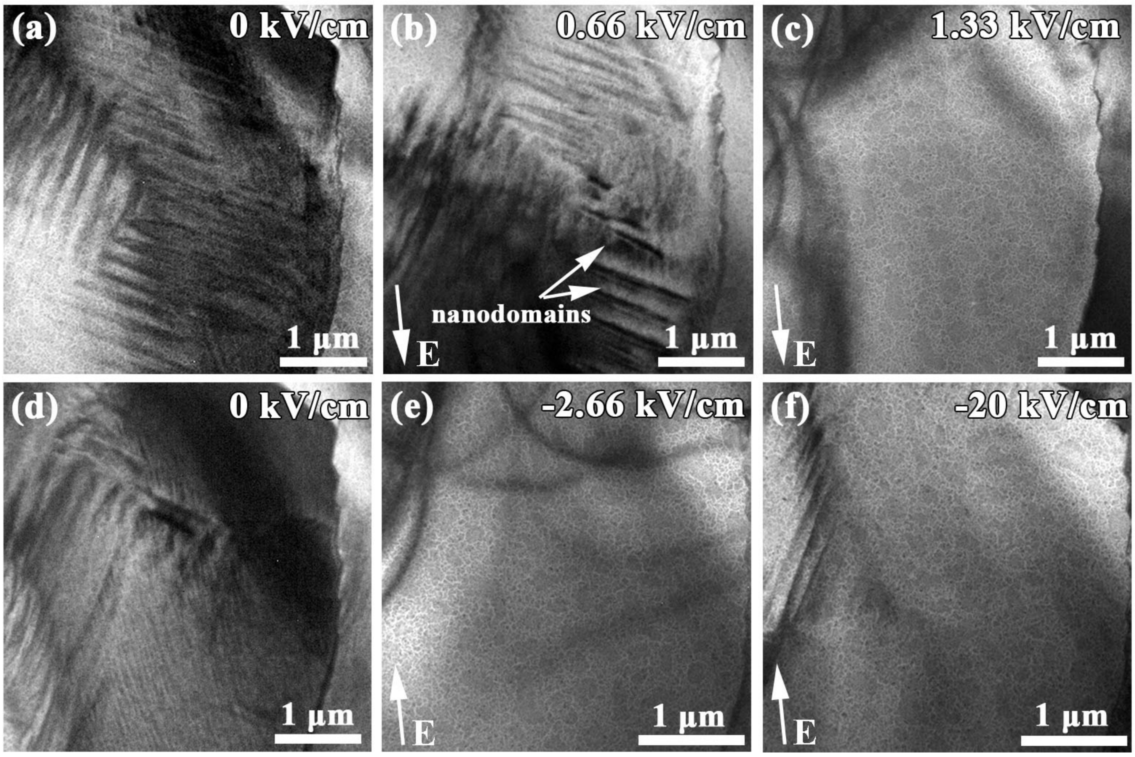

Figure 4.20: *In situ* TEM bright field images of the BZT – 0.3BCT along the $[1\text{-}53]_c$ zone axis at (a) zero field, (b) 0.66 kV/cm, (c) 1,33 kV/cm, (d) zero field, (e) -2.66 kV/cm, (f) -20 kV/cm. The direction of the poling field is indicated by the bright arrows [140].

It was noticed that a single-domain state appeared at different poling fields for the same composition, even with the same grain orientation (Figure 4.17 (b), Figure 4.19 (b)). This is related to the fact that the electric field is not equal in different grains due to a presence of circular perforation in the center of the TEM specimens, which can enhance or diminish the actual field value [131]. Additionally, it is also related to the stress arising from the neighboring grains in a polycrystalline material. In the present work nominal values of the poling fields, calculated as the applied voltage divided by the distance between electrodes, were used for all studies.

The domain morphology evolution in BZT – 0.32BCT under poling conditions was examined using a grain orientated along $[1\text{-}10]_c$ zone axis (Figure 4.21). In the virgin state, edge-on (110) domains with an average size of 144 ± 30 nm were observed within the grain (Figure 4.21 (a)). An increase in the poling field strength leads to the vanishing of the domain walls from the regions close to the grain boundary (Figure 4.21 (a) – (d)). A single-domain state formed at approximately 3.2 kV/cm (Figure 4.21 (d)). When the electric field reached a nominal value of 4.2 kV/cm a nucleation of nanosized domains occurred (Figure 4.21 (e)). New sets of miniaturized domains were formed under further increase in poling field (Figure 4.21 (f)). In Figure 4.21 (g) – (i) SAED patterns of the virgin state, at 2 kV/cm and at

5 kV/cm are represented, respectively. As before, the SAED patterns do not exhibit any significant changes during the poling process.

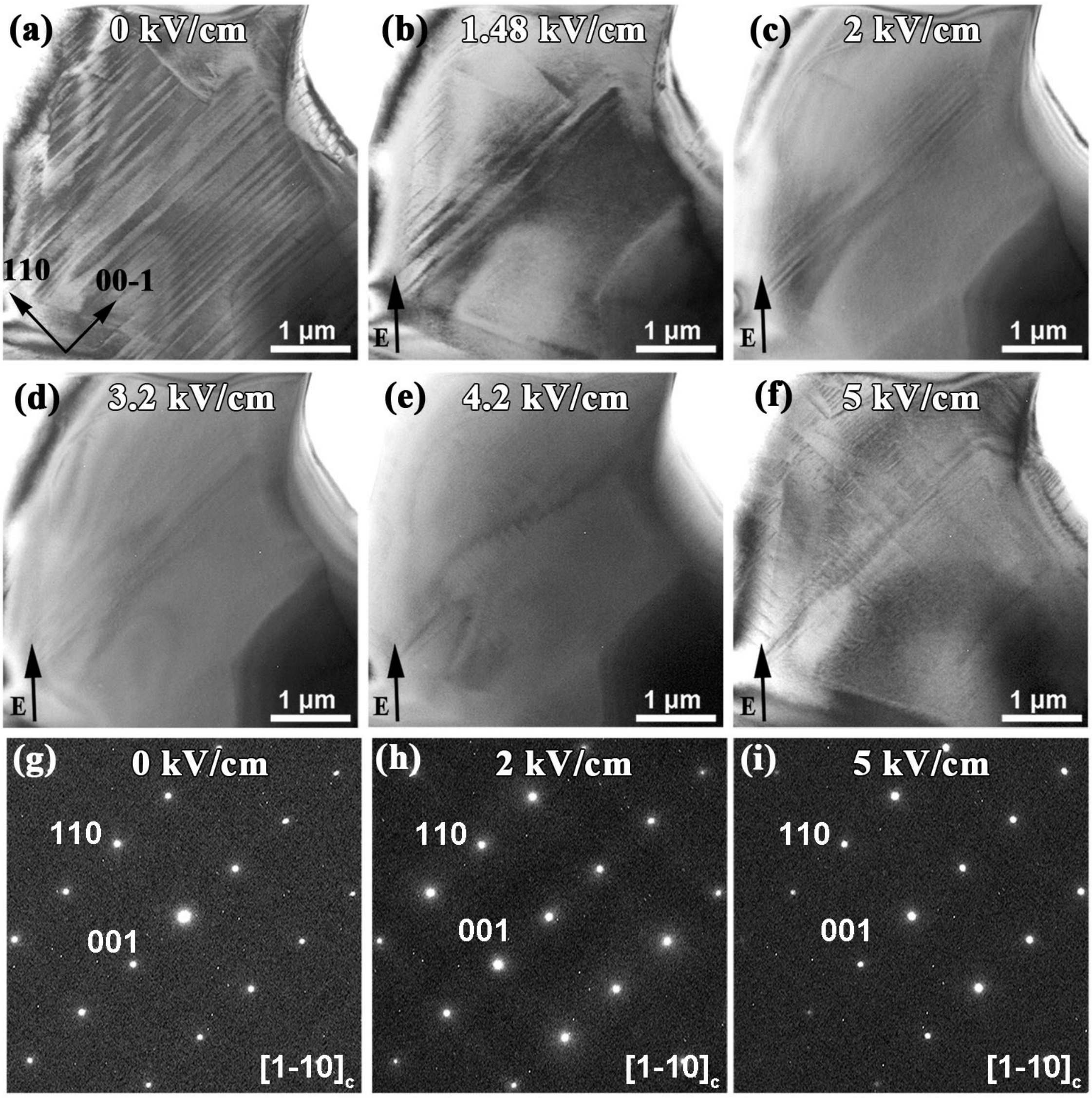

Figure 4.21: *In situ* TEM bright field images of the BZT – 0.32BCT along the $[1\text{-}10]_c$ zone axis at (a) virgin state, (b) 1.48 kV/cm, (c) 2 kV/cm, (d) 3.2 kV/cm, (e) 4.2 kV/cm, (f) 5 kV/cm. The direction of the poling field is indicated by the dark arrows. Corresponding SAED patterns recorded at (g) virgin state, (h) 2 kV/cm, (c) 5 kV/cm [140].

TEM micrographs in Figure 4.22 display the microstructural changes of BZT – 0.4BCT under an applied electric field. Very thin 71° domains with walls along (100) crystallographic planes are visible inside the grain imaged along its $[0\text{-}10]_c$ zone axis at the virgin state (Figure 4.22 (a)). These domains have an average size of 50 – 100 nm. A field induced transformation from the multiple domain state to the single-domain state, which is found to be reversible, occurred at approximately 1.5 kV/cm (Figure

4.22 (b)). Because the resolution is not sufficient, corresponding SAED patterns are devoid of reflection splitting (Figure 4.22 (a), (b)).

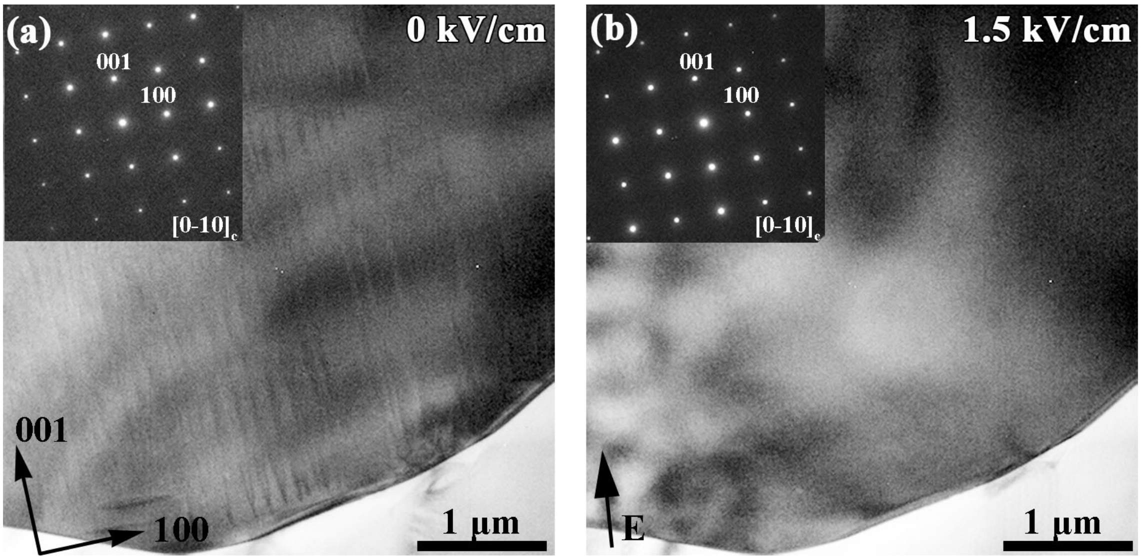

Figure 4.22: *In situ* TEM bright field images of the BZT – 0.40BCT along the [0-10]$_c$ zone axis at (a) virgin state, (b) 1.5 kV/cm. The direction of the poling field is indicated by the dark arrow in (b). In the insets, the corresponding SAED patterns are depicted [140].

Additionally, the CBED technique was used in order to analyze the symmetry of the same grain. The TEM bright field images at zero field and at a field strength of 2 kV/cm are depicted in Figure 4.23 (a), (b), respectively. A transformation from multi- to single-domain state during the re-poling process occurred at the nominal poling field of 1 kV/cm and was still present at 2 kV/cm (Figure 4.23 (b)). Figure 4.23 (c), (d) represents the corresponding CBED patterns along [0-10]$_c$ zone axis, recorded prior to re-poling and at 2 kV/cm from the area marked with an arrow. It can be seen that both CBED patterns have (10-1) a mirror plane, which corresponds to the rhombohedral or orthorhombic symmetry. Therefore, no transition from the rhombohedral to the tetragonal phases occurred during poling process. However, the phase transition from the rhombohedral to the orthorhombic phase on poling cannot be excluded.

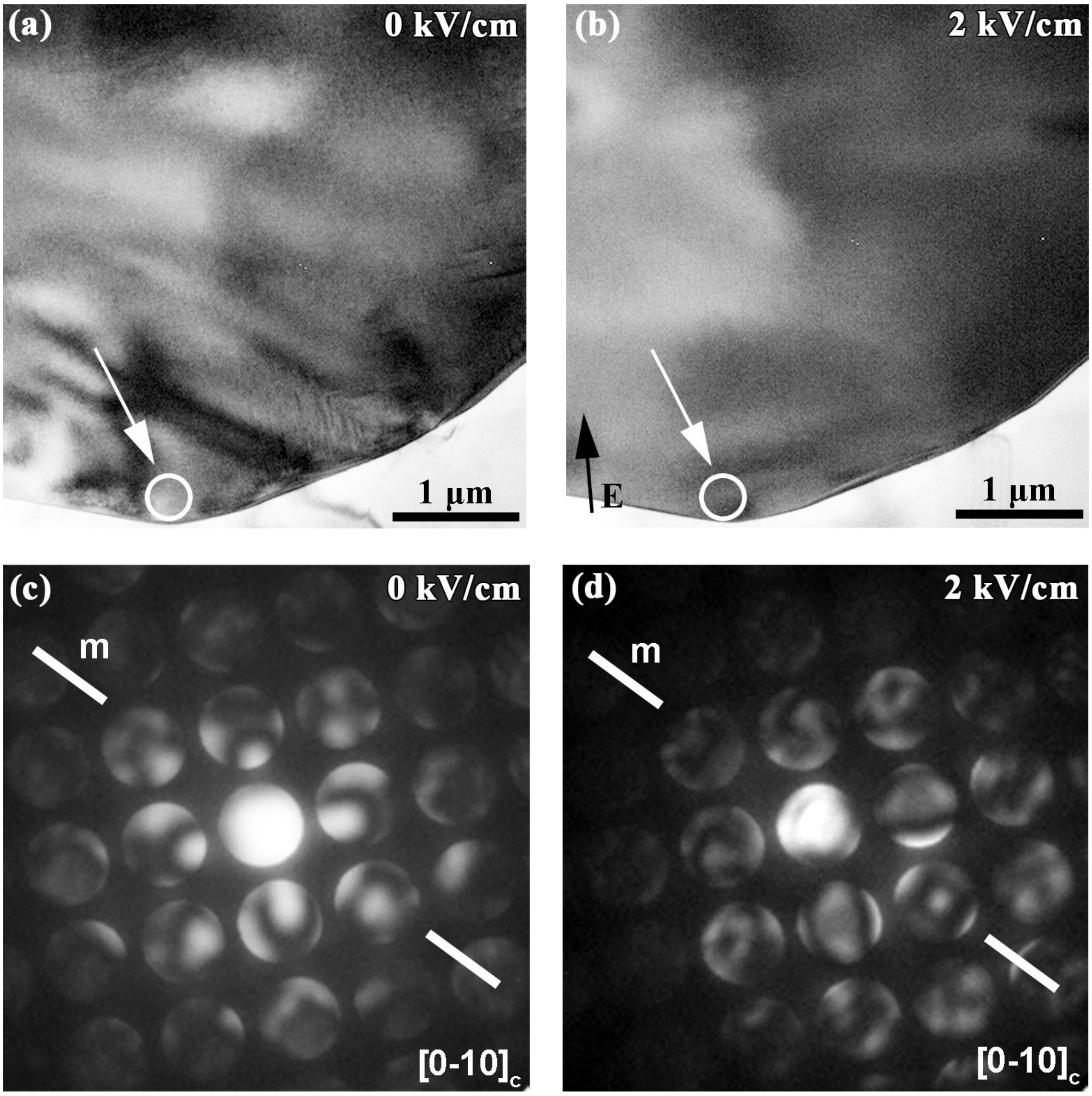

Figure 4.23: *In situ* TEM bright field images of the BZT – 0.40BCT along the [0-10]$_c$ zone axis at (a) zero field, (b) 2 kV/cm. The direction of the poling field is indicated by the dark arrow in (b). Corresponding CBED patterns recorded at (c) zero field, (d) 2 kV/cm show the presence of (10-1) mirror plane.

In situ TEM observation of the domain evolution in the BZT – 0.45BCT composition is shown in Figure 4.24. Initially, the grain imaged along its [1-10]$_c$ zone axis contained lamellar ferroelectric domains with an average width of 145 ± 36 nm, tracing along <111> direction. Within these domain lamellas areas with nanodomain structure were observed (Figure 4.24 (a)). The density of nanodomains increased with increase in the external field strength (Figure 4.24 (b), (c)). When the nominal value of electric field achieved 2.66 kV/cm a whole grain became a large single domain (Figure 4.24 (d)). Insets in the Figure 4.24 (a), (d) show corresponding SAED patterns. As well as in all previous cases, the SAED patterns are devoid of reflection splitting and no detectable changes were visible during electrical poling.

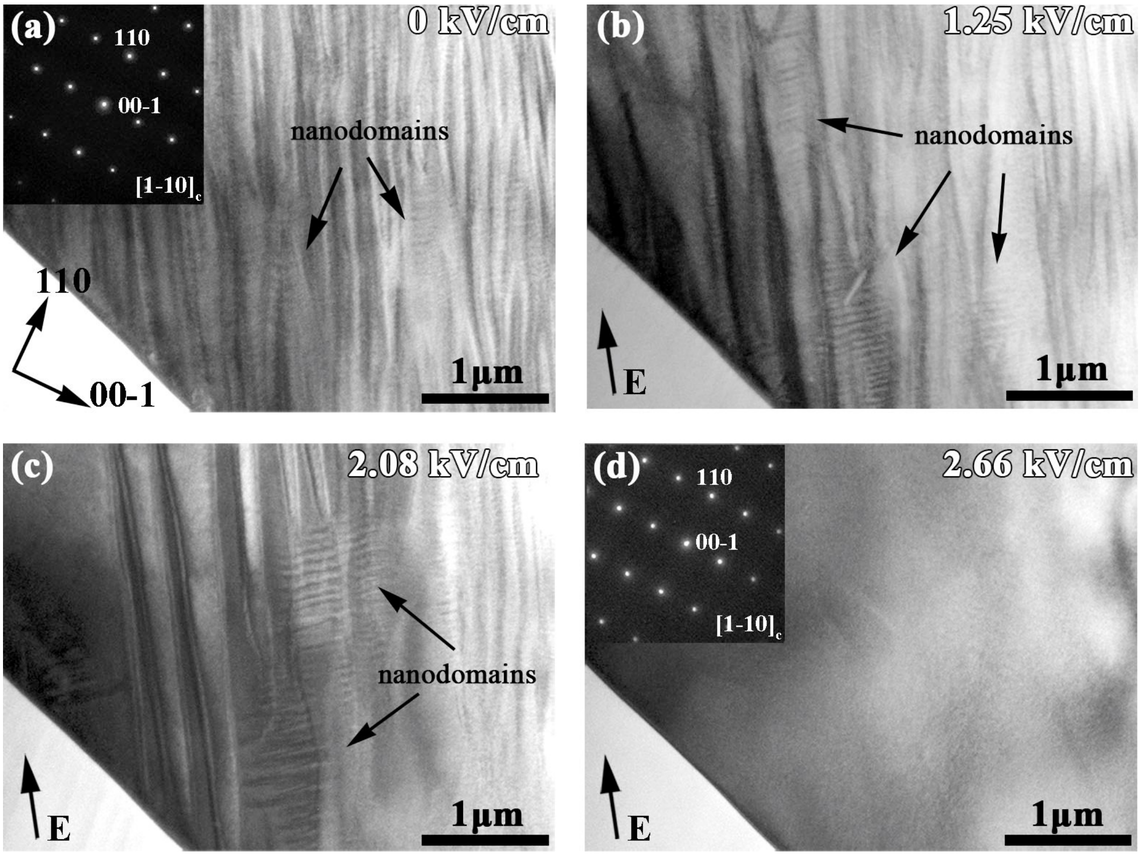

Figure 4.24: *In situ* TEM bright field images of the BZT – 0.45BCT along the [1-10]$_c$ zone axis at (a) zero field, (b) 1.25 kV/cm, (c) 2.08 kV/cm, (d) 2.66 kV/cm. The direction of the poling field is indicated by dark arrows. In the insets of (a) and (d), the corresponding SAED patterns are depicted [140].

In Figure 4.25 TEM micrographs of BZT – 0.48BCT as a function of the poling process are depicted. At the unpoled state a multiple domain structure, which is different from that previously observed in BZT – xBCT, was visible inside the grain (Figure 4.25 (a)). Domain pattern with such “wavy” domain contrast can be related to the fact that this composition is located at the PPT area. A small increase in poling field strength to 0.5 kV/cm did not provide any noticeable changes in the domain morphology (Figure 4.25 (b)). However, already at the nominal poling field of 1 kV/cm a multiple domain state → single-domain state transformation occurred (Figure 4.25 (c)). This transformation is reversible as domain walls reappeared upon field removal, forming a hierarchical domain structure at zero field (Figure 4.25 (d)). Nevertheless, this domain pattern is different from the virgin state, which is associated with the presence of a remanent polarization after first cycle.

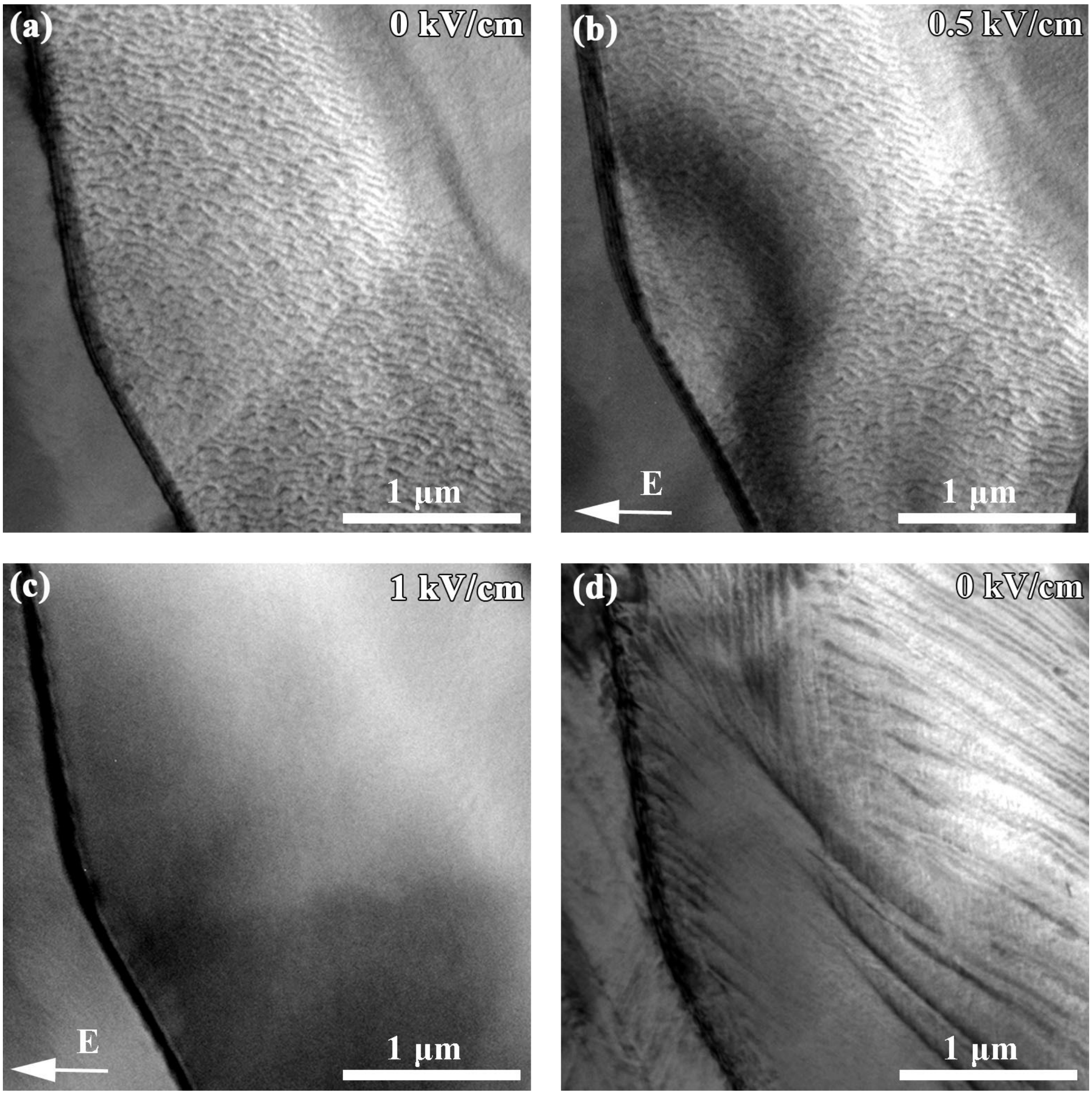

Figure 4.25: *In situ* TEM bright field images of the BZT – 0.48BCT at (a) virgin state, (b) 0.5 kV/cm, (c) 1 kV/cm, (d) zero field. The direction of the poling field is indicated by bright arrows.

The domain evolution in BZT – 0.52BCT piezoceramic during electrical poling was monitored using the grain imaged along its $[-110]_c$ zone axis (Figure 4.26). In the unpoled state a domain structure with an average domain width of 128 ± 12 nm was observed (Figure 4.26 (a)). At the field strength of 1.66 kV/cm all domain walls disappeared forming a single-domain state throughout the grain (Figure 4.26 (b)). However, this single domain state was not stable. It transformed to the multi-domain state with further increase in poling field (Figure 4.26 (c), (d)). A lamellar domain structure formed inside the grain when the poling field reached the value of 5.8 kV/cm (Figure 4.26 (c)). At the poling field of 7.5 kV/cm domain width increased and only lamellar domains with walls tracing long <111> directions were present inside the grain (Figure 4.26 (d)). Changes in the corresponding SAED patterns during the poling process have not been noticed because of small distortions, which result in a very small peak splitting that cannot be resolved in the SAED patterns (Figure 4.26, insets).

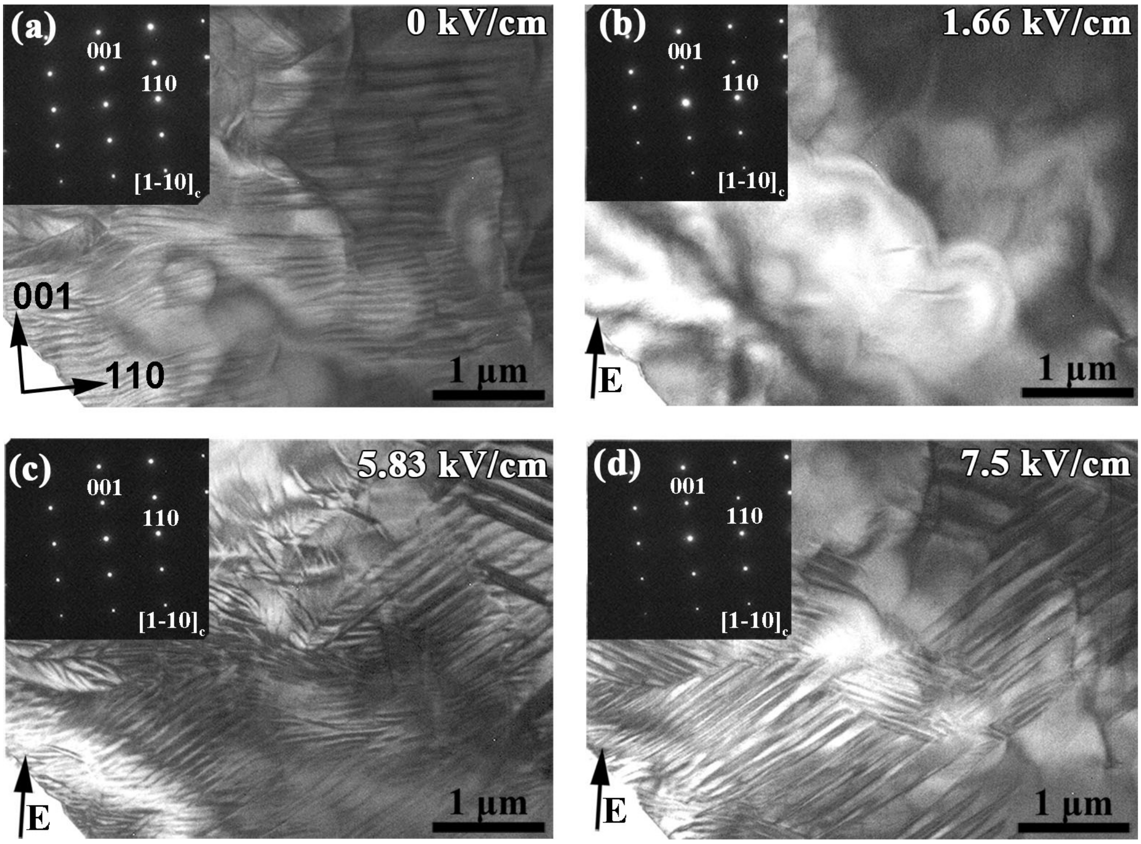

Figure 4.26: *In situ* TEM bright field images of the BZT – 0.52BCT along the $[1\text{-}10]_c$ zone axis at (a) virgin state, (b) 1.66 kV/cm, (c) 5.83 kV/cm, (d) 7.5 kV/cm. The direction of the poling field is indicated by dark arrows. In the insets, the corresponding SAED patterns are depicted. [140].

It should be noted that upon field removal a single-domain state was not observed within this grain. At zero field a multiple domain structure with domain walls, which do not correspond to certain crystallographic planes, was formed (Figure 4.27 (a)). During poling reversal, a single-domain state was achieved at the poling field value of about –6.5 kV/cm (Figure 4.27 (c)). However, this single-domain state transformed to a multi-domain state within few seconds at the same field strength.

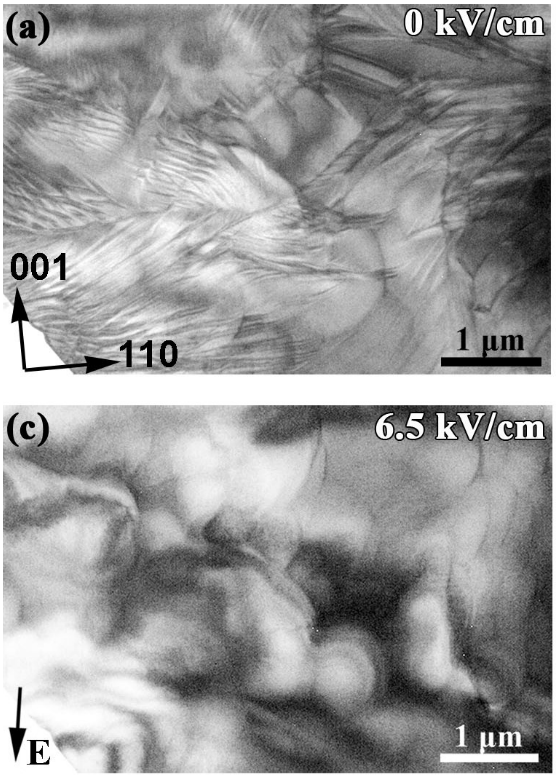

Figure 4.27: *In situ* TEM bright field images of the BZT – 0.52BCT along the [1-10]$_c$ zone axis at (a) zero field, (b) -5.83 kV/cm, (c) -6.5 kV/cm, (d) -6.5 kV/cm after 10 seconds. The direction of the poling field is indicated by dark arrows [140].

The domain morphology evolution during electrical poling in the BZT – 0.60BCT was studied using the grain imaged along the [112]$_c$ zone axis (Figure 4.28). Initially, domain lamellas with traces along [1-10] direction were observed (Figure 4.28 (a). The domain size at the unpoled state was determined to be 173 ± 41 nm. No visible changes in the domain morphology were detected up to the nominal poling field of 7.66 kV/cm. At 8.66 kV/cm a field induced domain switching occurred. Nanodomains were formed across the grain (Figure 4.28 (b)). The multi-domain state was present even at very high poling field of 12 kV/cm. A remanent state after poling showed nanometer-sized ferroelectric domains (Figure 4.28 (c)). When the electric field was reversed in polarity slight changes in the domain morphology were observed during repoling process, but the multiple domain state was still observed at high external field of –8.66 kV/cm (Figure 4.28 (d)). It should be noted that the transformation to a single-domain state for tetragonal BZT – 0.6BCT occurred at a rather high poling field value of –20 kV/cm. Corresponding SAED patterns for BZT – 0.6BCT did not reveal any apparent changes during poling process as for all other compositions (Figure 4.28 (b), (c) insets).

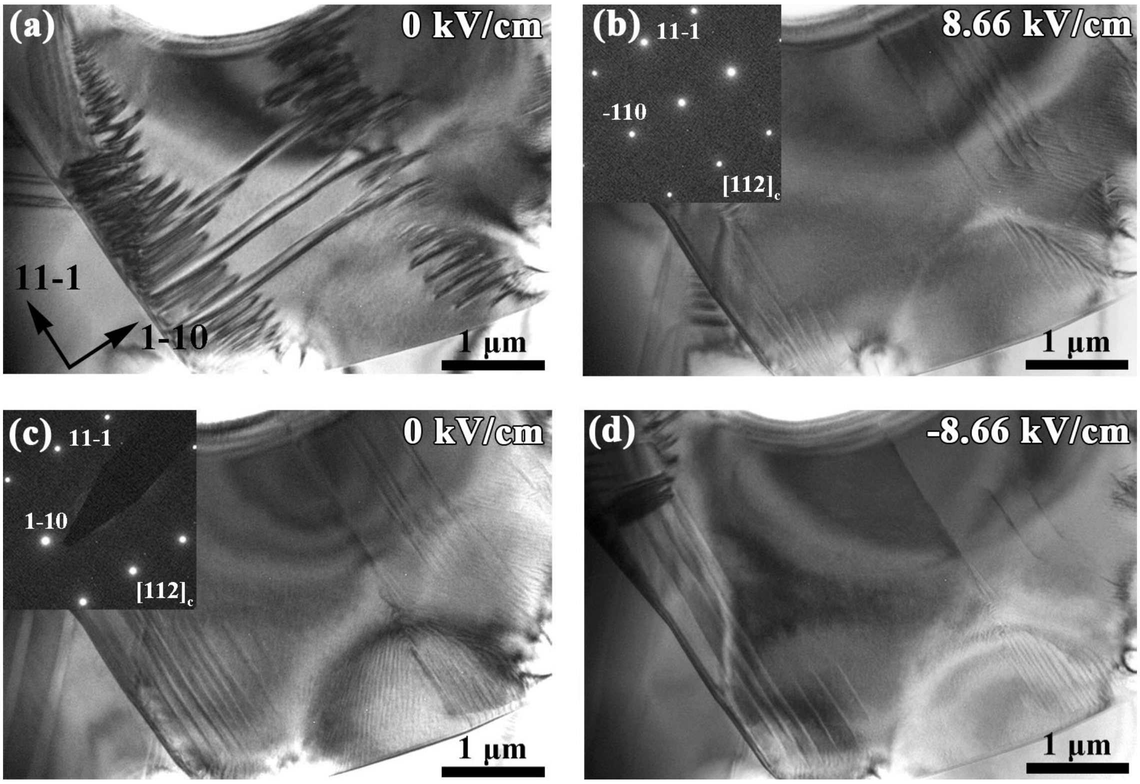

Figure 4.28: *In situ* TEM bright field images of the BZT – 0.60BCT along the $[112]_c$ zone axis at (a) virgin state, (b) 8.66 kV/cm, (c) zero field, (d) –8.66 kV/cm. In the insets of (b) and (c), the corresponding SAED patterns are depicted [140].

The composition dependence of the electric field, at which a single-domain state started to appear (E_{single}), is depicted in Figure 4.29. A tendency of decrease in E_{single} at the area close to the PPT, with its minimum for BZT – 0.48BCT, can be seen. For tetragonal BZT – 0.6BCT composition the single-domain state occurred at a very high poling field, much higher than for rhombohedral and for PPT compositions. This is related to the enhanced value of the coercive field for BZT – 0.6BCT, determined in numerous investigations [20, 147].

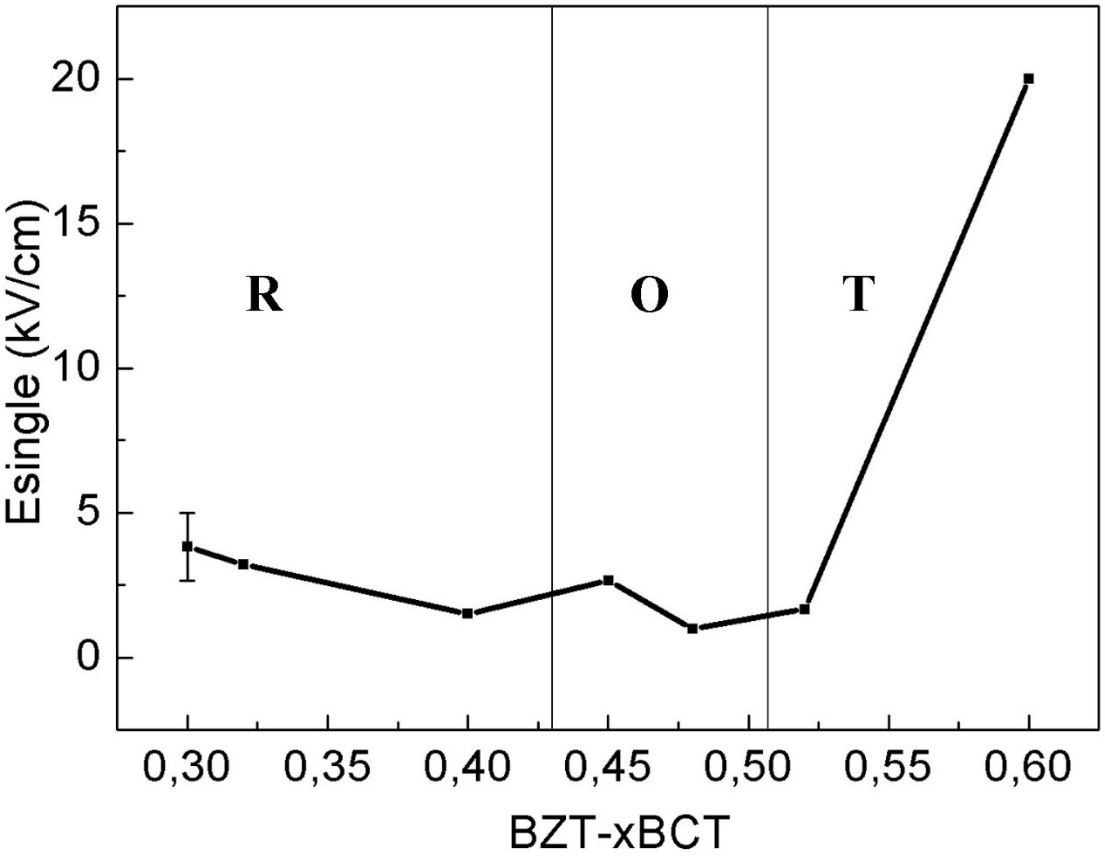

Figure 4.29: The nominal electric field value, at which a single-domain state starts to appear (E_{single}) as a function of composition.

4.7 In situ electric field plus cold-stage TEM investigations

As it was demonstrated in the previous chapter, in comparison with rhombohedral or tetragonal BZT – xBCT, PPT compositions required lower poling fields for the appearance of a single-domain state and, therefore, these compositions can be polarized under a lower electric field. However, the influence of the temperature induced phase transition during the poling process in PPT compositions is not clear. This chapter focuses on the possible electric field induced transformations in BZT – 0.48BCT and BZT – 0.52BCT during phase transitions at low temperatures. The phase diagram of the BZT – xBCT system (Figure 4.30) [23] revealed an orthorhombic-to-rhombohedral phase transition for BZT – 0.48BCT and BZT – 0.52BCT upon decreasing temperature. Changes in the domain morphology during reversible orthorhombic-to-rhombohedral phase transition for these compositions were monitored when varying the temperature range and the electric field values by means of in situ electric field TEM technique with simultaneous cooling.

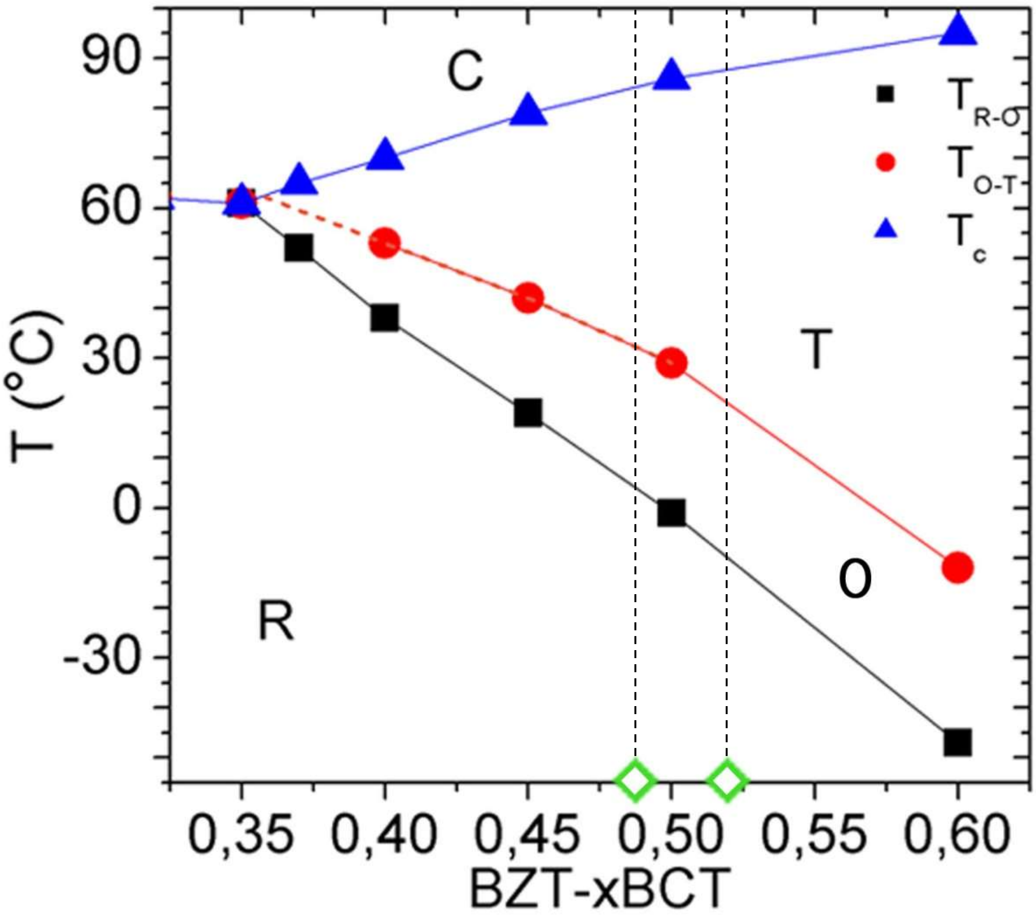

Figure 4.30: Phase diagram of the BZT – xBCT system, proposed by M. Acosta et al. [23]. Green squares denote compositions used for the in situ electric field cold-stage TEM studies.

First RT poling cycle of the BZT – 0.48BCT specimen was demonstrated in the previous chapter (Figure 4.25). After one cycle, at the remanent state domains with a hierarchical structure were visible within the grain (Figure 4.31 (a)). At RT an electric field of 0.3 kV/cm induced a domain switching process and at the nominal poling field of 0.5 kV/cm a single-domain state was achieved (Figure 4.31 (b)). At the electric field of 0.5 kV/cm a temperature decrease led to the multiple domain state formation at -20 °C (Figure 4.31 (d)). This corresponds to the phase transition from O to R at that temperature (Figure 4.30).

BZT – 0.48BCT has an O symmetry at RT, which transforms to the R symmetry below 5 °C [23]. In our studies multiple domains reappeared at -20 °C. This can be related to the additional stress due to the phase transition, which can be reduced by formation of domains or to the fact that at lower temperature BZT – 0.48BCT locates more far away from the PPT region. As polarization switching is impeded for the R phase in comparison to the PPT area [121], higher electric field is required in order to achieve a single-domain state for the R composition.

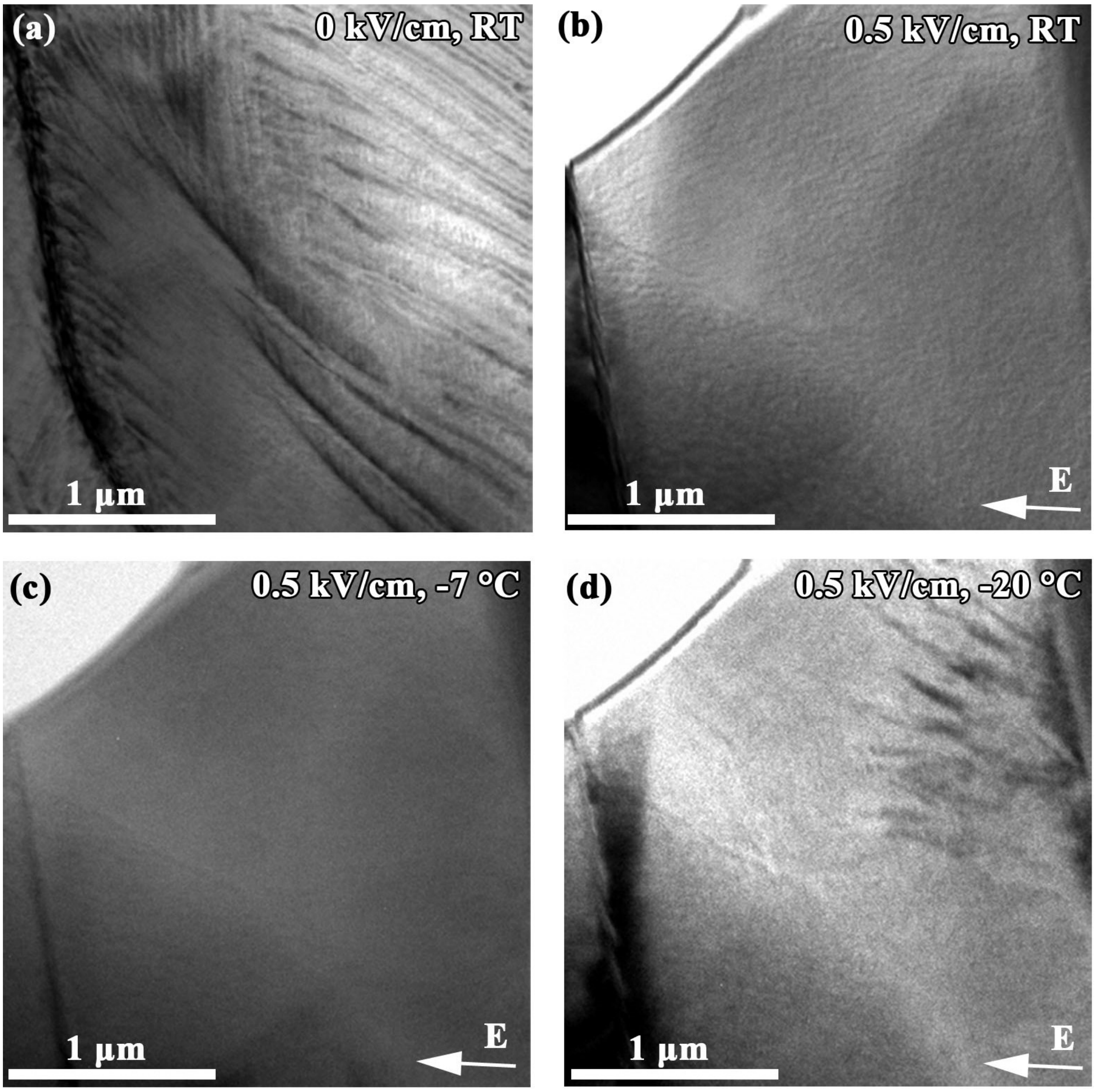

Figure 4.31: *In situ* TEM bright field images of the BZT – 0.48BCT at (a) zero field, RT; (b) 0.5 kV/cm, RT; (c) 0.5 kV/cm, -7 °C; (d) 0.5 kV/cm, -20 °C. The direction of the poling field is indicated by the bright arrow.

In Figure 4.32 (a) a multi-domain configuration of BZT – 0.48BCT specimen is displayed. The specimen was cooled down to -38 °C at the nominal poling field of 0.5 kV/cm. Interestingly, a slight increase in the poling field up to 0.6 kV/cm induced a transformation to the single-domain state at that temperature (Figure 4.32 (b)). During further cooling a multiple domain state reappeared at -48 °C (Figure 4.32 (c)). It should be noted that at the temperature of -48 °C and below the single-domain state have not been observed even at very high poling fields (Figure 4.32 (d)). This is associated with the position of BZT – 0.48BCT in the phase diagram, which is located deep in the R phase region at -48 °C [20, 23, 32]. Hence, in order to achieve a single-domain state in BZT – 0.48BCT at low temperatures, this composition needs to be poled under very high electric field, which is hard to achieve during the *in situ* TEM experiments.

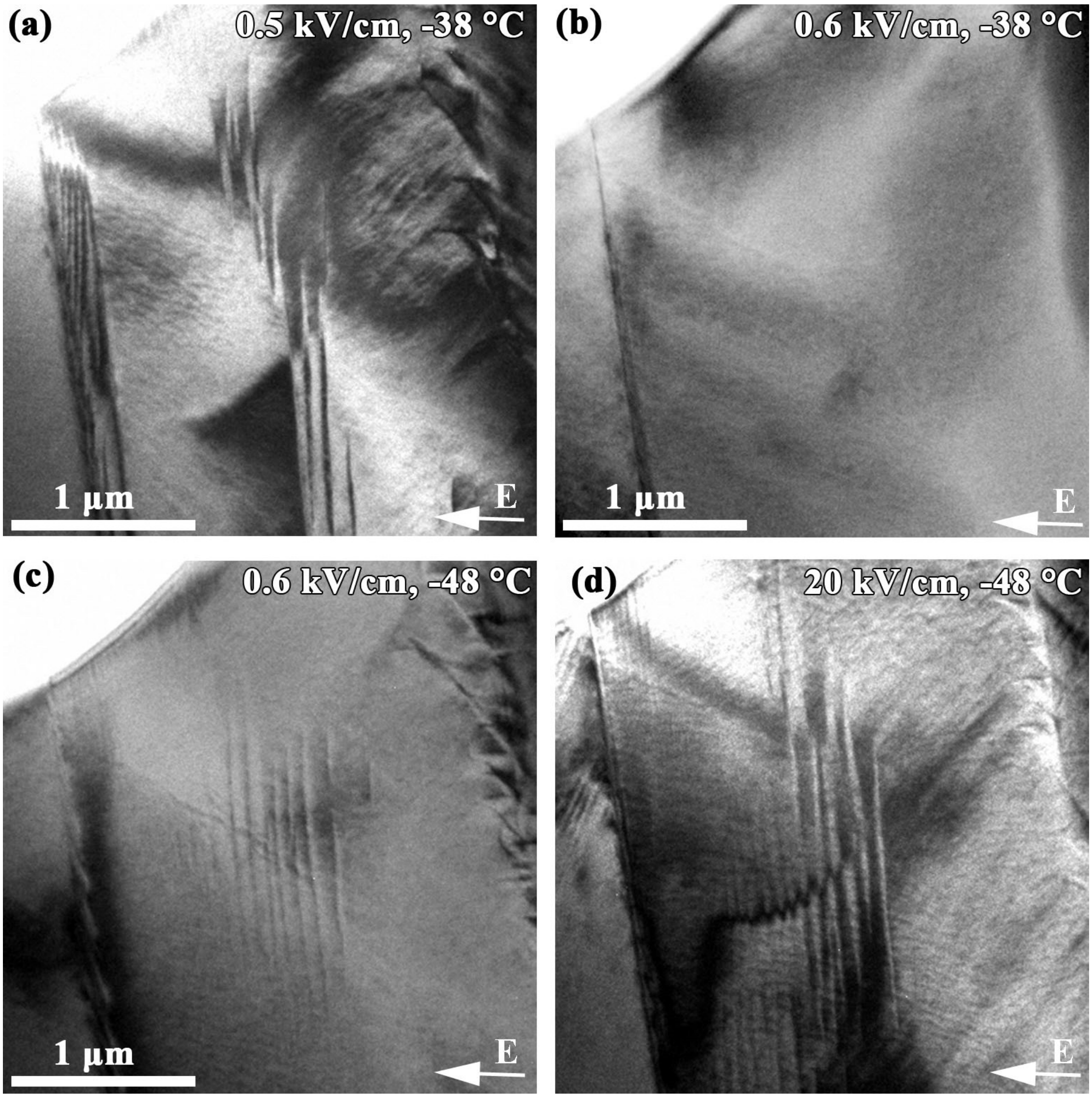

Figure 4.32: *In situ* TEM bright field images of the BZT – 0.48BCT at (a) 0.5 kV/cm, -38 °C; (b) 0.6 kV/cm, -38 °C; (c) 0.6 kV/cm, -48 °C; (d) 20 kV/cm, -48 °C. The direction of the poling field is indicated by the bright arrow.

When the applied field was reduced to the nominal value of 1.2 kV/cm, at -48 °C, lamellar domain contrast was observed within the same grain in the BZT – 0.48BCT piezoceramic (Figure 4.33 (a)). Upon heating (the nominal poling field of 1.2 kV/cm was kept constant) slight changes in the domain morphology were visible. All domain walls disappeared and a whole grain became a large single domain at around 0 °C. As we note before, at this temperature BZT – 0.48BCT is located close to the PPT region (Figure 4.30) and therefore the domain switching and poling process are facilitated. The single-domain state was also present at 10°C and RT (Figure 4.33 (b), (c)). As expected, after removing the external field domain walls reappeared inside the grain, forming a multiple domain state throughout the grain (Figure 4.33 (d)).

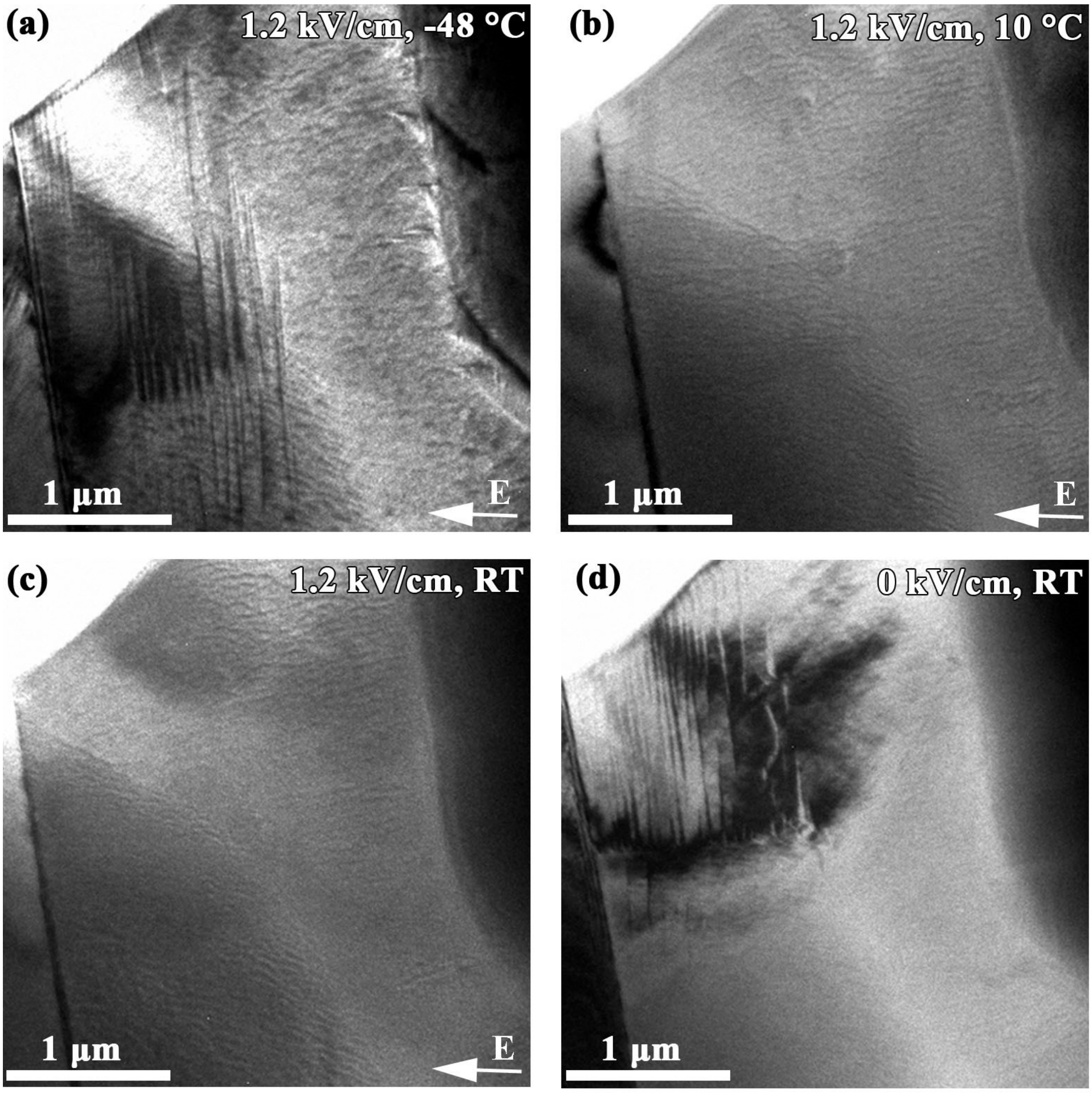

Figure 4.33: *In situ* TEM bright field images of the BZT – 0.48BCT at (a) 1.2 kV/cm, -48 °C; (b) 1.2 kV/cm, 10 °C; (c) 1.2 kV/cm, RT; (d) 0 kV/cm, RT. The direction of the poling field is indicated by the bright arrow.

Figure 4.34 represents the domain evolution, observed in BZT – 0.52BCT during the *in situ* TEM experiments. In the virgin state the grain selected for our studies exhibited a hierarchical domain structure with nanometer sized domains inside domain lamellas (Figure 4.34 (a)), comparable to those of BZT – 0.50BCT [27-30]. When the nominal poling field of 1.5 kV/cm was applied, only lamellar ferroelectric domains were observed within the grain (Figure 4.34 (b)). The single-domain state was reached at the field strength of 2.1 kV/cm (Figure 4.34 (c)). At a constant field of 2.1 kV/cm, no changes in the domain microstructure were observed on cooling down to -15 °C (Figure 4.34 (d)). However, at -30 °C a multiple domain configuration reappeared (Figure 4.34 (e)). This is likely related to the position of BZT – 0.52BCT in the phase diagram, which is far away from the PPT region at that temperature. Hence, higher external fields should be applied to the BZT – 0.52BCT at lower temperatures in order to achieve the single-domain state. Further decrease in the temperature led to the increase in domain volume fraction (Figure 4.34 (f)). A multi- to single-domain state transformation occurred at -23 °C on heating and was present at 55 °C at a field strength of 2.1 kV/cm (Figure 4.34 (g), (h)). After the applied field was removed at 55 °C ferroelectric domains reappeared within the grain (Figure 4.34 (i)).

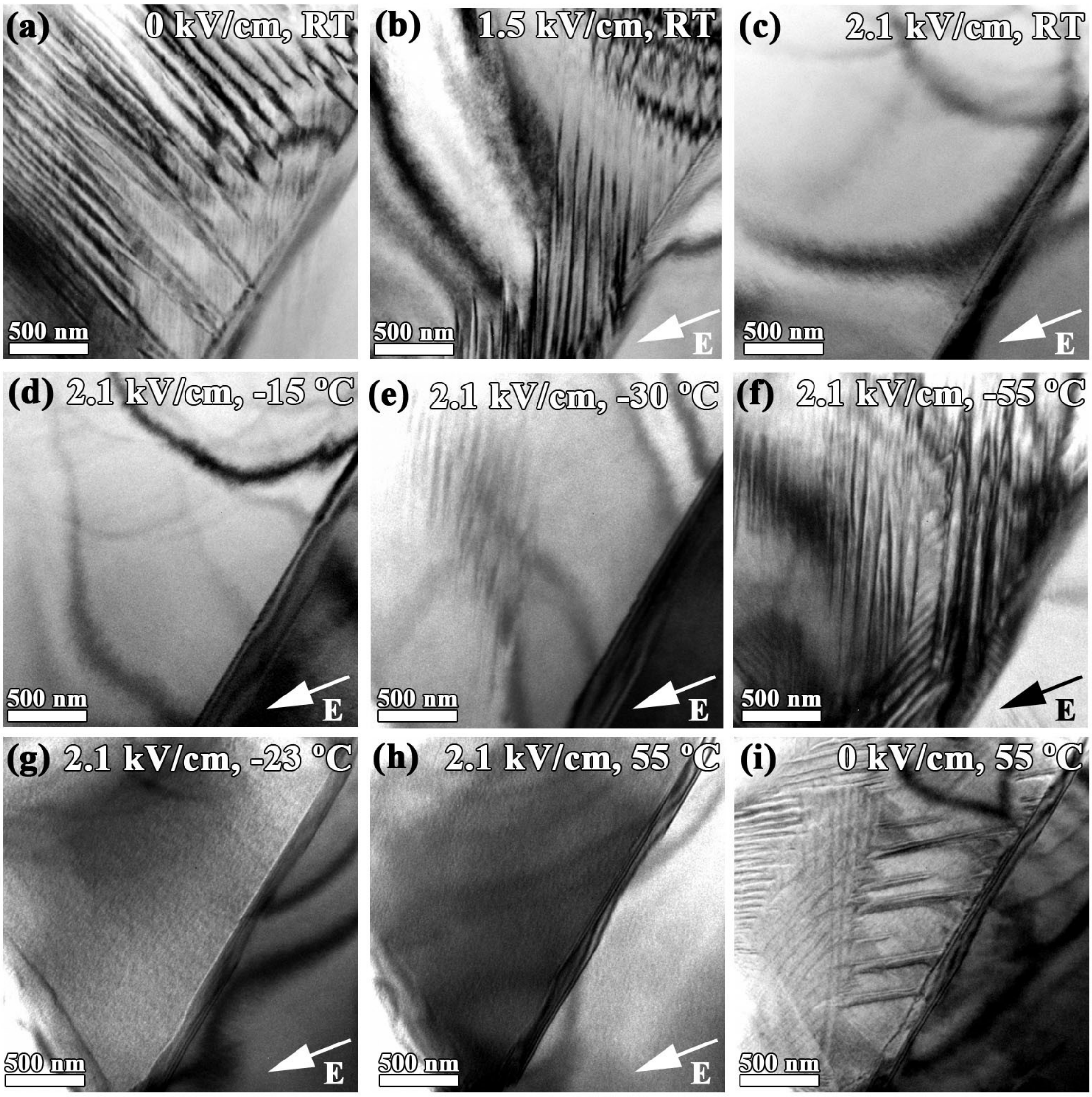

Figure 4.34: *In situ* TEM bright field images of the BZT – 0.52BCT at (a) virgin state, RT; (b) 1.5 kV/cm, RT; (c) 2.1 kV/cm, RT; (d) 2.1 kV/cm, -15 °C; (e) 2.1 kV/cm, -30 °C; (f) 2.1 kV/cm, -55 °C; (g) 2.1 kV/cm, -23 °C; (h) 2.1 kV/cm, 55 °C; (d) 0 kV/cm, 55 °C. The direction of the poling field is indicated by the bright arrow.

For the first time *in situ* electric field TEM studies with simultaneous cooling were conducted on the lead-free BZT – xBCT system. Our results revealed significant changes in the domain morphology of PPT compositions BZT – 0.48BCT and BZT – 0.52BCT during in situ TEM observation. At RT a single-domain state formation occurred at very low poling field of 0.6 kV/cm (during repoling process) for BZT – 0.48BCT and at 2.1 kV/cm for BZT – 0.52BCT (Figure 4.31 (b), Figure 4.34 (c)), which was expected when considering the results from the previous chapter. As the temperature decreased at constant electric field multiple domains reappeared. As it was already mentioned, the reason is likely a temperature induced phase transition to the R phase (Figure 4.30), which requires higher external fields to polarize BZT – 0.48BCT and BZT – 0.52BCT in comparison with the PPT area at RT. This is supported by the fact that the single-domain state in BZT – 0.48BCT was achieved after multi-domain state at low temperature (-38 °C) with a slight increase in the poling field (Figure 4.32 (a), (b)). However, when the temperature was further decreased down to -48 °C a single domain state did not appear even at very high applied field (Figure 4.32 (d)). Therefore, performed in situ TEM experiments confirm that for specimen with compositions far away from the PPT, higher electric fields are necessary in order to obtain a single domain state and thus to polarize the material.

5. Summary

5.1 Discussion

The main purpose of this work was to understand the microstructural features which contribute to the strong electromechanical properties of the lead-free $Ba(Zr_{0.2}Ti_{0.8})O_3$-$x(Ba_{0.7}Ca_{0.3})TiO_3$ piezoelectric ceramic. Detailed conventional TEM studies on a broad variety of BZT – xBCT (with x = 0.3, 0.32, 0.35, 0.4, 0.48, 0.6) were performed in order to demonstrate the composition dependent structural changes. Moreover, several *in situ* TEM techniques, including *in situ* hot- and cold-stage, *in situ* electric field and *in situ* electric field with simultaneous cooling, were successfully applied in order to monitor the domain morphology evolution in real time.

Present conventional TEM investigations showed that the domain configuration in the BZT – xBCT system is clearly composition dependent. According to the results, a microstructure of the rhombohedral BZT – xBCT composition is characterized by the existence of wedge-shaped domains. Formation of such domain configuration can be attributed to the local charges and mechanical stresses [148, 149]. Wedge-shaped domains for rhombohedral BZT – xBCT system were observed in several studies [27, 139]. Previously, such domain morphology was considered as a microstructural feature of the PZT piezoceramics with a rhombohedral crystal structure [45] and was also reported for the rhombohedral $BaTiO_3$ [150]. It should be noted that the rhombohedral domains in BZT – xBCT composition are mainly composed of 109° domains with walls in (110) planes, while 71° domains with (100) domain walls were rarely observed. The reason is a lower surface energy of 109° domains, which is one third of that for 71° type domain walls [151, 152]. This corresponds to results reported by Ricote et al. for rhombohedral PZT [45].

At RT for the BZT – xBCT composition close to the R – O phase boundary domains tend to have curved walls, which do not follow any particular direction. Moreover, during *in situ* TEM experiments domain walls curvature appeared on heating and cooling for compositions within R – O and O – T phase boundaries. We assume that a major reason for domain walls curvature in the PPT compositions BZT – xBCT is the strain caused by mismatch between adjustment of R and T ferroelectric domains, which can coexist at the PPT region.

Nanosized domains which are embedded in the large domain lamellas are characteristic for BZT – xBCT composition in the orthorhombic phase. Such hierarchical domain structure was reported as a distinct feature of the PPT composition BZT – 0.5BCT [27, 28]. Initially, domain hierarchy was obtained in lead-containing materials within the MPB [127-129, 153, 154]. Previously, by means of electron backscatter diffraction (EBSD) domain misorientation was analyzed in tetragonal PZT and $(PbTi)_{0.5}(BiFe)_{0.5}O_3$ [155]. It was shown that junctions of lamellar bands are highly strained. In current studies the microstructure of the tetragonal BZT – xBCT is dominated by lamellar microdomains, which is in agreement with the results obtained by Gao et al. [27].

Our *in situ* TEM observations confirmed a temperature induced ferroelectric – paraelectric phase transition for all studied materials during heating. The temperatures at which the crystal structure transforms to the cubic phase coincides with the Curie temperature, reported for this material [20, 23, 32]. On heating and cooling a microstructure evolution in BZT – xBCT system was observed. As it was already mentioned, irregular domains with curved walls appeared for the compositions at the PPT area due to internal stresses associated with coexistence of rhombohedral and tetragonal domains within one grain. Moreover, *in situ* cold-stage TEM observations on the BZT – 0.5BCT composition confirmed a temperature induced evolution of the domain size from nano- to micron-scale level during transition to the rhombohedral phase, which is in agreement with results obtained by Gao et al. [27].

Domain size analysis revealed an existence of lamellar domains in the submicron range for all studied materials. At the initial state miniaturization of domains down to nanoscale level was detected for the BZT – xBCT compositions close to the PPT region. Previously, nanodomain structure within micron-sized domain lamellas were observed for BZT – 0.5BCT composition by Gao et al. [27, 28]. By means of CBED analysis they showed a coexistence of the miniaturized rhombohedral and tetragonal domains in the BZT – 0.5BCT and associated it with a strong piezoelectricity of this composition [27]. The reduction in the domain size near the phase transition regions is expected from the classical domain theory [156], which predicts that the domain width is proportional to the square root of the domain wall energy ($D \sim \gamma^{1/2}$), which strongly decreases near the phase transition [72]. It should be noted that the areas occupied by nanodomains in the PPT compositions increased with the poling field. According to Wang et al. miniaturized domains can easily respond to the poling field, which results in increased piezoelectric properties [128]. Moreover, during poling a nucleation of the nanometer-sized domains within microdomains occurred for other compositions. Miniaturization of ferroelectric domains facilitates the domain switching under the applied electric field, and hence the poling process. Comparable poling behavior was observed in lead-containing ferroelectrics such as $(Pb_{0.92}La_{0.08})(Zr_{0.65}Ti_{0.35})O_3$ (PLZT) [157] and PZT [130]. It was shown that switching in the PLZT system occurred through the appearance of an intermediate nanodomain state, while in the PZT ferroelectric miniaturized ferroelectric domains were already present in the initial state and responded to the external electric field during the poling process.

Appearance of the single-domain state during *in situ* electric field TEM experiments was observed for all studied piezoceramics. However, as it was shown before, for different compositions this transformation occurred at different poling fields, with the highest value observed for tetragonal BZT – 0.6BCT. This coincides with the high coercive field for that composition [20, 147]. Therefore, higher electric field is required to achieve a proper poling of tetragonal BZT – xBCT in comparison with rhombohedral or PPT compositions. Our results are in good agreement with the calculations of the activation barrier for the nucleation of reversed domains, determined by Zhukov et al. [121]. According to them, the activation barrier is minimum for the PPT composition BZT – 0.48BCT, indicating enhanced polarization switching for this material. This value is increased for the rhombohedral BZT – 0.35BCT composition and achieves its maximum for the tetragonal BZT – 0.6BCT. Therefore, polarization switching was impeded for tetragonal and rhombohedral compositions, which are far away from the PPT. In the present study, the maximum poling field of 20 kV/cm was applied to reach a single-domain state in BZT – 0.6BCT.

Based on the results of the *in situ* electric field experiments the scheme of a domain evolution within one grain during the poling process in BZT – xBCT piezoceramic is suggested (Figure 5.1). With increasing the poling field, a transformation from the multiple domain state (A) to the single-domain state occurred in all studied compositions. Upon field removal multiple domain contrast reappeared, indicating a reversible transformation to the multiple domain state (A) (Figure 5.1). A single-domain state under poling conditions was previously observed only for PPT composition BZT – 0.5BCT and was associated with high piezoelectric properties [29, 30]. In this dissertation a transformation from a multiple- to a single-domain state was observed in all studied materials, even in the tetragonal BZT – 0.6BCT. In several grains this transformation occurred with the appearance of an intermediate nanodomain state (Figure 5.1 (a)). Further rise in the poling field strength leads to the formation of the micron-sized lamellar domains, although the electric field threshold value differed, depending on composition. The formation of the multiple domain state (B) can be associated with the strain incompatibility between neighboring grains under electric field (Figure 5.1 (b)). Under high poling fields each grain represents a single domain. With respect to the external electric field, preferred alignment of the polarization vector cannot be completely achieved within each single grain of the polycrystalline sample. Hence, high strain incompatibility exists between adjacent grains. Consequently, a further transformation from single- to multi-domain state occurs during further increase in field strength. It should be emphasized, that a single-domain state did not appear during diminishing the electric field and it was impossible to achieve it during further poling for almost all studied systems. Only BZT – 0.52BCT composition exhibited a single-domain state formation during re-poling process, which was stable just for a few seconds, suggesting that this state seems to be metastable under the studied conditions. Further cycling enables switching between two different multi-domain states for the majority of studied materials (Figure 5.1 (b)).

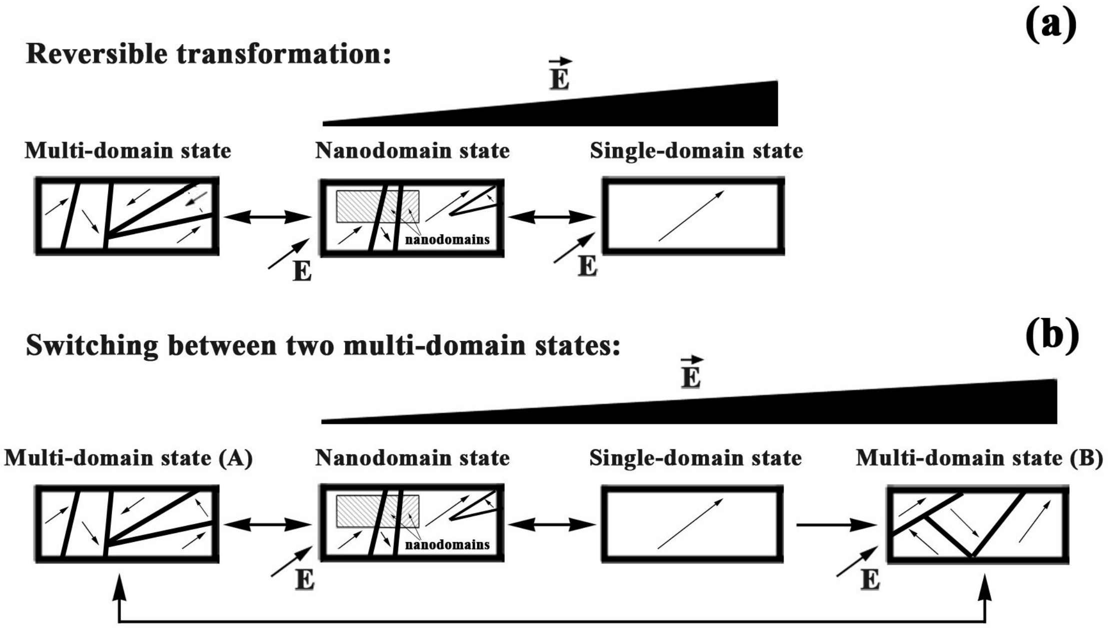

Figure 5.1: The scheme of the domain evolution within one grain in the BZT – xBCT system. (a) Reversible domain transformation: between multi-domain state (A) ↔ nanodomain state ↔ single-domain state, (b) switching between two different multidomain states (A) and (B).

The microstructural evolution in the BZT – xBCT system under an external electric field correlates well with the macroscopic data. For instance, the higher coercive field for tetragonal BZT – 0.6BCT composition correlates with the high poling fields required to induce the single domain state formation in comparison with rhombohedral and PPT compositions. Maximum values in saturation and remanent polarization for PPT compositions correspond to the miniaturization of domains. Enhanced values of maximum and negative strain for BZT – 0.4BCT and BZT – 0.52BCT compositions, which locate near to the (R – O) and (O – T) PPT areas in the phase diagram, respectively, coincide with a reduction in the domain size. A decrease in maximum and negative strain for the BZT – 0.45BCT and a decrease in maximum strain for BZT – 0.5BCT can be attributed to the presence of an orthorhombic structure.

A phase transition from the coexisting R and T phases to the O phase for the BZT – 0.5BCT at poling fields of 4 – 6 kV/cm was recently confirmed by *in situ* x-ray diffraction technique [30]. It was shown that a single-domain state, observed in this composition, corresponds to the O symmetry. Further increase in the poling field (>6 kV/cm) leads to another field induced ferroelectric – ferroelectric phase transition and appearance of the multi-domains in a different phase [30]. Hereby, we speculate that in our study ferroelectric – ferroelectric phase transition occurred for all materials, which lay within the PPT region. Therefore, a single-domain state formation occurred as a result of a phase transition to the orthorhombic phase. Changes in domain morphology in BZT – xBCT compositions, far away from the phase boundary, indicate a field induced switching of ferroelectric domains. Appearance of the miniaturized domain state in these compositions may results from the frustration of lamellar domains due to internal stresses. Domain wall motion in BZT – xBCT system suggests that the predominant electric field induced strain mechanism in BZT – xBCT is due to a high extrinsic contribution and not a phase transition contrary to lead-free BNT-based piezoceramics [158].

During *in situ* electric field plus cold-stage TEM experiments on PPT compositions BZT – xBCT, a single-domain state transformed to a multiple domain state on cooling at constant poling field. According to the phase diagram reported for BZT – xBCT system [20, 23, 32], the temperatures, at which multiple domains appear within the structure, correspond to the rhombohedral phase. Further increase in the poling field value at reduced temperature resulted in a single-domain state formation again. As it was already mentioned, due to increased value of activation barrier for R phase in comparison with PPT [121], polarization switching was impeded. In general, it can be stated that higher electric fields are required in order to polarize the system, which locates deeper in a rhombohedral area of phase diagram, and thus to achieve a single-domain state in the material.

During conventional and *in situ* TEM observations, the SAED patterns revealed neither reflection splitting nor any detectable changes for all studied BZT – xBCT compositions. Reflection splitting is an indication of twinning in the material and therefore should be present in the SAED patterns as long as ferroelectric domains are observed within the grains. Ferroelastic distortions of the unit cell due to mismatch of the crystal lattice of two neighboring domains (except 180° domains) contribute to the reflections splitting [43, 150]. As distortions in the BZT – xBCT system are extremely small, the splitting of the reflections cannot be resolved in the SAED patterns due to saturation limit of the CCD camera. However, recently reported high dynamic range (HDR) electron imaging technique may increase the dynamic range of CCD camera and therefore reduce this limitation [159]. By means of HDR technique the intensity of weak reflections increases while the intensity of strong reflections does not change.

5.2 Conclusions

In this dissertation, the domain structure evolution in lead-free $Ba(Zr_{0.2}Ti_{0.8})O_3$-$x(Ba_{0.7}Ca_{0.3})TiO_3$ piezoelectric ceramic was studied as a function of composition, temperature and applied electric field. It was shown that *in situ* TEM techniques are extremely powerful tools in order to visualize the real-time microstructural evolution over a wide compositional range for a lead-free ferroelectric system.

The microstructure of the BZT – xBCT system in a broad compositional range was characterized by conventional TEM. Composition induced R → O → T phase transition is accompanied by changes in the domain morphology. Thus, wedge-shaped microdomains with needle tips, which are a distinct feature of BZT – xBCT with a rhombohedral structure, transfer to the domain configuration, where nanosized ferroelectric domains are embedded in the micron-sized lamellar domains, typical for the O composition. Transition to the T phase leads to the appearance of large domain lamellas within the grains. Additionally, curved domain walls were observed for the compositions across R – O and O – T PPT areas. Thus, a composition induced domain evolution can be considered as an evidence of the R → O → T phase transition in a BZT – xBCT piezoceramic.

In situ temperature dependent TEM techniques provide an experimental confirmation of the ferroelectric → paraelectric phase transition in the BZT – xBCT system at Curie temperatures, reported for this material [20, 23, 32]. Moreover, during temperature induced R → O → T phase transition in each specific composition the domain morphology changed according to the present crystal structure.

During the *in situ* electric field TEM experiments, a multiple-domain state (A) → nanodomain state → single-domain state transformation occurred during the poling process for all studied materials. With further increase in the applied field a multiple-domain state (B) appeared. This state could be associated with strain incompatibility between neighboring grains under the electric field. The displacement of the domain walls and changes in the domain configuration during electrical poling indicated a high extrinsic contribution to the piezoelectric response in all studied lead-free BZT – xBCT compositions.

By means of *in situ* electric field TEM experiments with simultaneous cooling it was clearly showed that a temperature induced PPT → R phase transition at a moderate field is accompanied by a transformation from a single- to a multiple-domain state. However, a further increase in the poling field led to the reappearance of the single-domain state. Consequently, we obtained experimental evidence that the further the composition deviates from PPT, the higher the electric field, which is required to fully pole the material.

SAED patterns did not reveal any reflection splitting or any detectable changes during *in situ* TEM observations due to very small lattice distortions from a cubic structure, which cannot be resolved by this technique.

5.3 Further Study

The aim of this dissertation was to study the structural features and domain morphology evolution of BZT – xBCT ceramics using different TEM techniques. However, due to a resolution limit of the SAED patterns and absence of the superlattice reflection, the crystal structure of the studied material cannot be directly identified. In order to investigate crystal symmetry and to verify a field induced phase transition a CBED technique should be applied. Special attention should be given to BZT – xBCT compositions near the PPT area, which exhibit a coalescence of miniaturized domains within micron-sized domain lamellas. Local determination of the symmetry will clarify an electric field induced strain mechanisms in PPT compositions. Secondly, a time dependent TEM investigation can shed light on the microstructural evolution during a phase transition and its influence to the electromechanical properties. Such studies can be applied for *in situ* temperature and/or electric field TEM techniques. Finally, considering that ferroelectric devices are often utilized at temperatures higher than room temperature it is essential to perform *in situ* electric field experiments with simultaneous heating. In addition, other promising lead-free piezoelectric materials as $Bi_{1/2}Na_{1/2}TiO_3$- and $K_xNa_{1-x}NbO_3$-based systems require a detailed *in situ* electric field TEM study. Understanding the ferroelectric behavior and the microstructural origin of this system or related lead-free systems allows the tuning of the desired material properties for enhanced applications.

6. Bibliography

1 K. Uchino, Piezoelectric actuators and ultrasonic motors. Springer Science & Business Media (1997).

2 R. Dorey and R. Whatmore, J. Electroceram. 12 (1-2), 19-32 (2004).

3 R. Torah, S. Beeby, M. Tudor and N. White, J. Electroceram. 19 (1), 97-112 (2007).

4 T.-L. Ren, H.-J. Zhao, L.-T. Liu and Z.-J. Li, Mater.Sci. Eng.B 99 (1–3), 159-163 (2003).

5 Innovative Research and Products. Inc., Stamford, CT, USA (2013).

6 B. Jaffe, W. R. Cook and H. Jaffe, Piezoelectric Ceramics. Academic Press Inc. (1971).

7 EU-Directive 2011/65/EU, Official Journal of the European Union, 88 - 110 (2011).

8 G. A. Smolenskii, V. A. Isupov, A. I. Agranovskaya and N. N. Krainik, Sov. Phys. Solid State 2, 2651-2654 (1961).

9 T. Takenaka, H. Nagata, Y. Hiruma, Y. Yoshii and K. Matumoto, J. Electroceram. 19 (4), 259-265 (2007).

10 G. O. Jones and P. A. Thomas, Acta Cryst. B 56, 426-430 (2000).

11 L. A. Schmitt, J. Kling, M. Hinterstein, M. Hoelzel, W. Jo, H.-J. Kleebe and H. Fuess, J. Mater. Sci. 46 (12), 4368-4376 (2011).

12 S.-T. Zhang, A. B. Kounga, E. Aulbach and Y. Deng, J. Am. Ceram. Soc. 91 (12), 3950-3954 (2008).

13 W. C. Lee, Y. F. Lee, M. H. Tseng, C.-Y. Huang and Y.-C. Wu, J. Am. Ceram. Soc. 92 (5), 1069-1073 (2009).

14 S.-T. Zhang, A. B. Kounga, E. Aulbach, H. Ehrenberg and J. Rödel, Appl. Phys. Let. 91 (11), 112906 (2007).

15 J. Rödel, W. Jo, K. T. P. Seifert, E.-M. Anton, T. Granzow and D. Damjanovic, J. Am. Ceram. Soc. 92 (6), 1153 - 1177 (2009).

16 Y. Saito, H. Takao, T. Tani and T. Nonoyama, Nature 432, 2-5 (2004).

17 D. Damjanovic, N. Klein, J. Li and V. Porokhonskyy, Funct. Mater. Lett. 03 (01), 5-13 (2010).

18 T. Takenaka, K.-i. Maruyama and K. Sakata, Jpn. J. Appl. Phys. 30 (9S), 2236 (1991).

19 Y. M. Chiang, G. W. Farrey and A. N. Soukhojak, Appl. Phys. Lett. 73 (25), 3683-3685 (1998).

20 W. Liu and X. Ren, Phys. Rev. Lett. 103 (25), 257602 (2009).

21 D. Xue, Y. Zhou, H. Bao, C. Zhou, J. Gao and X. Ren, J. Appl. Phys 109 (5), 054110 (2011).

22 W. Wang, W. L. Li, D. Xu, W. P. Cao, Y. F. Hou and W. D. Fei, Ceram. Int. (3), 3933-3937 (2014).

23 M. Acosta, N. Novak, W. Jo, J. Rödel and W. Jo, Acta. Mater. 80, 48 - 55 (2014).

24 P. Mishra and P. Kumar, Ceram. Int. 40 (9), 14149-14157 (2014).

25 J. Gao, X. Hu, L. Zhang, F. Li, L. Zhang, Y. Wang, Y. Hao, L. Zhong and X. Ren, Appl. Phys. Lett. 104 (25), 252909 (2014).

26 M. C. Ehmke, J. Glaum, M. Hoffman, J. E. Blendell and K. J. Bowman, J. Am. Ceram. Soc. 96 (9), 2913-2920 (2013).

27 J. Gao, D. Xue, Y. Wang, D. Wang and L. Zhang, Appl. Phys. Lett. 99 (9), 092901 (2011).

28 J. Gao, L. Zhang, D. Xue, T. Kimoto, M. Song, L. Zhong and X. Ren, J. Appl. Phys. 115 (5), 054108 (2014).

29 H. Guo, C. Zhou, X. Ren and X. Tan, Phys. Rev. B 89 (10), 100104 (2014).

30 H. Guo, B. K. Voas, S. Zhang, C. Zhou, X. Ren, S. P. Beckman and X. Tan, Phys. Rev. B 90 (1), 014103 (2014).

31 H. Bao, C. Zhou, D. Xue, J. Gao and X. Ren, J. Phys. D: Appl. Phys. 43 (46), 465401 (2010).

32 D. S. Keeble, F. Benabdallah, P. A. Thomas, M. Maglione and J. Kreisel, Appl. Phys. Lett. 102 (9), 092903 (2013).

33 K. Yao, K. Uchino, Y. Xu, S. Dong and L. C. Lim, Trans. Ultrason., Ferroelect., Freq. Control. 47 (4), 819-825 (2000).

34 Z. Wu, B. Wu and S. Cochran, Investigation of elevated temperature effects on multiple layer piezoelectric ultrasonic transducers with adhesive bondlines by self-heating. INTECH Open Access Publisher (2010).

35 A. A. Bokov and Z. G. Ye, J. Mater. Sci. 41 (1), 31-52 (2006).

36 L. E. Cross, Ferroelectrics 76 (1), 241-267 (1987).

37 X. Zhao, W. Qu, X. Tan, A. Bokov and Z.-G. Ye, Phys. Rev. B 75 (10), 104106 (2007).

38 G. A. e. Smolenskii, J. Phys. Soc. Jpn 28 (Suppl), 26-37 (1970).

39 A. J. Moulson and J. M. Herbert, Electroceramics: materials, properties, applications. (John Wiley & Sons, 2003).

40 R. Waser, U. Böttger and S. Tiedke, Polar oxides: properties, characterization, and imaging. (John Wiley & Sons, 2006).

41 R. Dittmer, PhD Thesis, TUD (2013).

42 D. Damjanovic, Rep. Prog. Phys. 61, 1267-1324 (1998).

43 Y. H. Hu, H. M. Chan, Z. X. Wen and M. P. Harmer, J. Am. Ceram. Soc. 69 (8), 594-602 (1986).

44 R. Schierholz and H. Fuess, J. Appl. Crystal. 45 (4), 766-777 (2012).

45 J. Ricote, R. W. Whatmore and D. J. Barber, J. Phys.: Condens. Matter 12, 323 - 337 (2000).

46 Y. U. Wang, Phys. Rev. B 76 (2), 024108 (2007).

47 G. Rose, De novis quibusdam fossilibus quae in montibus uraliis inveniuntur. (typis A.G. Schadii, Berolini, 1839).

48 M. A. Islam, J. M. Rondinelli and J. E. Spanier, J. Phys. Condens. Matter. 25 (17), 175902 (2013).

49 J. Kling, PhD Thesis, TUD, 2011.

50 A. Glazer, Acta Cryst. B: Structural Crystallography and Crystal Chemistry 28 (11), 3384-3392 (1972).

51 A. Glazer, Acta Cryst. A: Crystal Physics, Diffraction, Theoretical and General Crystallography 31 (6), 756-762 (1975).

52 V. Goldschmidt, Trans. Faraday Soc. 25, 253-283 (1929).

53 R. Shannon, Acta Cryst. A 32 (5), 751-767 (1976).

54 S. Sasart, T. Cnenl-es and C. Ltesenmann, Am. Mineral. 68, 1189-1198 (1983).

55 D. I. Bilc and D. J. Singh, Phys. Rev. Lett. 96 (14), 147602 (2006).

56 P. Baettig, C. F. Schelle, R. LeSar, U. V. Waghmare and N. A. Spaldin, Chem. Mat.17 (6), 1376-1380 (2005).

57 N. A. Benedek and C. J. Fennie, J. Phys. Chem. C 117 (26), 13339-13349 (2013).

58 P. Woodward, Acta Cryst. B 53 (1), 32-43 (1997).

59 G. Shirane, K. Suzuki and A. Takeda, JPSJ 7 (1), 12-18 (1952).

60 G. H. Haertling, J. Am. Ceram. Soc. 82 (4), 797-818 (1999).

61 D. Damjanovic and R. Newnham, J. Intell. Mater. Syst. Struct. 3 (2), 190-208 (1992).

62 J. Scott, science 315 (5814), 954-959 (2007).

63 M. Ahart, M. Somayazulu, R. Cohen, P. Ganesh, P. Dera, H.-k. Mao, R. J. Hemley, Y. Ren, P. Liermann and Z. Wu, Nature 451 (7178), 545-548 (2008).

64 E. Sawaguchi, H. Maniwa and S. Hoshino, Phys. Rev. 83 (5), 1078 (1951).

65 B. Noheda, D. E. Cox, G. Shirane, J. A. Gonzalo, L. E. Cross and S.-E. Park, Appl. Phys. Lett. 74 (14), 2059-2061 (1999).

66 B. Noheda, D. E. Cox, G. Shirane, R. Guo, B. Jones and L. E. Cross, Phys. Rev. B 63 (1), 014103 (2000).

67 L. Bellaiche, A. García and D. Vanderbilt, Phys. Rev. Lett. 84 (23), 5427 (2000).

68 D. Tenne, A. Bruchhausen, N. Lanzillotti-Kimura, A. Fainstein, R. Katiyar, A. Cantarero, A. Soukiassian, V. Vaithyanathan, J. Haeni and W. Tian, Science 313 (5793), 1614-1616 (2006).

69 V. Isupov, Phys. Solid State 43 (12), 2262-2266 (2001).

70 K. A. Schönau, L. A. Schmitt, M. Knapp, H. Fuess, R.-A. Eichel, H. Kungl and M. J. Hoffmann, Phys. Rev. B 75 (18), 184117 (2007).
71 D. Damjanovic, Appl. Phys. Lett. 97 (6), 062906 (2010).
72 G. A. Rossetti, A. G. Khachaturyan, G. Akcay and Y. Ni, J.Appl. Phys. 103 (11), 114113 (2008).
73 H. Fu and R. E. Cohen, Nature 403 (6767), 281-283 (2000).
74 A. Safari and E. K. Akdogan, Piezoelectric and acoustic materials for transducer applications. (Springer Science & Business Media, 2008).
75 D. Viehland, J. Am. Ceram. Soc. 89 (3), 775-785 (2006).
76 E. Aksel and J. L. Jones, Sensors (Basel, Switzerland) 10 (3), 1935-1954 (2010).
77 G. Jones and P. Thomas, Acta Cryst. B: Structural Science 58 (2), 168-178 (2002).
78 K. Sakata and Y. Masuda, Ferroelectrics 7 (1), 347-349 (1974).
79 S. Vakhrushev, V. Isupov, B. Kvyatkovsky, N. Okuneva, I. Pronin, G. Smolensky and P. Syrnikov, Ferroelectrics 63 (1), 153-160 (1985).
80 J. Suchanicz, Ferroelectrics 209 (1), 561-568 (1998).
81 V. A. Isupov and T. V. Kruzina, Izv. Akad. Nauk SSSR, Series of Physics 47, 616 (1983).
82 C.-S. Tu, I. Siny and V. Schmidt, Phys. Rev. B 49 (17), 11550 (1994).
83 C. Xu, D. Lin and K. Kwok, Solid State Sciences 10 (7), 934-940 (2008).
84 Y. Hiruma, H. Nagata and T. Takenaka, J. App. Phys. 105 (8), 084112-084112-084118 (2009).
85 L. A. Schmitt, M. Hinterstein, H.-J. Kleebe and H. Fuess, J. Appl. Crystal. 43 (4), 805-810 (2010).
86 T. Takenaka, Ferroelectrics 230 (1), 87-98 (1999).
87 T. Takenaka, K. O. Sakata and K. O. Toda, Ferroelectrics 106 (1), 375-380 (1990).
88 X. Wang, K. Kwok, X. Tang, H. Chan and C. Choy, Solid State Communications 129 (5), 319-323 (2004).
89 H. Yu and Z.-G. Ye, Appl. Phys. Lett. 93 (11), 112902 (2008).
90 A. B. Kounga, S.-T. Zhang, W. Jo, T. Granzow and J. Rodel, Appl. Phys. Lett. 92 (22), 222902-222903 (2008).
91 Y. Hiruma, K. Yoshii, H. Nagata and T. Takenaka, J. App. Phys. 103 (8), 084121-084121-084127 (2008).
92 J. Rödel, W. Jo, K. T. Seifert, E. M. Anton, T. Granzow and D. Damjanovic, J. Am. Ceram. Soc. 92 (6), 1153-1177 (2009).
93 B.-J. Chu, D.-R. Chen, G.-R. Li and Q.-R. Yin, J. Eu. Ceram. Soc 22 (13), 2115-2121 (2002).
94 Q. Xu, S. Chen, W. Chen, S. Wu, J. Zhou, H. Sun and Y. Li, Mater. Chem. Phys. 90 (1), 111-115 (2005).
95 M. Chen, Q. Xu, B. H. Kim, B. K. Ahn, J. H. Ko, W. J. Kang and O. J. Nam, J. Eu. Ceram. Soc.28 (4), 843-849 (2008).
96 S. T. Zhang, A. B. Kounga, E. Aulbach and Y. Deng, J. Am. Ceram. Soc. 91 (12), 3950-3954 (2008).
97 W. Jo, J. E. Daniels, J. L. Jones, X. Tan, P. A. Thomas, D. Damjanovic and J. Rödel, J. App. Phys. 109 (1), 014110 (2011).
98 J. Park, S. Lee, M. Lee, D. Kim, Y. Sung, M. Kim, T. Song, J. Cho, B. Choi and S. Kim, J. Korean. Phys. Soc. 57, 1905 (2010).
99 T. Song, M.-H. Kim, Y.-S. Sung, H. Yeo, S. Lee, S.-J. Jeong and J.-S. Song, J. Korean. Phys. Soc. 51, 697 (2007).
100 A. Sasaki, T. Chiba, Y. Mamiya and E. Otsuki, Japanese J. App. Phys. 38 (9S), 5564 (1999).
101 Y. R. Zhang, J. F. Li and B. P. Zhang, J. Am. Ceram. Soc. 91 (8), 2716-2719 (2008).
102 K. Yoshii, Y. Hiruma, H. Nagata and T. Takenaka, Jpn. J. App. Phys.45 (5S), 4493 (2006).
103 Y. Hiruma, H. Nagata and T. Takenaka, J. App. Phys. 104 (12), 124106-124106-124107 (2008).
104 C. Peng, J.-F. Li and W. Gong, Materials Letters 59 (12), 1576-1580 (2005).
105 Z. Chen, A. Shui, Z. Lu and P. Liu, Nippon seramikkusu kyokai gakujutsu ronbunshi 114 (10), 857-860 (2006).

106 Y. Sung, J. Kim, J. Cho, T. Song, M. Kim and T. Park, Applied Physics Letters 96 (20), 202901-202901-202903 (2010).

107 N. Sawangwan, J. Tontrakoon and T. Tunkasiri, Ferroelectrics 358 (1), 103-108 (2007).

108 J. Hao, W. Bai, W. Li and J. Zhai, J. Am. Ceram. Soc. 95 (6), 1998-2006 (2012).

109 A. B. Haugen, J. S. Forrester, D. Damjanovic, B. Li, K. J. Bowman and J. L. Jones, J. App. Phys. 113 (1), 014103 (2013).

110 W. Li, Z. Xu, R. Chu, P. Fu and G. Zang, Physica B: Condensed Matter 405 (21), 4513-4516 (2010).

111 Y. Tian, L. Wei, X. Chao, Z. Liu and Z. Yang, J. Am. Ceram. Soc. 96 (2), 496-502 (2013).

112 M. C. Ehmke, S. N. Ehrlich, J. E. Blendell and K. J. Bowman, J. Appl. Phys. 111 (12), 124110 (2012).

113 F. Benabdallah, A. Simon, H. Khemakhem, C. Elissalde and M. Maglione, J. Appl. Phys. 109 (12), 124116 (2011).

114 D. E. Cox, B. Noheda, G. Shirane, Y. Uesu, K. Fujishiro and Y. Yamada, Appl.Phys.Lett. 79 (3), 400 (2001).

115 D. Damjanovic, A. Biancoli, L. Batooli, A. Vahabzadeh and J. Trodahl, Appl. Phys. Lett. 100 (19), 192907 (2012).

116 D. R. J. Brandt, M. Acosta, J. Koruza and K. G. Webber, J. Appl. Phys. 115 (20), 204107 (2014).

117 L. Zhang, M. Zhang, L. Wang, C. Zhou, Z. Zhang, Y. Yao, L. Zhang, D. Xue, X. Lou and X. Ren,Appl.Phys.Lett. 105 (16), 162908 (2014).

118 M. Acosta, N. Khakpash, T. Someya, N. Novak, W. Jo, H. Nagata, G. A. Rossetti and J. Rödel, Phys. Rev. B 91 (10), 104108 (2015).

119 J. Wu, D. Xiao, W. Wu, Q. Chen, J. Zhu, Z. Yang and J. Wang, J. Eu. Ceram. Soc 32 (4), 891-898 (2012).

120 W. Li, Z. Xu, R. Chu, P. Fu and G. Zang, J. Am. Ceram. Soc. 93 (10), 2942-2944 (2010).

121 S. Zhukov, Y. A. Genenko, M. Acosta, H. Humburg, W. Jo, J. Rödel and H. von Seggern, Appl.Phys. Lett. 103 (15), 152904 (2013).

122 G. Tutuncu, B. Li, K. Bowman and J. L. Jones, J. Appl. Phys. 115, 144104 (2014).

123 M. Zakhozheva, L. A. Schmitt, M. Acosta, W. Jo, J. Rödel and H.-J. Kleebe, Appl.Phys.Lett. 105 (11), 112904 (2014).

124 L. A. Schmitt, H. Kungl, M. Hinterstein, L. Riekehr, H. J. Kleebe, M. J. Hoffmann, R. A. Eichel and H. Fuess, J. Am. Ceram. Soc. 98 (1), 269-277 (2015).

125 V. Dorcet, G. Trolliard and P. Boullay, Chem. Mat. 20 (15), 5061-5073 (2008).

126 C. Ma and X. Tan, J. Am. Ceram. Soc. 94 (11), 4040-4044 (2011).

127 F. Bai, J. Li and D. Viehland,Appl.Phys.Lett. 85 (12), 2313-2315 (2004).

128 H. Wang, J. Zhu, N. Lu, A. A. Bokov, Z.-G. Ye and X. W. Zhang, Appl.Phys.Lett. 89 (4), 04298 (2006).

129 H. Wang, J. Zhu, X. W. Zhang, Y. X. Tang and H. S. Luo, Appl.Phys.Lett. 92 (13), 132906 (2008).

130 R. Theissmann, L. A. Schmitt, J. Kling, R. Schierholz, K. A. Schönau, H. Fuess, M. Knapp, H. Kungl and M. J. Hoffmann, J. App. Phys. 102 (2), 024111 (2007).

131 X. Tan, H. He and J.-K. Shang, Journal of materials research 20 (07), 1641-1653 (2005).

132 C. Ma, H. Guo, S. P. Beckman and X. Tan, Phys. Rev. Lett. 109 (10), 107602 (2012).

133 L. S. Lucato, Department of Materials Science, Darmstadt University of Technology, Darmstadt, Germany (1999).

134 J. I. Goldstein, D. E. Newbury, P. Echlin, D. C. Joy, C. Fiori and E. Lifshin, Scanning electron microscopy and X-ray microanalysis. A text for biologists, materials scientists, and geologists. (Plenum Publishing Corporation, 1981).

135 T. Everhart and R. Thornley, Journal of scientific instruments 37 (7), 246 (1960).

136 D. B. Williams and C. B. Carter, The transmission electron microscope. (Springer, 1996).

137 R. Schierholz, PhD Thesis, TUD, 2010.

138 A. Srinivas, R. V. Krishnaiah, V. L. Niranjani, S. V. Kamat, T. Karthik and S. Asthana, Ceramics International 41 (2, Part A), 1980-1985 (2015).

139 S. Lu, Z. Xu, S. Su and R. Zuo, Appl.Phys.Lett. 105 (3), - (2014).
140 M. Zakhozheva, L. Schmitt, M. Acosta, H. Guo, W. Jo, R. Schierholz, H.-J. Kleebe and X. Tan, Phys. Rev. Appl. 3 (6), 064018 (2015).
141 X. Dai, Z. Xu and D. Viehland, Philosophical Magazine B 70 (1), 33-48 (1994).
142 G. Rossetti Jr, G. Popov, E. Zlotnikov and N. Yao, Materials Science and Engineering: A 433 (1), 124-132 (2006).
143 J. Wang, S. Jiang, D. Jiang, J. Tian, Y. Li and Y. Wang, Ceramics International 38 (7), 5853-5857 (2012).
144 J. Yao, L. Yan, W. Ge, L. Luo, J. Li, D. Viehland, Q. Zhang and H. Luo, Phys. Rev. B 83 (5), 054107 (2011).
145 A. A. Bokov and Z.-G. Ye, J. App. Phys. 95 (11), 6347-6359 (2004).
146 C. W. Tai, S. H. Choy and H. L. W. Chan, J. Am. Ceram. Soc. 91 (10), 3335-3341 (2008).
147 M. Zakhozheva, L. A. Schmitt, M. Acosta, H. Guo, W. Jo, J. Rödel, H.-J. Kleebe and X. Tan.
148 A. Krishnan, M. Treacy, M. Bisher, P. Chandra and P. Littlewood, presented at the AIP Conference Proceeding 2000 (unpublished).
149 L. A. Schmitt, D. Schrade, H. Kungl, B.-X. Xu, R. Mueller, M. J. Hoffmann, H.-J. Kleebe and H. Fuess, Computational Materials Science 81, 123 - 132 (2014).
150 M. Tanaka and G. Honjo, JPSJ 19 (6), 954-970 (1964).
151 C. Randall, D. Barber and R. Whatmore, J. Mater. Sci. 22 (3), 925-931 (1987).
152 V. Zhirnov, Soviet Physics Jetp-Ussr 8 (5), 822-825 (1959).
153 H. Wu, D. Xue, D. Lv, J. Gao, S. Guo, Y. Zhou, X. Ding, C. Zhou, S. Yang and Y. Yang, J. App. Phys. 112 (5), 052004 (2012).
154 K. Kurushima, K. Kobayashi and S. Mori, presented at the Applications of Ferroelectrics (ISAF/PFM), 2011 International Symposium on and 2011 International Symposium on Piezoresponse Force Microscopy and Nanoscale Phenomena in Polar Materials, 2011 (unpublished).
155 M. Farooq, R. Villaurrutia, I. MacLaren, T. Burnett, T. Comyn, A. Bell, H. Kungl and M. Hoffmann, J. App. Phys. 104 (2), 024111 (2008).
156 M. E. Lines and A. M. Glass, Principles and applications of ferroelectrics and related materials. (Clarendon press Oxford, 2001).
157 S. Schaab and T. Granzow, Appl.Phys.Lett. 97 (13), 132902 (2010).
158 M. Hinterstein, M. Knapp, M. Holzel, W. Jo, A. Cervellino, H. Ehrenberg and H. Fuess, J. Appl. Crystal. 43 (6), 1314-1321 (2010).
159 K. Evans and R. Beanland, Microscopy and Microanalysis 20 (05), 1601-1604 (2014).

7. Appendix I: Chemical analysis

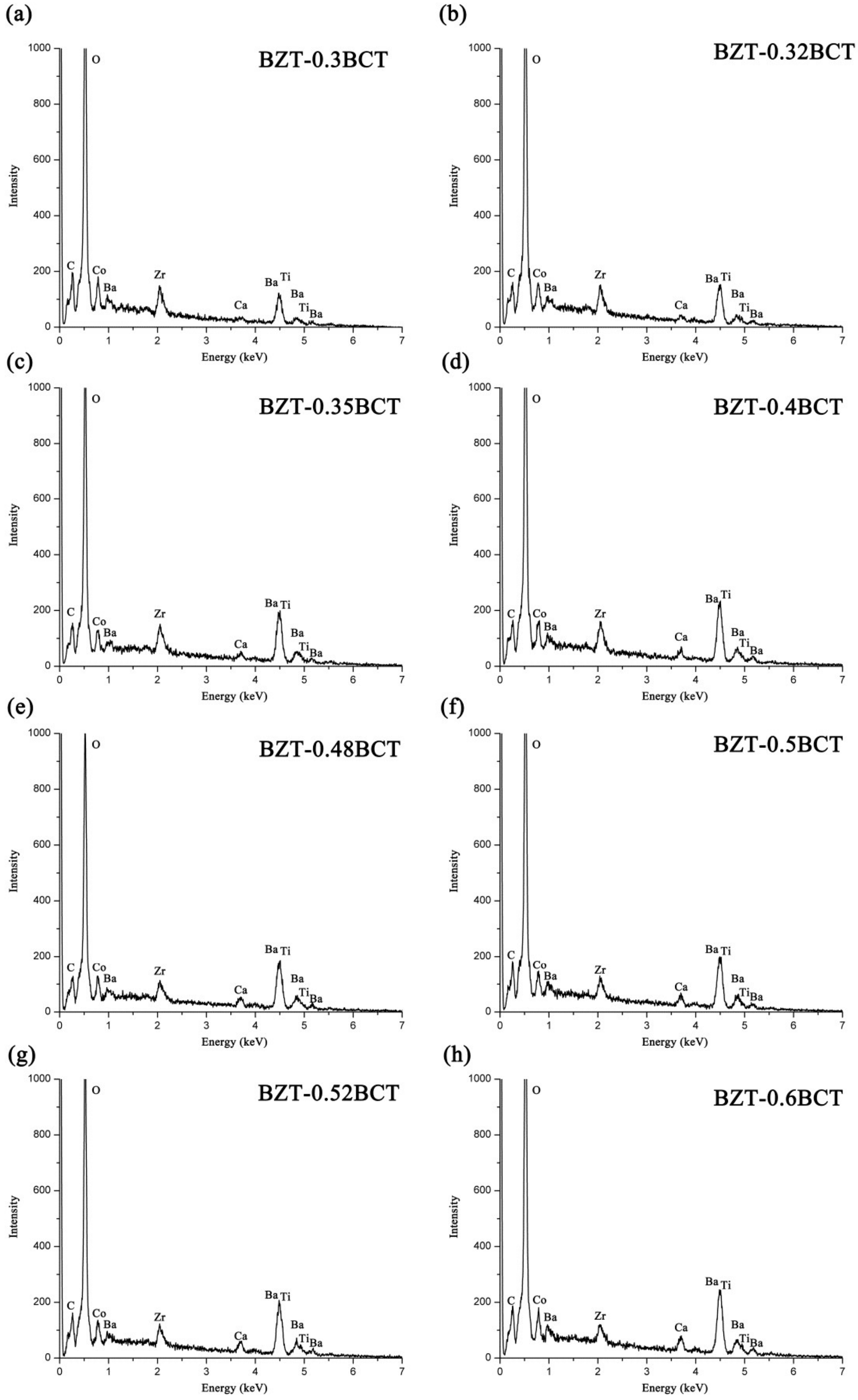

Figure 7.1: EDX spectra of the (a) BZT-0.3BCT, (b) BZT-0.32BCT, (c) BZT-0.35BCT, (d) BZT-0.4BCT, (e) BZT-0.48BCT, (f) BZT-0.5BCT, (g) BZT-0.52BCT, (h) BZT-0.6BCT.

Table 7.1: Weight percent of elements in the $Ba(Zr_{0.2}Ti_{0.8})O_3$-x$(Ba_{0.7}Ca_{0.3})TiO_3$ determined from the stoichiometric formula.

Composition	Ba, wt %	Zr, wt %	Ca, wt %	Ti, wt %	O, wt %
BZT-0.3BCT	54.21	5.54	1.56	17.85	20.82
BZT-0.32BCT	54.03	5.409	1.67	18.00	20.89
BZT-0.35BCT	53.76	5.19	1.84	18.22	20.99
BZT-0.4BCT	53.30	4.83	2.12	18.57	21.17
BZT-0.45BCT	52.83	4.46	2.41	18.94	21.35
BZT-0.48BCT	52.55	4.24	2.58	19.17	21.45
BZT-0.5BCT	52.36	4.09	2.69	19.32	21.53
BZT-0.52BCT	52.16	3.94	2.81	19.47	21.60
BZT-0.6BCT	51.38	3.33	3.29	20.09	21.90

Table 7.2:Weight percent of elements in the $Ba(Zr_{0.2}Ti_{0.8})O_3$-x$(Ba_{0.7}Ca_{0.3})TiO_3$ obtained from the EDX analysis.

Composition	Ba, wt %	Zr, wt %	Ca, wt %	Ti, wt %	O, wt %
BZT-0.3BCT	40.06	8.08	1.29	14.26	36.31
BZT-0.32BCT	51.93	5.71	1.59	16.87	23.89
BZT-0.35BCT	51.79	6.11	1.62	16.06	24.40
BZT-0.4BCT	51.49	5.71	1.88	16.26	24.64
BZT-0.45BCT	50.15	5.18	2.12	17.16	25.37
BZT-0.48BCT	52.57	4.63	2.29	17.24	23.25
BZT-0.5BCT	49.68	4.65	2.67	17.45	25.55
BZT-0.52BCT	50.20	4.66	2.69	17.07	25.37
BZT-0.6BCT	48.75	3.91	2.79	19.06	25.48

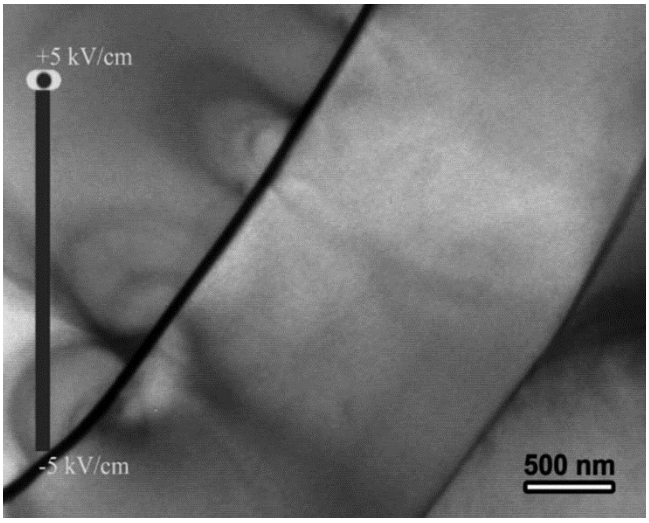

Figure 7.2: TEM bright field image of the BZT-0.3BCT extracted from the in situ TEM movie. Three adjacent grains at an electric field of +5 kV/cm. A single-domain state is present within each grain [123].

Curriculum vitae

Personal Information

Name: Marina

Surname: Zakhozheva

Email: Zakhozheva@gmail.com

Date of birth: 02/11/1986

Nationality: Russian

Work Experience

2015 – present	Product Marketing Engineer DENSsolutions
2011 – 2012	Engineer Rzhanov Institute of Semiconductor Physics

Education

2012 – 2015	Ph.D. Technische Universität Darmstadt, Geomaterial Science
2009 – 2011	Master of Physics Tomsk State University, Department of Physics
2004 – 2009	Bachelor of Physics Tomsk State University, Department of Physics

Internship and Seminars

March – May 2014	Visiting Scientist USA, Iowa State University, The Ames Laboratory
May 2013	Quantitative Electron Microscopy (QEM) school Saint-Aygulf, France

Main Publications

- J. Glaum, M. Zakhozheva, M. Acosta, E. Aksel, H.-J. Kleebe, M. Hoffman, LA Schmitt, Influence of B-Site Disorder on the Properties of Unpoled $Bi_{1/2}Na_{1/2}TiO_3$-0.06$Ba(Zr_xTi_{1-x})O_3$ Piezoceramics. Journal of the American Ceramic Society (2016).
- M. Zakhozheva, L. A. Schmitt, M. Acosta, H.Guo, W. Jo, H.-J. Kleebe, X. Tan, Wide compositional range in situ electric field investigations on lead-free Ba(Zr0.2Ti0.8)O3-x(Ba0.7Ca0.3)TiO3 piezoceramic, Physical Review Applied, submitted.

- M. Zakhozheva, L. A. Schmitt, M. Acosta, W. Jo, J. Rödel, and H.-J. Kleebe, In situ electric field induced domain evolution in Ba(Zr0.2Ti0.8)O3-0.3(Ba0.7Ca0.3)TiO3 ferroelectrics, Applied Physics Letters 105, 112904 (2014).
- Litovchenko I. Yu., Tyumentsev A.N., Zakhozheva M.I., Korznikov A.V. Direct and reverse martensitic transformation and formation of nanostructured states during severe plastic deformation of metastable austenitic stainless steel, Adv. Mater. Sci. №31, 47 (2012).
- Zakhozheva M.I., Litovchenko I.Yu., Tyumencev A.N. Investigation of defect structure and phase composition of metastable austenitic steel during severe plastic deformation by rolling University news. Physics. –V. 53, №11/3. P. 95 – 98 (2010).

Main Conferences

- Workshop on Advanced In Situ TEM/STEM, Gothenburg, Sweden, 2015 (Talk).
- International Microscopy Conference, Prague, Czech Republic, 2014 (Poster).
- International Symposium SFB 595, Rügen Island, Germany, 2014 (Talk).
- XXV Russian conference on electron microscopy, Chernogolovka, Russia, 2014 (Talk).
- XI International scientific and technological Ural symposium of young metallography scientists, Yekaterinburg, Russia, 2010 (Talk).
- Physics and chemistry of nanomaterials, Tomsk, Russia, 2009 (Talk).
- V Russian conference of the young scientists “Physics and chemistry of the high-energy systems”, Tomsk, Russia, 2009 (Talk).
- 15th Russian conference of student physicists, Kemerovo, Russia, 2009 (Talk).
- XI Russian scientific student conference “Solid state physics”, Tomsk, Russia, 2008 (Talk).